

**USING INTERNET-ENABLED REMOTE
INSTRUMENTATION FOR RESEARCH AND
TRAINING IN PHYSICS: EVALUATION OF
DIFFERENT DIFFUSION BARRIERS FOR SILVER
METALLIZATION**

by



A minithesis submitted in partial fulfilment
of the requirements for the degree of

MAGISTER SCIENTIAE

in the

**DEPARTMENT OF PHYSICS,
UNIVERSITY OF THE WESTERN CAPE**

September 2007

Supervisor: Prof. D. Adams, University of the Western Cape

KEYWORDS

INTERNET

COLLABORATORY

VIRTUAL LABORATORY

REMOTE INSTRUMENTATION

THERMAL STABILITY

DIFFUSION BARRIERS

RUTHERFORD BACKSCATTERING

SCANNING ELECTRON MICROSCOPE

FOUR POINT PROBE FURNACE

X-RAY DIFFRACTION



ABSTRACT

Using Internet-enabled Remote Instrumentation for Research and Training in Physics: Evaluation of Different Diffusion Barriers for Silver Metallization

Name: S. Majiet

M.Sc. Minitesis,

Department of Physics,

University of the Western Cape

The growth of the Internet has led to many interesting developments for both educational and commercial purposes. In this project an attempt was made to use the Internet for a research purpose to facilitate the determination of the thermal stability of diffusion barriers. Another purpose of this thesis is to investigate the teaching and training use of the Internet through the development of online interactive tools and activities as well as materials. The training aspects are mentioned as it is hoped that this thesis can serve as a form of documentation of the use of the Internet, while the central part was the determination of thermal stability of TiN, TaN and TiW diffusion barriers on Ag.

The fact that most advanced instruments are computer driven or can be interfaced with a computer was exploited to set up a virtual laboratory facility through which sophisticated and scarce instrumentation can be remotely accessed. The major piece of equipment that forms part of the laboratory is a four-point probe furnace at Arizona State University, Tempe, USA. The Internet made it possible to use the facility to

perform an online experiment to determine the effectiveness of different diffusion barriers for silver metallisation. This was accomplished by measuring the resistance of the different samples remotely over the Internet through the control of the four-point probe furnace at Arizona State University. Four types of analysis were used to determine the thermal stability of the diffusion barriers, namely the Scanning Electron Microscopy, Rutherford Backscattering Spectrometry, X-Ray Diffraction and resistivity measurements. Similar facilities exist at Oak Ridge National Laboratory, Tennessee, USA, where a range of different electron microscopes can be accessed remotely via the Internet.

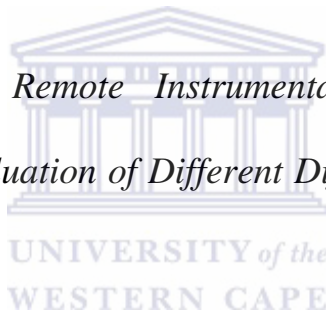
The measurements of the diffusion barriers form the main part of this work. However, the other aspects required for the use of the Internet in such a system, such as the development of a website to receive and upload scanning electron microscopy (SEM) images, the development of the virtual scanning electron microscope and the learning of the Virtual Reality Markup Language are also included.

September 2007

DECLARATION

I declare that

*Using Internet-enabled Remote Instrumentation for Research and
Training in Physics: Evaluation of Different Diffusion Barriers for Silver
Metallization*



is my own work, that it has not been submitted for any degree or examination in any other university, and that all the sources I have used or quoted have been indicated and acknowledged by complete references.

Full Name: Siradz Majiet

Date: September 2007

Signed:.....

ACKNOWLEDGEMENTS

I would like to thank God Almighty who made everything possible.

I am grateful to the following people:

Prof. D. Adams of the Physics Department at the University of the Western Cape, who supervised this investigation, for his guidance, advice, friendship and for the many stimulating discussions.

Dr. B. Julies of the Physics Department at the University of the Western Cape, who acted as co-supervisor, for his assistance, encouragement and support.

Prof. Jim Mayer of Arizona State University, for his interest and support.

Dr. Gerald Malgas of the Council of Scientific and Industrial Research (CSIR) for his proof reading of the thesis, his friendship, interest and support.

The staff of the Physics Department at the University of the Western Cape for their encouragement.

My friends Zelda Vergotine and Faghrie Mitchell for their moral support and for just being there.

Mrs. Vergotine and the late Mr. Vergotine for their constant encouragement and support.

My fellow students: Messrs Gerald Malgas, Chris Arendse, Theo Muller, Sylvain Halindintwali and Nolan Botha for their much-valued friendship and many discussions around this investigation.

My colleagues at CSIR, in particular Lindsay Linzer for her interest and support, others which need special mention are Steve Spottiswoode, Dave Roberts, Navin Singh and Dushendra Naidoo for their support.

My parents, brothers (Tariq and Junaid), family, grandmother and friends for their moral support.



TO MY PARENTS

RUSHDIEN & SHIREEN

CONTENTS

KEYWORDS	I
ABSTRACT	II
DECLARATION	IV
ACKNOWLEDGEMENTS	V
LIST OF FIGURES	X
LIST OF TABLES	XIII
LIST OF ABBREVIATIONS	XIV
PREFACE	1
CHAPTER ONE:INTERNET-ENABLED REMOTE RESEARCH: A NEW APPROACH TO RESEARCH AND TRAINING IN PHYSICS	2
1.1 OVERVIEW OF COLLABORATORIES	2
1.2 THE VIRTUAL LABORATORY AT UWC	6
1.2.1 <i>Scanning Electron Microscope (SEM)</i>	8
1.2.2 <i>Image-capturing software</i>	8
1.2.3 <i>Image manipulation facility</i>	8
1.3 THE FOUR-POINT PROBE FURNACE AT ARIZONA STATE UNIVERSITY (ASU)...	9
1.3.1 <i>The control interface</i>	10
1.3.2 <i>The Van der Pauw method</i>	12
1.4 THE FACILITY AT OAK RIDGE NATIONAL LABORATORY	16
1.5 DETERMINING THE FEASIBILITY OF USING INTERNET-BASED SCIENTIFIC INSTRUMENTS IN PHYSICS RESEARCH	18
1.5.1 <i>Considerations</i>	18
1.5.2 <i>Benefits</i>	18
1.6 FUTURE DEVELOPMENTS IN THE FIELD OF IRI.....	19
1.7 CONCLUSION	22
1.8 REFERENCES – CHAPTER 1.....	22
CHAPTER TWO: USING INTERNET-ENABLED REMOTE INSTRUMENTATION TO STUDY THE THERMAL STABILITY OF DIFFUSION BARRIERS FOR SILVER METALLISATION	26
2.1 INTRODUCTION	26

2.2	DIFFERENT TYPES OF DIFFUSION BARRIER.....	28
2.2.1	<i>Sacrificial barriers</i>	28
2.2.2	<i>Stuffed barriers</i>	28
2.2.3	<i>Amorphous barriers</i>	29
2.3	DIFFUSION BARRIERS FOR AG METALLISATION	32
2.3.1	<i>Introduction</i>	32
2.3.2	<i>Using TaN, TiN and TiW as diffusion barriers for Ag</i>	32
2.4	RESULTS	37
2.4.1	<i>ASU vacuum furnace</i>	37
2.4.2	<i>iThemba Laboratories</i>	47
2.5	DISCUSSION	53
2.5.1	<i>ASU vacuum furnace</i>	53
2.5.2	<i>iThemba Laboratories</i>	55
2.6	CONCLUSION	56
2.7	REFERENCES – CHAPTER 2.....	57
CHAPTER THREE:SUMMARY AND FUTURE WORK.....		60
3.1	SUMMARY.....	60
3.2	FUTURE WORK	61
APPENDIX A: THE DEVELOPMENT OF A VIRTUAL SCANNING ELECTRON MICROSCOPE (VSEM) FOR TEACHING AND TRAINING.....		62
A.1	THE SCANNING ELECTRON MICROSCOPE: AN OVERVIEW	62
A.1.1	<i>The detector</i>	64
A.1.2	<i>Electron gun</i>	65
A.1.3	<i>Electromagnetic lenses</i>	68
A.1.4	<i>Apertures</i>	70
A.2	THE VIRTUAL SCANNING ELECTRON MICROSCOPE	71
A.2.1	<i>Rationale</i>	71
A.2.2	<i>The design of the VSEM</i>	71
A.3	HOW TO USE THE VIRTUAL SCANNING ELECTRON MICROSCOPE	73
A.4	CONCLUSION	82
A.5	REFERENCES – APPENDIX A.....	82
APPENDIX B: EXPERIMENTAL TECHNIQUES.....		85
B.1	RUTHERFORD BACKSCATTERING SPECTROMETRY (RBS).....	85
B.1.1	<i>Kinematic factor</i>	86
B.1.2	<i>Differential cross-section</i>	88

<i>B.1.3</i>	<i>Energy loss</i>	89
B.2	X-RAY DIFFRACTION (XRD)	91
<i>B.2.1</i>	<i>How X-rays are formed</i>	<i>91</i>
<i>B.2.2</i>	<i>Bragg diffraction</i>	<i>92</i>
<i>B.2.3</i>	<i>Intensity of diffraction</i>	<i>95</i>
<i>B.2.4</i>	<i>Atomic and structure factors</i>	<i>99</i>
B.3	VIRTUAL REALITY MODELLING LANGUAGE (VRML)	100
<i>B.3.1</i>	<i>Introduction</i>	<i>100</i>
<i>B.2.2</i>	<i>Working with VRML 2.0</i>	<i>102</i>
<i>B.2.3</i>	<i>Animation</i>	<i>107</i>
B.4	REFERENCES – APPENDIX B	112
APPENDIX C: INTERNET USES		118
C.1	SUMMARY.....	118
C.2	REFERENCES – APPENDIX C	121
APPENDIX D: GRAPHS		126
D.1	NOTES.....	126



LIST OF FIGURES

Figure 1.1:	Flowchart depicting the different components of VIMS at the University of the Western Cape.....	7
Figure 1.2:	The equipment that constitutes the Visualization Facility at UWC.....	8
Figure 1.3:	The four-point probe furnace at Arizona State University [1.10].....	11
Figure 1.4:	The control interface of the four-point probe furnace at ASU viewed through a Java-enabled web browser [1.10]	11
Figure 1.5:	An arbitrary shaped sample with four contacts along its circumference, the current source feeding and the voltage reading [1.10].....	14
Figure 1.6:	The Java interface of the electron microscopes at ORNL which allows a scientist to control the electron microscopes remotely [1.8].....	17
Figure 2.1:	Illustration of the position of a diffusion barrier in a typical IC [2.3]	27
Figure 2.2:	The different stages of a diffusion barrier X and how it reacts with the contact materials A and B [2.2]	30
Figure 2.3:	“Stuffed” barrier.....	30
Figure 2.4:	Amorphous barrier	31
Figure 2.5:	Schematic diagram of the high-vacuum system evaporator used for the deposition of the Ag layers onto the different barrier materials (TiN, TiW and TaN) [2.12]	34
Figure 2.6:	Plot of sheet resistance vs. annealing temperature of an Ag (200 nm)/TiW (200 nm) sample	38
Figure 2.7:	Plot of sheet resistance vs. annealing temperature of an Ag (200 nm)/TaN (200 nm) sample	39
Figure 2.8:	The RBS spectrum of an as-deposited Ag (200 nm)/TiN (200 nm) sample compared with sample annealed in vacuum until 750 °C.....	41
Figure 2.9:	The RBS spectrum of an as-deposited Ag (200 nm)/TiW (200 nm) sample compared with sample annealed in vacuum until 750 °C.....	42
Figure 2.10:	The RBS spectrum of an as-deposited Ag (200 nm)/TaN (200 nm) sample compared with a sample annealed in vacuum until 750 °C.....	43
Figure 2.11:	SEM micrograph of (a) an as-deposited Ag (200 nm)/TiN (200 nm) sample, and (b) a sample annealed in vacuum until 750 °C	44
Figure 2.12:	SEM micrograph of (a) an as-deposited Ag (200 nm)/TiW (200 nm) sample, and (b) a sample annealed in vacuum until 750 °C	45

Figure 2.13:	SEM micrograph of (a) an as-deposited Ag (200 nm)/TaN (200 nm) sample, and (b) a sample annealed in vacuum until 750 °C	46
Figure 2.14:	XRD spectra of the Si substrate, and the as-deposited and annealed Ag (200 nm)/TiN (200 nm) sample	48
Figure 2.15:	XRD spectra of the Si substrate, and the as-deposited and annealed Ag (200 nm)/TiW (200 nm) sample	49
Figure 2.16:	XRD spectra of the Si substrate, the as-deposited and annealed Ag (200 nm)/TaN (200 nm) sample	50
Figure A.1:	Schematic representation of a scanning electron microscope column (courtesy of Hitachi Ltd) [A.4]	63
Figure A.2:	Ray diagram of a two-lens SEM showing the electron beam path to the specimen [A.5]	64
Figure A.3:	The electron gun [A.9]	66
Figure A.4:	The electromagnetic lens [A.11]	69
Figure A.5:	The electron gun	75
Figure A.6:	The condenser lens	76
Figure A.7:	The objective lens	77
Figure A.8:	The detector	78
Figure A.9:	The microscope created with CosmoWorlds	79
Figure A.10:	The major components created with CosmoWorlds	80
Figure A.11:	The detector of the microscope created with CosmoWorlds	81
Figure B.1:	Diagram of the experimental set-up of Rutherford backscattering. A 2 MeV $^4\text{He}^{2+}$ beam was used [B.2]	86
Figure B.2:	Diagram showing elastic collision between a projectile of mass M_1 with velocity V_0 and a stationary target of mass M_2 [B.2]	87
Figure B.3:	Schematic drawing to illustrate the production of K and L characteristic peaks that appear in XRD spectra [B.5]	93
Figure B.4:	The condition for the first and zeroth order diffraction from a row of atoms [B.7]	97
Figure B.5:	(a) A unit cell showing the lattice parameters a, b and c. (b) The three-dimensional lattice [B.14]	98
Figure B.6:	The condition for Bragg's Law [B.11]	98
Figure B.7:	A print screen showing the result of example 1	105

Figure B.8:	The RGB colour cube where the greys are on the dotted diagonal [B.31]	106
Figure B.9:	An EventIn (Starttime) and Eventout (Fraction_changed) of the timesensor node [B.46]	112
Figure D.1:	Plot of sheet resistance vs. annealing temperature of an Ag (200 nm)/TiW (200 nm) sample	126
Figure D.2:	Plot of sheet resistance vs. annealing temperature of an Ag (200 nm)/TaN (200 nm) sample	127



LIST OF TABLES

Table 1.1:	Collaboratories, their website addresses and the research they undertake.....	5
Table 1.2:	The switches to close and over which contact points the voltage will be read.....	13
Table 2.1:	Summary of the techniques used in thin films and the information provided	36
Table 2.2:	List of the resistivity measurements for the as-deposited and annealed TiN sample in vacuum at 650 °C for 30 minutes.....	51
Table 2.3:	List of the resistivity measurements for the as-deposited and annealed TaN sample in vacuum at 650 °C for 30 minutes	52
Table 2.4:	List of the resistivity measurements for the as-deposited and annealed TiW sample in vacuum at 650 °C for 30 minutes.....	52
Table 2.5:	A list of the resistivity measurements for the as-deposited and annealed TiN, TaN and TiW samples in vacuum at 650 °C for 30 minutes	52
Table C.1:	A list of developments and its use briefly described.	118

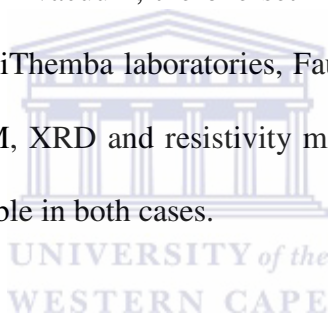
LIST OF ABBREVIATIONS

ARPA	Advanced Research Projects Agency
ARPANET	Advanced Research Projects Agency Network
ASU	Arizona State University
CTE	Coefficient of Thermal Expansion
EDS	Energy Dispersive Spectroscopy
EDS	Energy Dispersive Spectroscopy
ftp	File Transfer Protocol
HTML	Hypertext Markup Language
HTML	High Temperature Materials Lab (of the Oak Ridge National Laboratory)
IC	Integrated Circuit
IEC	International Electrotechnical Commission
IMS	Information Management System
IRI	Internet Remote Instrumentation
ISO	International Standards Organization
JTC	Joint Technical Committee
MCA	Multichannel Analyser
ORNL	Oak Ridge National Laboratory
RBS	Rutherford Backscattering Spectrometry
SEM	Scanning Electron Microscope
SIS	Soft Imaging Software
TCP/IP	Transmission Control Protocol / Internet Protocol
TEM	Transmission Electron Microscope
URL	Universal Resource Locator
US DoD	United States Department of Defence
UWC	University of the Western Cape
VIMS	Virtual Information Management System
VR	Virtual Reality
VRML	Virtual Reality Modelling Language
VSEM	Virtual Scanning Electron Microscope
XRD	X-Ray Diffraction

PREFACE

In the thesis, the history of the Internet, a brief background and examples of collaboratories are discussed. The development of the Virtual Information Management System (VIMS) is mentioned with the goal to serve as a portal for researchers, scientists and learners to request or obtain images and remotely control research equipment from around the world.

The main thrust of the thesis is Chapter 2, which in fact uses remote instruments and investigates the thermal stability of TaN, TiN and TiW diffusion barriers on Ag. Two sets of samples are annealed in vacuum, the one set in a four point probe furnace at ASU, another in a furnace at iThemba laboratories, Faure. It is then shown using the four techniques of RBS, SEM, XRD and resistivity measurements that the diffusion barriers did indeed remain stable in both cases.



A further development to VIMS, is included namely the Virtual Scanning Electron Microscope (VSEM), it is included in Appendix A, and serves as a beta version of the microscope that could be tested and developed in the future.

CHAPTER ONE: INTERNET-ENABLED REMOTE RESEARCH: A NEW APPROACH TO RESEARCH AND TRAINING IN PHYSICS

1.1 Overview of laboratories

During the 1960s, at the height of the cold war, the United States Department of Defence (US DoD) wanted a command and control network that could withstand a nuclear war. Traditional circuit switching networks were too vulnerable, as the loss of only one line or switch would render the network useless. The DoD therefore approached its research arm, the Advanced Research Projects Agency (ARPA), to solve the problem. The ARPA, after consulting various experts, decided that a packet-switching network was needed [1.1]. This network connected together various institutions and contractors, and became known as the Advanced Research Projects Agency Network (ARPANET) [1.2]. After this network was established, ARPA realized that the transmission protocol in use was not stable, and this culminated in the invention of the Transmission Control Protocol / Internet Protocol (TCP/IP) model. TCP/IP was becoming increasingly important, as more and more networks were being connected to ARPANET [1.3]. TCP/IP became the basis of what we now call the Internet, as it allowed different networks from around the world to communicate with one another. TCP/IP became the official protocol of the Internet on 1 January 1983 [1.4].

The impact that the Internet has had on the accumulation and distribution of information is remarkable. Developments using the Internet include online newspapers, magazines, chatting, e-commerce and teleconferencing. The world has

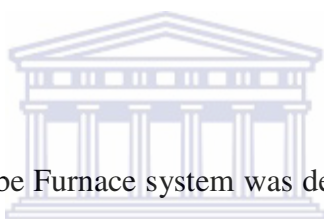
certainly become a smaller place, where communication can be set up between interested parties at the click of a button, with physical distances no longer being a factor. This ease of communication through text, voice and video or even Virtual Reality (VR) [1.5] has facilitated the realisation of a “global village”.

The development of the Internet has modernised traditional teaching and training. The Internet has opened the possibility for students to enrol online and access equipment and instruments remotely. With today’s scientific equipment being largely computer driven, remote instrumentation has become a reality, making scientific equipment available over the Internet. Remote access via the Internet makes it possible to share expensive and advanced equipment, as duplication in laboratories worldwide is currently not economically viable. The Internet has therefore been utilised in a number of formats in the research environment, in remote instrumentation, virtual laboratories and collaboratories (See Appendix C for a detailed list of Internet uses in research with their article references).

The establishment of virtual laboratories has enabled researchers and students to gain access to instrumentation and equipment at any laboratory in the world from their offices. The virtual laboratory is a “real space” with virtual instrumentation accessible to users from remote regions. A collaboratory, however, was defined by William Wulf in 1989 as a “center without walls, in which the nation’s researchers can perform research without regard to physical location, interaction with colleagues, accessing instrumentation, sharing data and computational resources, and accessing information in digital libraries” [1.6]. A distinctive characteristic of collaboratories is that they focus on data collection and analysis [1.7]. Numerous institutions from around the

world such as Arizona State University (ASU), University of Michigan and the Oak Ridge National Laboratory (ORNL) have recognised the potential and the advantage of remote instrumentation [1.8-1.10]. Many institutions do not have the resources to acquire expensive equipment, and remote instrumentation is an excellent way of bridging this gap. The remote instrumentation facilities are elaborated on below.

At the ORNL [1.11] the Transmission Electron Microscope (TEM) and Scanning Electron Microscope (SEM), like many other scarce scientific instruments, can be accessed remotely. At the booked time samples are placed in the microscope and the required experiment is run. This is done remotely through a Java-compliant web browser [1.12, 1.13, 1.14].



An interactive Four Point Probe Furnace system was developed at ASU [1.15], which can be remotely accessed through a Java-enabled browser. This furnace is used mainly in material-related science to obtain in-situ resistance measurements of thin solid films. The work described in this thesis uses this system.

WESTERN CAPE

An interactive scanning electron microscope (SEM) at the University of Michigan [1.16] is used for surface morphology and elemental analysis. This microscope is also accessed through a Java-enabled browser.

A number of institutions have also established collaboratories in order to facilitate research, communication between researchers, data analysis and storage. Table 1.1 summarises a few collaboratories and the type of research they focus on.

Table 1.1: Collaboratories, their website addresses and the research they undertake

Name of Collaboratory	Type of Research
Biological Sciences Collaboratory [1.17] (http://www.pnl.gov/biology)	Sharing of biological data and analysis
Diesel Combustion Collaboratory [1.18] (http://cgi.ncsa.uiuc.edu/cgi-bin/General/CC/irg/clearing/projectAbstract.pl?projid=1239)	Problem-solving environment for combustion researchers
Biological Collaborative Research Environment (http://www.ks.uiuc.edu/Research/biocore/)	Collaboration tool for biologists
Molecular Interactive Collaborative Environment (http://www.sdsc.edu)	Collaborative access and manipulation on 3D molecular models
Human Environment Regional Observatory [1.19] (http://hero.geog.psu.edu/projectDescription.htm)	Studies of human aspects of global environmental change
National Fusion Collaboratory [1.20, 1.21] (http://www.fusiongrid.org/projects/)	Uses computational grids to conduct physics research
Medical Ignorance Collaboratory (http://www.ignorance.medicine.arizona.edu/collaboratory.html)	Collaborative tools to improve the understanding of medical matters

Most sophisticated and advanced instrumentation is computer driven and hence can be connected to the Internet. The advantage of this is that very expensive equipment, formerly only available at elite institutions, can now be shared and accessed via the Internet by other users as well. In South Africa, with the introduction of Outcomes Based Education in schools, education has been moved towards being more activity based [1.22]. The Internet can therefore also be exploited to bring experiments via advanced instrumentation into ordinary classrooms. A biology class, for example, could study the compound eye of a fly by logging onto the Internet and accessing a remote electron microscope at a neighbouring university.

1.2 The Virtual Laboratory at UWC

The Department of Physics at the University of the Western Cape (UWC) has developed a facility called “The Virtual Laboratory”. A virtual laboratory is defined as a space (a dedicated computer laboratory or even a personal office) from where instruments at a remote site can be accessed; the experiments are done remotely, with the parameters being changed via the Internet and the result seen immediately. This makes the experiment interactive.

VIMS (Virtual Information Management Systems) consist of two major components, namely the “Virtual Laboratory” and the “Information Management System” (Figure 1.1). The first component, the Virtual Laboratory, is a real space from where advanced instruments can be accessed. These instruments are used for teaching as well as research, with researchers doing experiments on these instruments without having to travel to the institutions. The second component, the Information Management System (IMS), was developed to capture, process and distribute image

data. Currently the IMS is used for the collection and distribution of optical and electron microscopy images that are obtained at UWC. The users can download archived images of specimens or make specific requests.

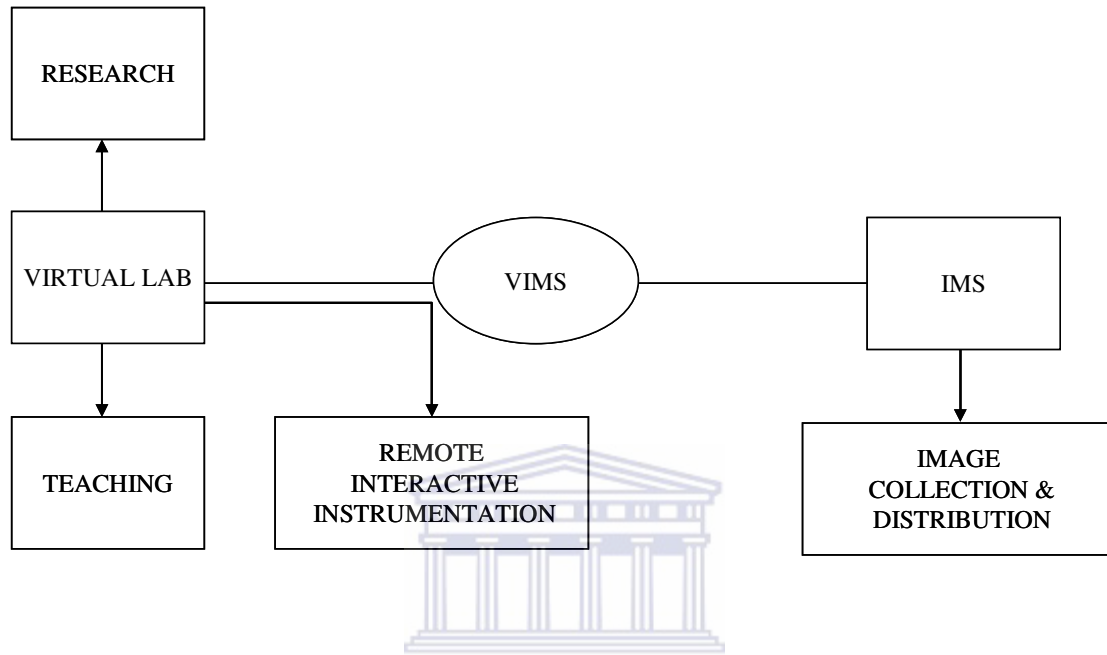


Figure 1.1: Flowchart depicting the different components of VIMS at the University of the Western Cape

The facility that enables the realisation of the different goals of the components of VIMS is called the “Visualisation Facility” and consists of three parts, namely:

- The scanning electron microscope (SEM)
- The computer with image-capturing software
- The image manipulation facility (Figure 1.2).

Each of these components are described in the following sections.

1.2.1 Scanning Electron Microscope (SEM)

The Electron Microscopy Unit at UWC has a Hitachi X650 [1.23] scanning electron microscope with Energy Dispersive Spectroscopy (EDS) [1.24] capability. The SEM can achieve magnifications of up to 30 000 times and is used mainly for evaluating the surface morphology of various surfaces or items in great detail. The SEM is used to capture images using different magnifications, which are then distributed online.

1.2.2 Image-capturing software

The video output of the SEM is linked to a computer with image analysis software, which captures real-time images from the microscope using analySIS 3.1. Soft Imaging Software (SIS) GmbH [1.25] are the developers of the image-capturing software that is used by the SEM.

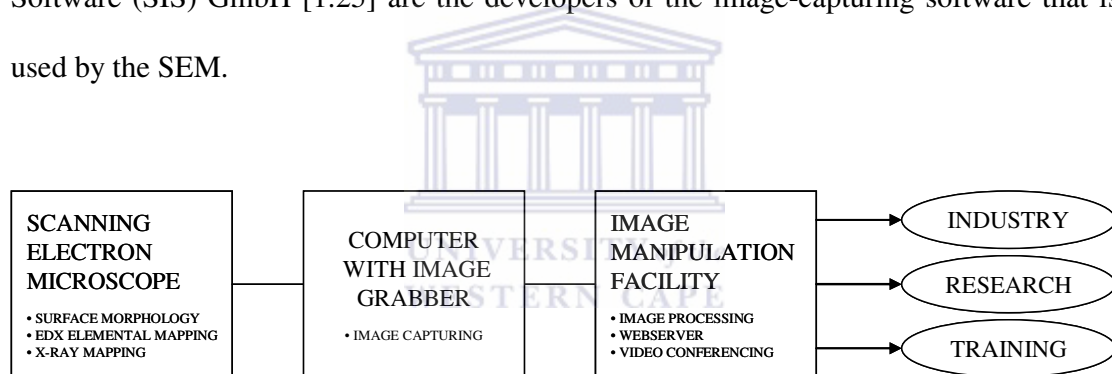


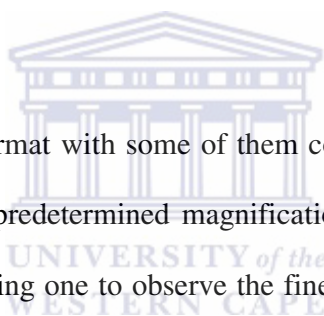
Figure 1.2: The equipment that constitutes the Visualization Facility at UWC

1.2.3 Image manipulation facility

The image manipulation facility is an O2 R5000 Silicon Graphics (SGI) [1.26] workstation. It is used as a web server and an image bank, as well as for image processing. It was previously accessed through the universal resource locator (URL): <http://sem.uwc.ac.za/>. At the present moment, the server is no longer functioning due to skills shortage although the website is available on the accompanying CD. The SGI

workstation retrieves the images from the computer connected to the SEM via the campus network.

Images are continuously made available on the Internet, some of them on request from schools, colleges or private companies. These images are categorised into physical (e.g. potassium dichromate, copper sulphate), biological (e.g. spermatozoa, erythrocytes), everyday objects (e.g. cotton fibres, ant's eye) and a special section called Out of Africa. The Out of Africa section consists of optical images of lions, ostriches and crocodiles and electron microscopy images of certain parts of these animals (e.g. lion hair, a crocodile's tooth, an ostrich feather). No graphical user interface is provided that allows sorting of images. The only way of searching through the images is by using the find command in the respective web browser.



All the images are in JPEG format with some of them converted from the TIFF format. All images can be viewed at predetermined magnifications (more commonly up to ten thousand times), thereby allowing one to observe the finer details of a particular sample. These images are ideal for educational purposes as they can be used either as visual aids or to stimulate discussion in the classroom.

1.3 The Four-Point Probe Furnace at Arizona State University (ASU)

ASU has set up a remote facility with a four-point probe furnace (Figure 1.3). The instrument is controlled through a Java [1.27] program and the control interface is viewed through a Java-enabled browser (Figure 1.4). The furnace is used mainly in material science research to evaluate the resistance of thin solid films using the Van der Pauw method [1.28]. It may be booked online, and then the sample is sent through the post and loaded into the furnace for the experiment. The data can be viewed through the graphical

user interface, but in order to perform any data analysis it has to be remotely retrieved using the file transfer protocol (ftp) [1.29].

1.3.1 The control interface

Once the sample is placed in the furnace, the researcher uses the control interface to control the current, change the starting and final temperature, enter the ramp rate, pre-anneal time, post-anneal time, provide the sample identification and change the way the data are viewed. The control interface gives the user feedback, for example, on the current stage of the furnace, the total time that the sample is annealed, the pressure in the furnace and the resistance of the sample. It also gives the user the ambient temperature in the furnace and the sample temperature. Once the sample is loaded in the furnace the operational mode indicated in the graphical user interface goes from setup to ramp mode. The furnace measures the sheet resistance as a function of temperature. These data can then be used to obtain the reaction sequence such as phase changes and the activation energy of a process (such as diffusion processes or silicide formation).



Figure 1.3: The four-point probe furnace at Arizona State University [1.15]

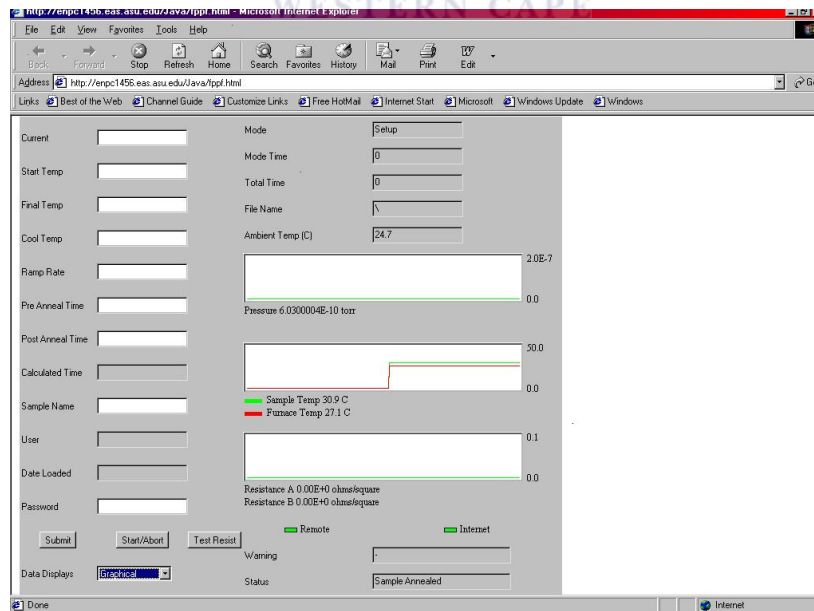


Figure 1.4: The control interface of the four-point probe furnace at ASU viewed through a Java-enabled web browser [1.15]

1.3.2 The Van der Pauw method

The Van der Pauw method is used to determine the resistance of thin films. The experimental setup consists of four probes in contact with the sample at arbitrary points along the circumference, a constant current source, and a voltmeter (Figure 1.5). The optimal conditions required when applying this technique are the following: the contacts need to be positioned at the circumference of the sample and be sufficiently small; and the sample should be homogeneous in thickness and not have any isolated holes or scratches.

The resistance of a thin conductive layer, such as a diffused layer or a thin metal film, is proportional to the resistivity ρ of the layer and inversely proportional to the thickness t . It is convenient to define a quantity R_s which is equal to ρ/t .

The quantity R_s is called the sheet resistance and may be thought of as a material property for conductors which are essentially two-dimensional, because the thickness is negligible compared to the other dimensions. A conducting thin layer consisting of a simple rectangle of length L (in the direction of the current) and width W has a resistance R .

$$R = \frac{\rho}{t} \frac{L}{W} = R_s \frac{L}{W}$$

The ratio L/W is referred to as the number of squares (\square), since it is the number of squares of size W that can fit into the rectangle without overlapping. The term "squares" is dimensionless. The sheet resistance has the unit of ohms, but it is convenient to refer to it as ohms per square (Ω/\square). The resistance of a rectangular thin layer is therefore the sheet resistance times the number of squares (L/W) [1.30].

In the Van der Pauw method four contact points are made to the thin layer; current is carried through the outer two contacts and the voltage drop is measured across the remaining contacts (see Figure 1.5). The figure shows an arbitrary sample with four labelled contacts and a current source and a voltmeter attached to it through a series of labelled switches. Table 2.1 below describes the points across which the voltage will be read when the listed switches are closed and the current source is switched on. The switches are labelled and listed in the table in a clockwise direction (see Figure 1.5).

Table 1.2: The switches to close and over which contact points the voltage will be read

The switches to close	The voltage will be read across these contact points on the sample
1	1-2
2	4-1
3	3-4
4	2-3

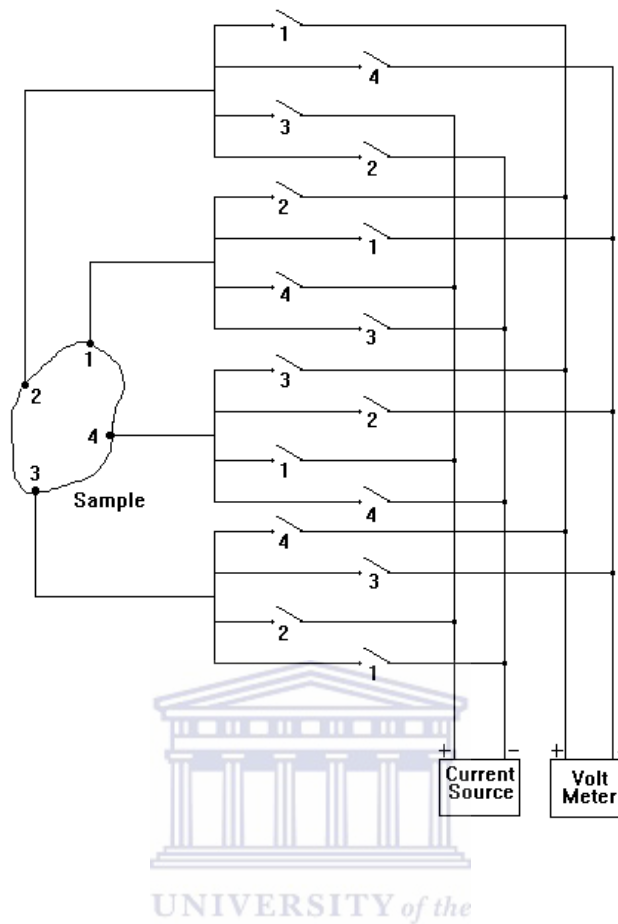


Figure 1.5: An arbitrary Vshaped sample with four contacts along its circumference, the current source feeding and the voltage reading [1.15]

The sheet resistance is given by:

$$R_s = K_p \frac{V}{I}$$

where K_p is a constant that depends on the configuration, position and orientation of the probes. The probes are commonly equally spaced in a straight line, with the two outer

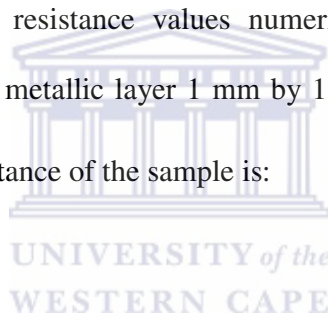
probes being the current probes. The probe spacing L_p is usually small compared to the dimensions of the film and large compared to the layer thickness, t .

If the film is infinite in all planar directions, the constant K_p is:

$$K_p = \frac{\pi}{\ln 2} = 4.5324$$

Correction factors are needed when the dimension of the layer becomes comparable to the probe spacing.

Square samples always have resistance values numerically equal to their R_s value irrespective of their sizes. If a metallic layer 1 mm by 1 mm in area has a measured R_s value of $10 \Omega/\square$, then the resistance of the sample is:



$$R = \frac{\rho L}{tW} = \frac{\rho \text{ 1mm}}{t \text{ 1mm}} = \frac{\rho}{t} = R_s = 10\Omega$$

where ρ is the resistivity of the layer, t the thickness of the layer, L the length and W the width of the sample [1.31].

During the measurement of electrical resistance of a sample, there is the unavoidable attachment of wires. This results in the measurement of the resistance at the point of contact to the sample (contact resistance). The contact resistance is typically negligible, and only becomes a problem when measuring very small resistivities (e.g. superconductivity). The problem of contact resistance is prevented from being a factor in the four-point probe by sending a constant current across the two probes and noting the

voltage across the two remaining probes (see Figure 1.5). If the sample has any resistance to the flow of electrical current there will be a drop in the voltage reading. This instrument was used during my research to obtain resistivity measurements and these measurements are discussed in Chapter 2.

1.4 The Facility at Oak Ridge National Laboratory

The Oak Ridge National Laboratory (ORNL) has several electron microscopes at the High Temperature Materials Lab (HTML) in Oak Ridge, Tennessee. These instruments are expensive to purchase and maintain. Few companies or laboratories are able to own similar equipment. The idea behind the facility is to create a general, portable, remote control interface to microscopes located anywhere on the World Wide Web. This will allow researchers to utilise these facilities on line without having to travel. The interface (Figure 1.6) is written in Java and executes as an applet allowing a scientist to control the microscope remotely via any Java-compliant Web browser.

The transmission electron microscope and scanning electron microscope are scheduled and booked like many other scarce scientific instruments. Scientists submit proposals to use the instrument, which are evaluated and scheduled once they are accepted. The scientist then sends his sample to Oak Ridge National Lab where a technician places it in the microscope, and the experiment is carried out remotely using the Java applet that is sent via the Internet from the computer connected to the microscope.

The remote user has control of sample movement, magnification and focus. For the purposes of speed of processing and to decrease the network load, the microscope supplies a new 256 x 256 x 8 bit grey scale image each time the user changes a parameter on the control panel. At any time during the scheduled experiment, the user can download

a full-resolution version of the microscope image (1 000 x 1 000 x 14 bit grey scale) [1.32].

The microscope was not used during our research and serves as an example of a remote microscope that can be controlled through the Internet. All the microscopes are controlled by Digital Micrograph software [1.33]. An interface layer between this software and the Web server allows the microscopes to be controlled from the Java applet. Both the applet and the Digital Micrograph software have built-in fail-safe checks to prevent the instrument from being damaged.

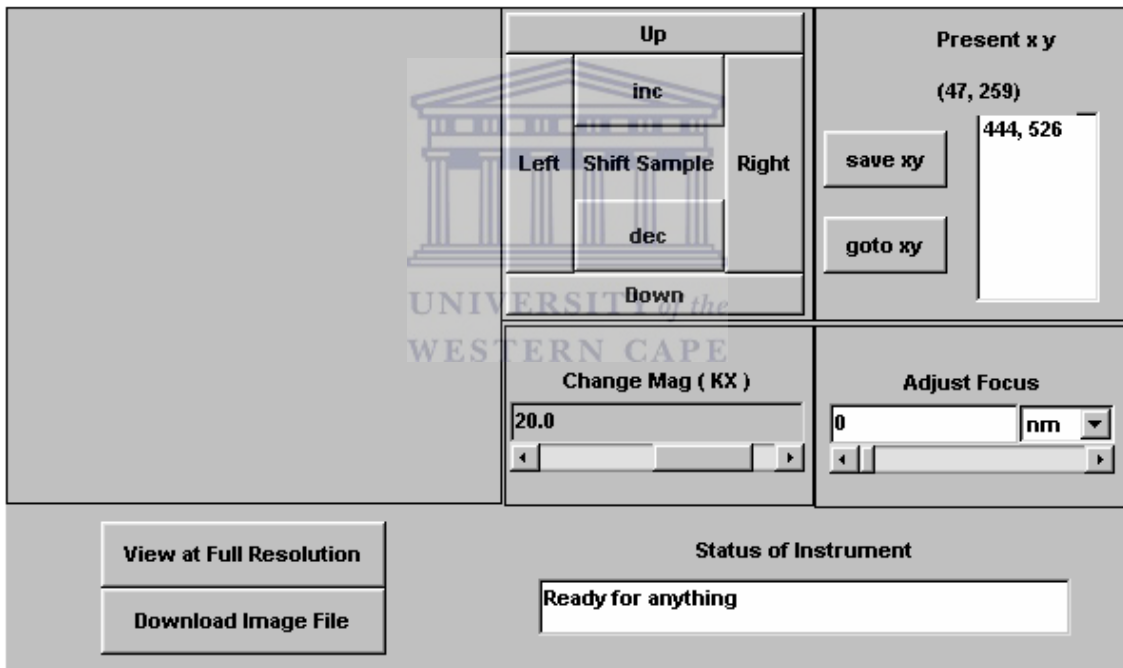


Figure 1.6: The Java interface of the electron microscopes at ORNL which allows a scientist to control the electron microscopes remotely [1.32]

Students and researchers can access remote instruments via the Internet and without having to incur expenses such as travelling. The availability of remote instrumentation makes it possible for researchers not to be restricted in the type of research they want to

do, because if the facility is not available it can be accessed from somewhere else. The virtual laboratory at UWC was initially accessed through the Internet address <http://sem.uwc.ac.za/>, as mentioned, the server is no longer functioning but the website is available on the accompanying CD.

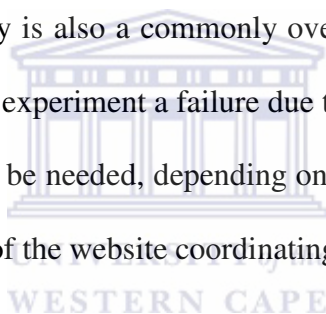
1.5 Determining the feasibility of using Internet-based scientific instruments in physics research

1.5.1 Considerations

Computer. The use of the remote instrument might impose special requirements on the computer being utilised. The website will have to be checked.

Time of day. The time of day is also a commonly overlooked consideration as peak times could render a potential experiment a failure due to bandwidth limitations.

Operator. An operator might be needed, depending on the instrument and utilisation. Special note should be taken of the website coordinating the utilisation times.



1.5.2 Benefits

Financial. There will be less strain on the financial resources of the user, as no additional expenses will be incurred such as travel and accommodation.

Timeousness. The data from certain experiments would be immediately available, thus saving time.

Community. Access to the instrument would be available to a larger research community, therefore making it easier to obtain the skill needed to operate the instrument.

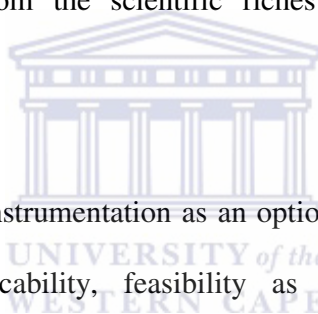
1.5.3 Risks

BANDWIDTH	SIGNIFICANT	The bandwidth available to the user would also be a constraint on the user as in certain instances lots of bandwidth is essential for being productive on the Internet, especially if the website has rich content. Recent developments in Internet infrastructure, especially in the United States, has virtually eliminated these constraints with projects such as GRID [1.34] and Internet2 [1.35], which are essentially advanced networks that are able to transmit data at gigabits per second (Gbps).
POST	SIGNIFICANT	Sending the sample to the institution or university by post can also be seen as a constraint, as there would be a delay before the experiment could be conducted. It could take longer to send the sample than if a person actually went to the location and did the experiment in certain scenarios.
SECURITY	SIGNIFICANT	A disadvantage of remote instrumentation is that because of security concerns, research on equipment would have to be limited. Security concerns most importantly include crackers who want to cause malicious damage. The result is that for the time being travel would still be necessary in certain instances.
LEVEL OF INSTRUCTION	NOT SIGNIFICANT	The near elimination of travel has its advantages and disadvantages. The costs of the university or institution are reduced, but the student or researcher would never in some instances get real hands-on experience.

1.6 Future Developments in the Field of IRI

There has been a major boost in the infrastructure development with the development of GRID. The term is not an abbreviation or an acronym and merely is the data link between the researchers/users and the instruments that they use. GRID, an experimental network in the United States, is used to test the limitations of what can be done remotely over the

Internet. Projects as huge as this are normally borne out of collaboration where a number of institutions co-fund the project because of the huge expense involved and the tremendous benefits that can be reaped. Considering the rising costs of scientific equipment, important scientific equipment is becoming a scarce item. The maintenance of the instrument is also an added expense for prospective institutions and contributes volumes to its rarity. These types of infrastructure development improve the transfer of data over the Internet, which includes, amongst other things, video, text and voice. Training is essential for potential users to be effective. This may be an orientation visit to the location or simply a remote training session between the operator and the student using video and voice. The prospect of remote instrumentation ensures that disadvantaged students will also benefit from the scientific riches of well-equipped laboratories worldwide.

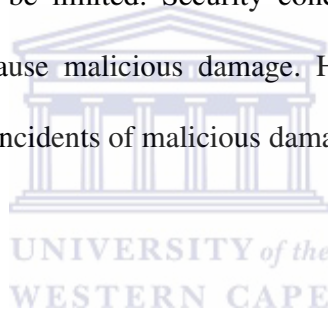


To effectively assess remote instrumentation as an option, it has to be measured against some criteria, namely applicability, feasibility as well as the advantages and disadvantages.

Remote instrumentation is necessary especially in the context of rising costs of the purchasing and maintenance of research equipment. Remote instrumentation gives students or researchers the opportunity to work with research equipment from a distance, irrespective of whether their universities or institutions have the finances to acquire the equipment or not. Research conducted in this way does, however, have its limitations, the details of which are discussed later in this chapter.

The most obvious advantage of remote instrumentation is that it would considerably reduce travelling expenses of universities or institutions. Previously one would have had to travel to the location of the equipment, but with remote instrumentation all that is needed is to arrange with the necessary authorities of the equipment. The data would also be available almost immediately depending on the facilities of the institution that hosts the equipment. The equipment would now be available to a wider research community irrespective of their background, and in this way training could be given to more scientists on scarce equipment.

One disadvantage of remote instrumentation is that because of security concerns, research on equipment would have to be limited. Security concerns most importantly include crackers who would try to cause malicious damage. However, with the advances in Internet security in the future, incidents of malicious damage to remote instruments would become negligible.

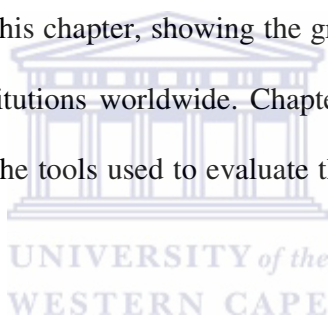


Another disadvantage is that the bandwidth available to the user would also be a constraint, as in certain instances lots of bandwidth is essential to being productive on the Internet, especially if the website has rich content. Recent developments in Internet infrastructure, especially in the United States, has all but eliminated these constraints with projects such as GRID and Internet2, which are essentially advanced networks that are able to transmit data at gigabits per second (Gbps).

Sending the sample to an institution or university may also be a constraint as there would be a delay before the experiment could be conducted.

1.7 Conclusion

This chapter focuses on aspects of using remote instrumentation and its drawbacks. The concept of a virtual laboratory is introduced in remote instrumentation, and the advantage of accessing costly equipment over the Internet is shown. The considerable benefits of using remote instruments over the Internet are discussed. The time-consuming aspect in certain critical projects, however, might hinder the progress of remote instrumentation. Although Internet bandwidth is a huge drawback, the development of Quality of Service [1.36, 1.37] and the move towards gigabit speeds to the desktop will certainly minimise if not completely eliminate this drawback. The online four-point probe furnace is discussed in detail and how it can be used to conduct material science research. The microscopes at the ORNL are summarised in this chapter, showing the growing trend towards the use of remote instrumentation at institutions worldwide. Chapter 2 discusses the remote four-point probe furnace as one of the tools used to evaluate the efficacy of diffusion barriers for Ag metallisation.



1.8 References – Chapter 1

- 1.1 Tannenbaum A.S. (1996). *Computer networks (3rd Edition)*. New Jersey: Prentice Hall.: 47.
- 1.2 Tannenbaum A.S. (1996). *Computer networks (3rd Edition)*. New Jersey: Prentice Hall.: 48.
- 1.3 Tannenbaum A.S. (1996). *Computer networks (3rd Edition)*. New Jersey: Prentice Hall.: 49.
- 1.4 Tannenbaum A.S. (1996). *Computer networks (3rd Edition)*. New Jersey: Prentice Hall.: 52.

- 1.5 Wexelblat A. (1993). *Virtual reality: applications and explorations*. Boston, MA.: Morgan Kaufmann Publishers.
- 1.6 Wulf W. (1989). *The National Collaboratory*. In: *Towards a National Collaboratory*. Unpublished report of a National Science Foundation invitational workshop, Rockefeller University, New York.
- 1.7 Chin, G.Jr. and Lansing, C.S. (2004). *Capturing and supporting contexts for scientific data sharing via the biological sciences collaboratory*. Proceedings of the 2004 ACM Conference on Computer-supported Cooperative Work. ACM Press.: 409.
- 1.8 *Arizona State University*. [Online] Available <http://www.asu.edu/>
- 1.9 *University of Michigan*. [Online] Available <http://www.umich.edu/>
- 1.10 *Oak Ridge National Laboratory*. [Online] Available <http://www.ornl.gov/>
- 1.11 *The Remote Control of the Electron Microscope at Oak Ridge National Laboratory*. [Online] Available <http://www.epm.ornl.gov/~geist/java/applets/uscope/>
- 1.12 *Mozilla Firefox web browser website*. [Online] Available <http://www.mozilla.org/>
- 1.13 *Internet Explorer web browser website*. [Online] Available <http://www.mozilla.org/>
- 1.14 *Opera web browser website*. [Online] Available <http://www.opera.com/>
- 1.15 *The Four-Point Probe Furnace at Arizona State University*. [Online] Available <http://www.eas.asu.edu/~fppf/>
- 1.16 *The University of Michigan Electron Microbeam Analysis Laboratory (EMAL) website*. [Online] Available <http://emalwww.engin.umich.edu/>

- 1.17 Chin G. Jr. & Lansing C. S. (2004). Capturing and supporting contexts for scientific data sharing via the biological sciences collaboratory. *Proceedings of the 2004 ACM conference on computer supported cooperative work*. New York: ACM Press.: 409.
- 1.18 Pancerella C.M., Rahn L. A. & Yang C. L. (1999). The diesel combustion collaboratory: combustion researchers collaborating over the Internet. *Proceedings of the 1999 ACM/IEEE conference on supercomputing*, New York: ACM Press.
- 1.19 MacEachren A.M., Pike W., Yu C., Brewer I., Gahegan M., Weaver S.D. & Yarnal B. (2006). Building a geocollaboratory: Supporting Human–Environment Regional Observatory (HERO) collaborative science activities. *Computers, Environment and Urban Systems*. 30: 201.
- 1.20 Keahey K., Fredian T., Peng T., Schissel D.P., Thompson M., Foster I., Greenwald M. & McGunef D. (2002). Computational Grids in action: the National Fusion Collaboratory. *Future Generation Computer Systems*. 18: 1005.
- 1.21 McHarg Jr B.B., Casper T.A., Davis S. & Greenwood D. (1999). Tools for remote collaboration on the DIII-D National Fusion Facility. *Fusion engineering and design*, 43: 343.
- 1.22 *Curriculum 2005: Lifelong Learning for the 21st Century: A User's Guide*. [Online] Available <http://www.polity.org.za/govdocs/misc/curr2005.html>
- 1.23 *The Hitachi website*. [Online] Available http://www.hitachi-hitec.com/global/em/sem/sem_index.html
- 1.24 *The EDAX website*. [Online] Available <http://www.edax.com/products/xray.cfm>

- 1.25 *The Olympus Soft Imaging Solutions website*. [Online] Available
<http://www.soft-imaging.de/>
- 1.26 *The Silicon Graphics website*. [Online] Available <http://www.sgi.com/>
- 1.27 *The Sun Java website*. [Online] Available <http://java.sun.com/>
- 1.28 Van der Pauw L.J. (1958). A method of measuring specific resistivity and hall effect of discs of arbitrary shape. *Philips Research Reports*. 30:1.
- 1.29 Tannenbaum A.S. (1996). *Computer networks (3rd Edition)*. New Jersey: Prentice Hall.: 693.
- 1.30 Mayer J.W. and Lau S.S. (1990). *Electronic materials science: For integrated circuits in Si and GaAs*. New York: Macmillan Publishing Company.: 34.
- 1.31 Mayer J.W. and Lau S.S. (1990). *Electronic materials science: For integrated circuits in Si and GaAs*. New York: Macmillan Publishing Company.: 35.
- 1.32 *High temperature materials laboratory website*. [Online] Available
<http://www.ms.ornl.gov/htmlhome/>
- 1.33 *Digital Micrograph™ 3 Image Acquisition and Processing Software*. [Online] Available http://www.gatan.com/imaging/dig_micrograph.html
- 1.34 *The Global GRID Forum*. [Online] Available <http://www.gridforum.org/>
- 1.35 *Internet 2 Home*. [Online] Available <http://www.Internet2.org/>
- 1.36 Tannenbaum A.S. (1996). *Computer networks (3rd Edition)*. New Jersey: Prentice Hall.: 460-463.
- 1.37 Ferrari T., Ghisseli A. & Vistoli C. (2001). Quality of services for remote control in high-energy physics experiments: a case study. *Computer physics communications*, 140: 209-218.

CHAPTER TWO: USING INTERNET-ENABLED REMOTE INSTRUMENTATION TO STUDY THE THERMAL STABILITY OF DIFFUSION BARRIERS FOR SILVER METALLISATION

2.1 Introduction

In this chapter, diffusion barriers are discussed with the study of it by different experimental techniques (which will be further elaborated on in this chapter) in order to determine the efficiency of the chosen diffusion barriers. Diffusion barriers are very important in integrated circuit (IC) technology [2.1] because they are used to prevent interdiffusion and reaction between the metal lines and the underlying substrate. In integrated circuits (IC), the various electronic devices are interconnected with metal lines to carry current or transport charge [2.2]. These metal lines could for example be copper, which is currently used as the interconnect material, but reacts readily with the underlying silicon substrate. In order to prevent this reaction, a barrier layer is inserted between the copper and silicon. Diffusion barriers are deposited onto the silicon substrate before the deposition of aluminium (Figure 2.1). Different types of refractory metal compounds are used as diffusion barriers; examples include tungsten, tantalum or titanium nitrides. In the case of Al, spiking into the silicon substrate leads to electrical shorts and other problems at the junctions. One of the solutions to improve contact reliability is to place a diffusion barrier between Al and Si to prevent the dissolution of Si into the Al layer [2.2].

A diffusion barrier therefore separates material A and material B physically by interposing a layer of material X chosen so that the undesirable intermixing of A and B will be suppressed (Figure 2.2) [2.2].

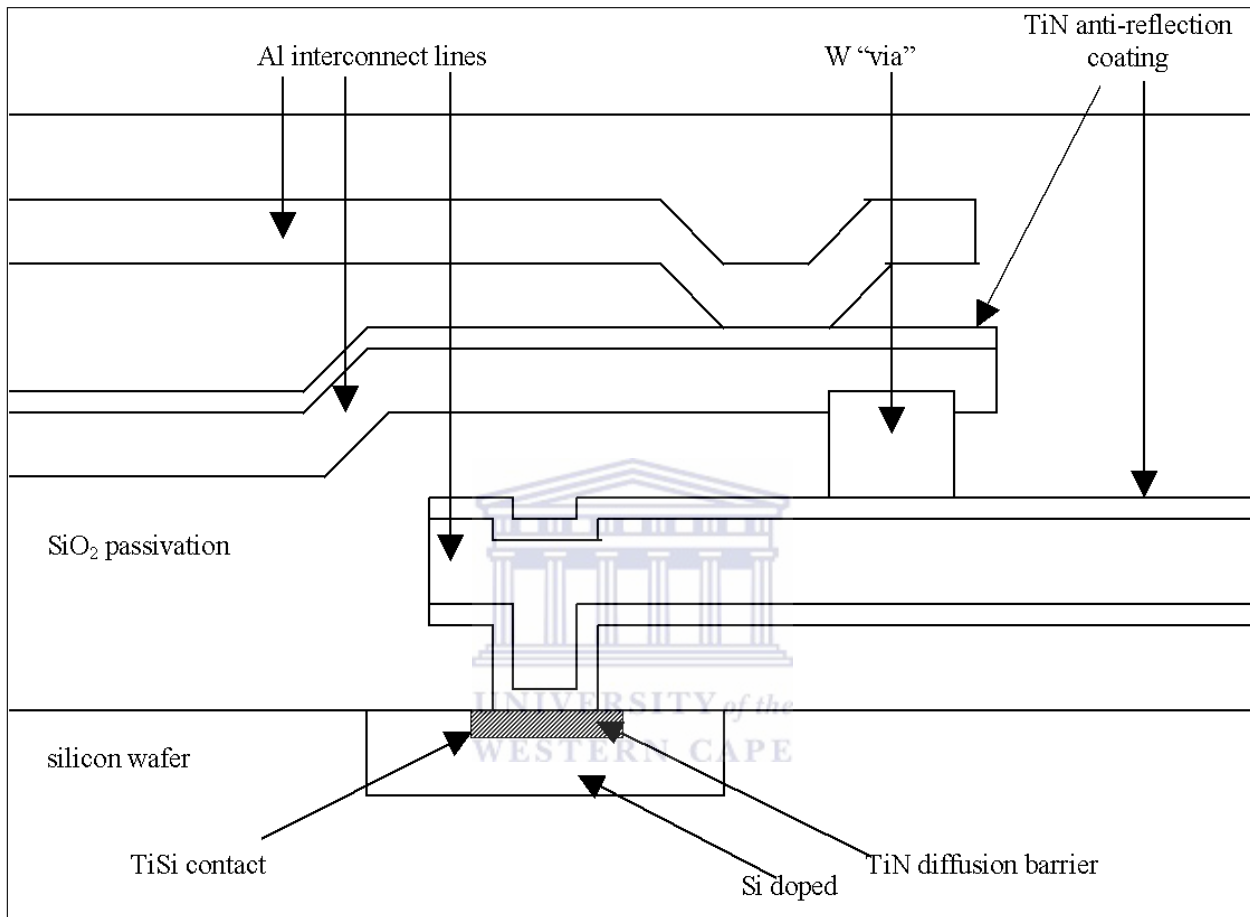


Figure 2.1: Illustration of the position of a diffusion barrier in a typical IC [2.3]

An ideal diffusion barrier should meet the following criteria:

- 1) The transport rate of A across X and of B across X should be small.
- 2) The loss rate of X into A and of X into B should be small.
- 3) X should be thermodynamically stable against A and against B.
- 4) There should be strong adhesion of X with A and with B [2.2].

- 5) The specific contact resistance of A to X and of X to B should be small.
- 6) X should be laterally uniform in thickness and in structure.
- 7) X should be resistant to mechanical and thermal stresses.
- 8) X should be highly conductive (thermal and electrical).

In reality not all the conditions can be met by one single diffusion barrier, therefore certain compromises will have to be made [2.4].

2.2 Different Types of Diffusion Barrier

2.2.1 Sacrificial barriers

A sacrificial barrier is where a barrier layer X reacts with A or B or both (Figure 2.2) in a laterally uniform manner with fully discernable rates. The separation of A and B needs to be in place at all times even though X reacts with A and B, implying that X must not be completely consumed. A typical example (Figure 2.4) is the use of a Ti layer between Al and Si to delay Al spiking. At 450 °C, Ti reacts negligibly with silicon but reacts with Al to form a uniform layer of $TiAl_3$.

Once the Ti is consumed the sacrificial barrier no longer performs its function [2.4]. Sacrificial barriers delay the metallisation failure with predictable lifetimes when the sacrificial reactions are well identified [2.5].

2.2.2 Stuffed barriers

While sacrificial barriers may provide adequate protection for the metallisation, they have a definite lifetime after which the barriers no longer function. For more permanent protection, the barrier layer X should be stable against A and B. The lack of thermodynamic driving force is not enough to make X a barrier; it is also necessary to

stop or reduce diffusion of A and B across X via short circuit paths. There are ways to achieve this: eliminate the short circuit paths, i.e. the grain boundaries, and plug the easy paths with appropriate atoms and molecules stuffing the barrier (Figure 2.3) [2.5].

In the Ti-Mo-Au system, molybdenum (Mo) and gold (Au) are mutually insoluble; there is no driving force for them to react. When the Mo and Ti are deposited under good vacuum conditions, the two metals intermix via grain boundaries. When Au is added to the top of the film, Au and Ti readily combine at 600 °C across the virtually unperturbed Mo layer. However, if Ti is exposed to oxygen before the Mo layer is deposited, intermixing between Ti and Mo is limited. The implication is that the Ti-Mo-Au barrier system owes its blocking capacity to the presence of oxygen, which plugs the easy paths in the Mo and the Ti layers [2.5].

2.2.3 Amorphous barriers

Another way to stop the easy diffusion paths is to eliminate the grain boundaries altogether by making the diffusion layer either single crystalline or amorphous in structure. Single crystalline barrier layers are impractical at present; the alternative solution of depositing amorphous layers appears to a feasible approach.

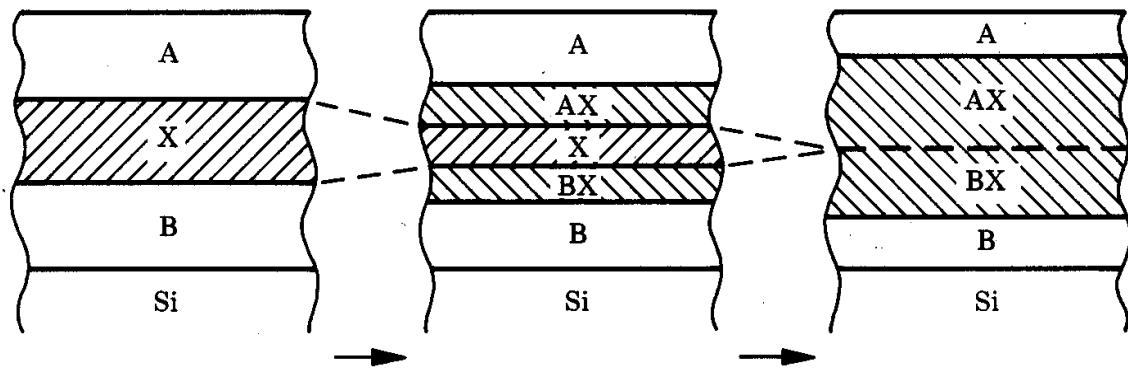


Figure 2.2: The different stages of a diffusion barrier X and how it reacts with the contact materials A and B [2.2]

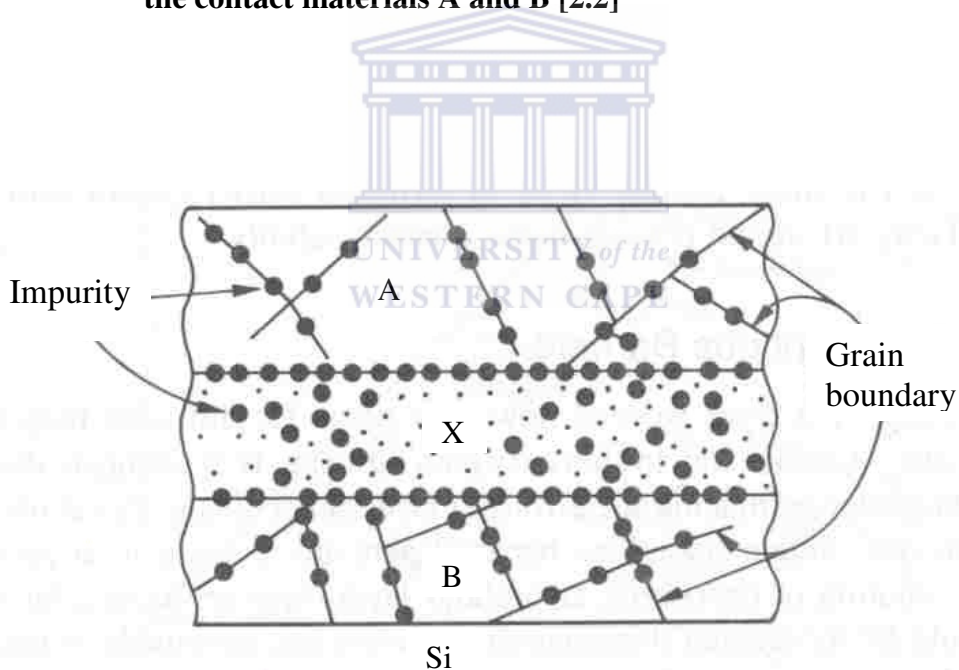


Figure 2.3: "Stuffed" barrier

Easy diffusion paths are plugged by suitable impurities; the stuffed barrier can successfully withstand the heat treatment [2.5]

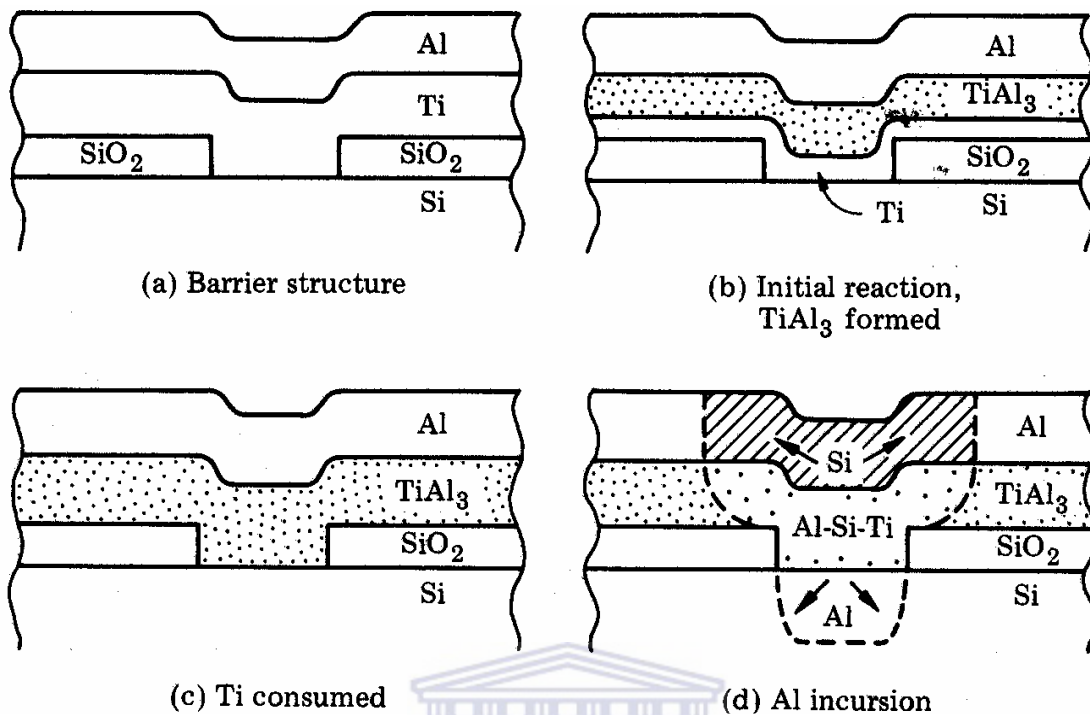


Figure 2.4: Amorphous barrier

- (a) The basic contact structure of Ti as a sacrificial barrier.
- (b) TiAl₃ starts forming over the entire structure.
- (c) At the point where the titanium has been completely consumed, the Ti-Si-Al ternary forms over the contact region.
- (d) Silicon begins diffusing into the Al while Al displaces the diffusing silicon in the contact hole. The TiAl₃ adjacent to the contact area serves as a place where most of the displaced silicon moves from the contact hole. This is mainly to extend the ternary region [2.4].

It should be recognised that amorphous layers are metastable in nature. When the amorphous layer crystallises into a polycrystalline film, easy diffusion paths are present again. It is also possible for the amorphous layer, X, to react with layers A and/or B; in

doing so the amorphous diffusion barrier becomes a sacrificial barrier [2.6]. During reaction the composition of the amorphous layer may change and may lead to a lowering of the crystallisation temperature [2.7].

2.3 Diffusion barriers for Ag metallisation

2.3.1 Introduction

Recently much research has been done to investigate silver as a potential alternative for Cu and Al interconnects. Silver (Ag) has the lowest resistivity of all candidate metals and has a lower reactivity than copper (Cu). Apart from reports showing that Ag reacts with Si converting all metallic silver at around 1 150 °C, there are no reports of Ag forming a silicide when it comes into contact with Si [2.8]. Ag is well known to show poor adhesion when deposited on oxides, and at low temperatures the case is no different. Ag sometimes exhibits signs of peeling when it is deposited on Si substrates and annealed at low temperatures [2.9]. Therefore, for Ag to be used as a suitable interconnect material, diffusion barriers had to be found to isolate the metal from the underlying substrate and prevent any interdiffusion. In this investigation three different types of materials, namely TiN, TaN and TiW were investigated as possible diffusion barriers for silver.

2.3.2 Using TaN, TiN and TiW as diffusion barriers for Ag

(a) Sample cleaning and deposition

Thermal oxidised silicon wafers with thin layers of TiN, TaN and TiW of about 100 nm were used. The TiN, TaN and TiW wafers were prepared by radio frequency (RF) sputtering [2.10] at Motorola [2.11]. These wafers were then cut into 1 cm x 1 cm squares and then ultrasonically cleaned with organic solvents. The cleaning sequence was as follows: 5 minutes in methanol, 5 minutes washing in acetone, 5

minutes washing in trichloroethylene, 5 minutes washing in acetone again, 5 minutes washing in methanol, followed by a rinse in deionised water. After cleaning, the 1 cm x 1 cm square samples were then mounted on circular aluminum discs, which acted as sample holders. A total of six sample holders could be loaded into the evaporation chamber at a time, giving the researcher the option of preparing six different structures. The sample holders were then loaded into the vacuum evaporation system for deposition.

The vacuum system (Figure 2.5) is divided into an upper part and lower part. The upper part is covered by a glass bell jar. Inside this bell jar are a quartz thickness monitor and a rotating sample holder. The lower section contains the turbomolecular pump, which is backed up by a rotary pump. After evacuation, depositions were carried out at pressures less than 10^{-5} Pa. These pressures were achieved by using four kinds of vacuum pumps. A pressure of 10 Pa was attained using a mechanical rotary pump and it was further reduced to about to 10^{-2} Pa using a turbo pump.

The pressure was further brought down to 10^{-5} Pa by using ion pumps. The lower sections also contain the electron gun, which has three crucibles. The electron gun consists of a tungsten filament, which produces electrons that are focused on the hearth by a magnetic field. The materials to be evaporated were placed in the three crucibles. Three materials could be deposited sequentially without breaking the vacuum. In the lower section were also a Ti-sublimation pump and a liquid nitrogen cold trap. During the evaporation liquid nitrogen was added to the cryopanel to freeze out some gases remaining in the chamber. The Ti-sublimation pump was used to keep the pressure as low as possible during evaporation. To achieve a good high vacuum, the pumping system was left to run

overnight prior to the deposition. Silver layers of approximately 200 nm were deposited by electron beam evaporation onto the three different substrates (TaN, TiW, TiN). The pressure rose to $\sim 1.07 \times 10^{-4}$ Pa during deposition.

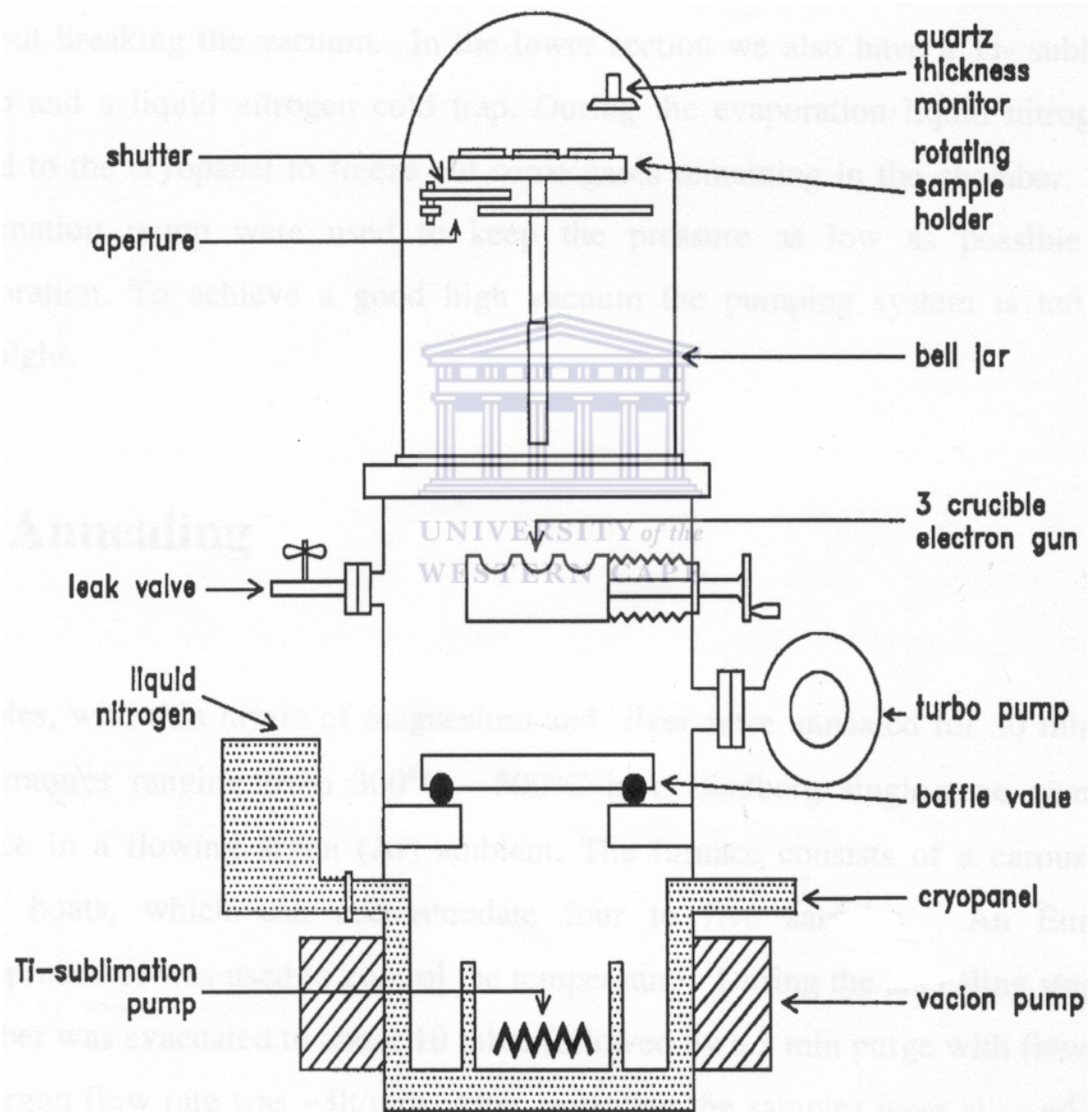


Figure 2.5: Schematic diagram of the high-vacuum system evaporator used for the deposition of the Ag layers onto the different barrier materials (TiN, TiW and TaN) [2.12]

(b) The techniques used

The Rutherford Backscattering Spectrometry (RBS) [2.13] analysis was performed using a 6 MV vertical, single-ended Van de Graaff accelerator using a 2.0 MeV $^4\text{He}^{2+}$ beam at iThemba Laboratories, Faure. The backscattering angle was 170° and the total accumulated charge was 10 – 20 μC . The samples were loaded into a vacuum chamber, which can hold 10 samples at a time. The incident $^4\text{He}^{2+}$ ions are elastically scattered by nuclei of the sample, providing a quantitative elemental depth profile. The computer-simulation program RUMP [2.14] was used for the simulation of the RBS spectra (see Appendix B for more detailed discussion of the theoretical concepts and principles of Rutherford Backscattering Spectrometry).

The four-point probe furnace [2.15] at ASU was used to measure the sheet resistance of the samples. The sheet resistance for the samples was measured with a ramp rate of 0.17 $^\circ\text{C}/\text{s}$. The sheet resistance of the Ag/TiN sample was measured off-line, whereas the other samples were measured via the Internet. The starting temperature of the furnace was room temperature (27 $^\circ\text{C}$) and the samples were annealed up to a temperature of 750 $^\circ\text{C}$. The current that was used to measure the sheet resistance was 50 μA . The vacuum inside the furnace at the start of the experiments was $\sim 4 \times 10^{-6}$ Pa, except in the case of Ag/TiN samples where the vacuum was $\sim 2.67 \times 10^{-8}$ Pa (see Chapter 1 for more detailed discussion of the four-point probe furnace).

The Hitachi X650 Scanning Electron Microscope (SEM) [2.16] in the Electron Microscopy Unit (EM Unit) at UWC was used to study the morphology of the samples. The microscope also has energy dispersive spectroscopy (EDS) and X-ray mapping capability. An emission current of 70 μA and a voltage of 25 keV were used in these analyses. A working distance of 15 mm was used during the imaging process. The

samples were coated with a thin gold layer to prevent charge build-up on the sample. The vacuum inside the microscope during analyses was $\sim 10^{-3}$ Pa. The secondary electron mode was used in the analyses of the morphology of the sample (see Appendix A for more detailed discussion of the scanning electron microscopy).

A D8 Advance Bruker diffractometer with a vertical goniometer was used to obtain the X-ray diffraction spectra [2.17]. The equipment used to detect the diffracted beam was a scintillation counter. The source of the monochromatic X-ray beam was a Cu tube. The wavelength of the Cu K_{α} radiation was 0.15 nm, generated at a voltage of 40 keV and a current of 30 mA. The system is equipped with a sample carrier that is capable of holding nine samples at a time. The step size used for the X-ray diffraction spectra was 0.05° . The spectra obtained were compared to those in the built-in database to determine the elements (see Appendix B for more detailed discussion of the X-ray diffraction). The techniques used and the information they provide of the thin film is summarised in Table 2.1 below.

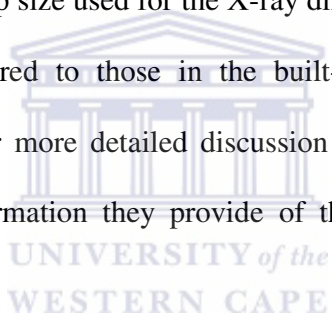


Table 2.1: Summary of the techniques used in thin films and the information provided

Technique	Information
RBS	<ul style="list-style-type: none"> • Elemental depth profiles • Film thickness
Resistivity Measurements	<ul style="list-style-type: none"> • Compound formation
SEM	<ul style="list-style-type: none"> • Surface morphology
XRD	<ul style="list-style-type: none"> • Phase and compound formation

2.4 Results

Two set of samples of Ag/TiN, Ag/TiW and Ag/TaN were annealed in vacuum, one was annealed in situ at ASU while another was annealed ex situ at iThemba Laboratories, Faure. The set that was annealed at ASU is further discussed under the heading ASU Vacuum Furnace while the set annealed at iThemba Laboratories is discussed under the heading iThemba Labs.

2.4.1 ASU vacuum furnace

Figure 2.6 shows a plot of the raw data as well as a linear fit of the sheet resistance versus annealing temperature of Ag (200 nm) on TiW sample annealed in the four-point probe furnace in a vacuum of 4×10^{-6} Pa, except in the case of the Ag/TiN samples where the vacuum was $\sim 2.67 \times 10^{-8}$ Pa. The results in the range 200 °C to 750 °C show an almost linear relationship between the sheet resistance and the annealing temperature.

However, below 400 °C the cooling curve deviates from the heating curve. This deviation may be due to poor contact between the sample and the probe as a result of the difference in the coefficient of thermal expansion (CTE). The plot of sheet resistance versus annealing temperature of the Ag on TaN sample shows a similar behaviour as the Ag on TiW (Figure 2.7) in that the cooling curve deviates from the heating curve. In order to maintain some neatness in the graph, as a huge number of readings are taken every second in the vacuum furnace, a feature in the plotting program Origin [2.18] is used to hide every 10 points, which produces the graphs in Figures 2.6 and 2.7.

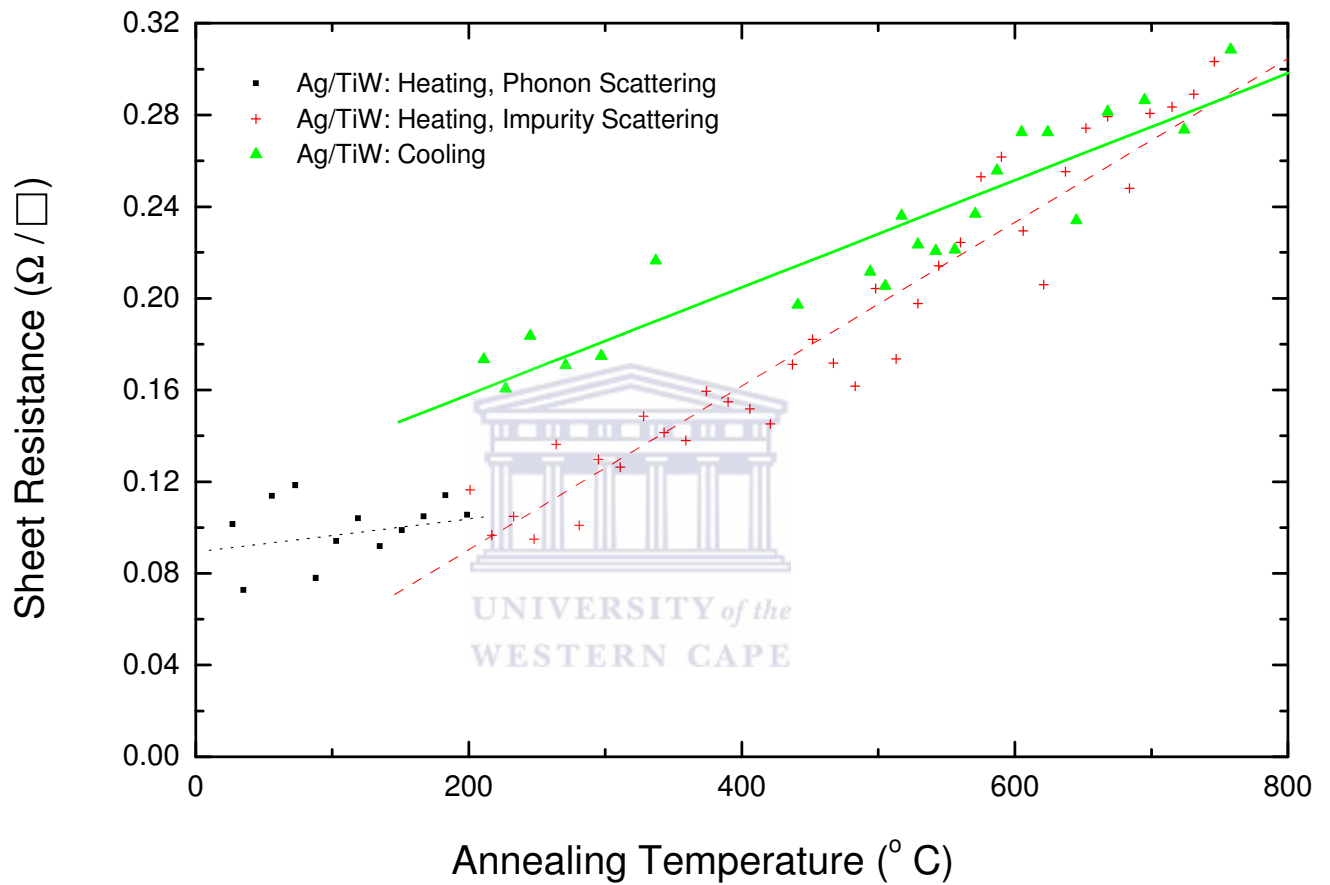


Figure 2.6: Plot of sheet resistance vs. annealing temperature of an Ag (200 nm)/TiW (200 nm) sample

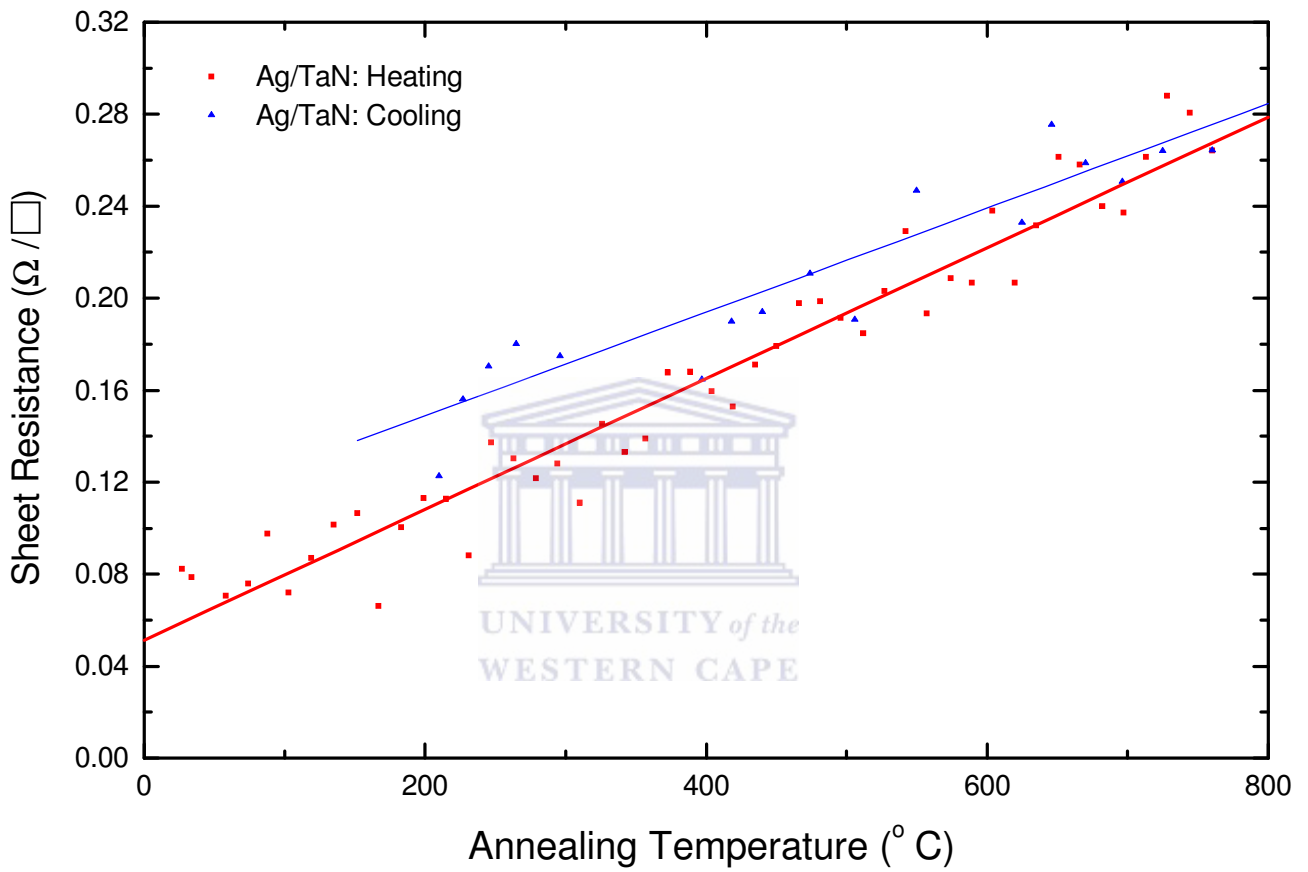


Figure 2.7: Plot of sheet resistance vs. annealing temperature of an Ag (200 nm)/TaN (200 nm) sample

Figure 2.8 shows the RBS spectra of Ag deposited on TiN before and after annealing at 750 °C in a furnace at a ramp rate of 0.17 °C/s. Apart from some possible interfacial roughness at the trailing edge, the two spectra are almost identical, which suggests that the barrier remains intact and no interdiffusion between Ag and the TiN occurred. Figures 2.9 and 2.10 contrast the RBS spectra of the as-deposited Ag on TiW and TaN respectively with that annealed in a vacuum furnace. The results again show no interdiffusion. In both cases the as-deposited samples are almost identical to the annealed samples.

In order to evaluate the surface morphology of the samples, scanning electron microscopy analyses were performed. In Figure 2.11(a) the SEM micrograph shows that the surface of the as-deposited sample of Ag on TiN is smooth. A SEM micrograph of an annealed sample of Ag on TiN (Figure 2.11(b)) shows that apart from localised Ag hillocks the surface is relatively smooth. The as-deposited samples of Ag on TiW (Figure 2.12(a)) show localised hillocks as well as a very few holes. The annealed samples of Ag on TiW (Figure 2.12(b)) show no features other than those observed in as-deposited samples.

Therefore, the surface morphology for both the as-deposited and annealed samples is basically the same. The surfaces of the as-deposited and annealed Ag/TaN samples (Figure 2.13) show similar features to the Ag/TiN and Ag/TiW samples. Almost no hillocks are present on the Ag/TiW and Ag/TaN annealed samples.

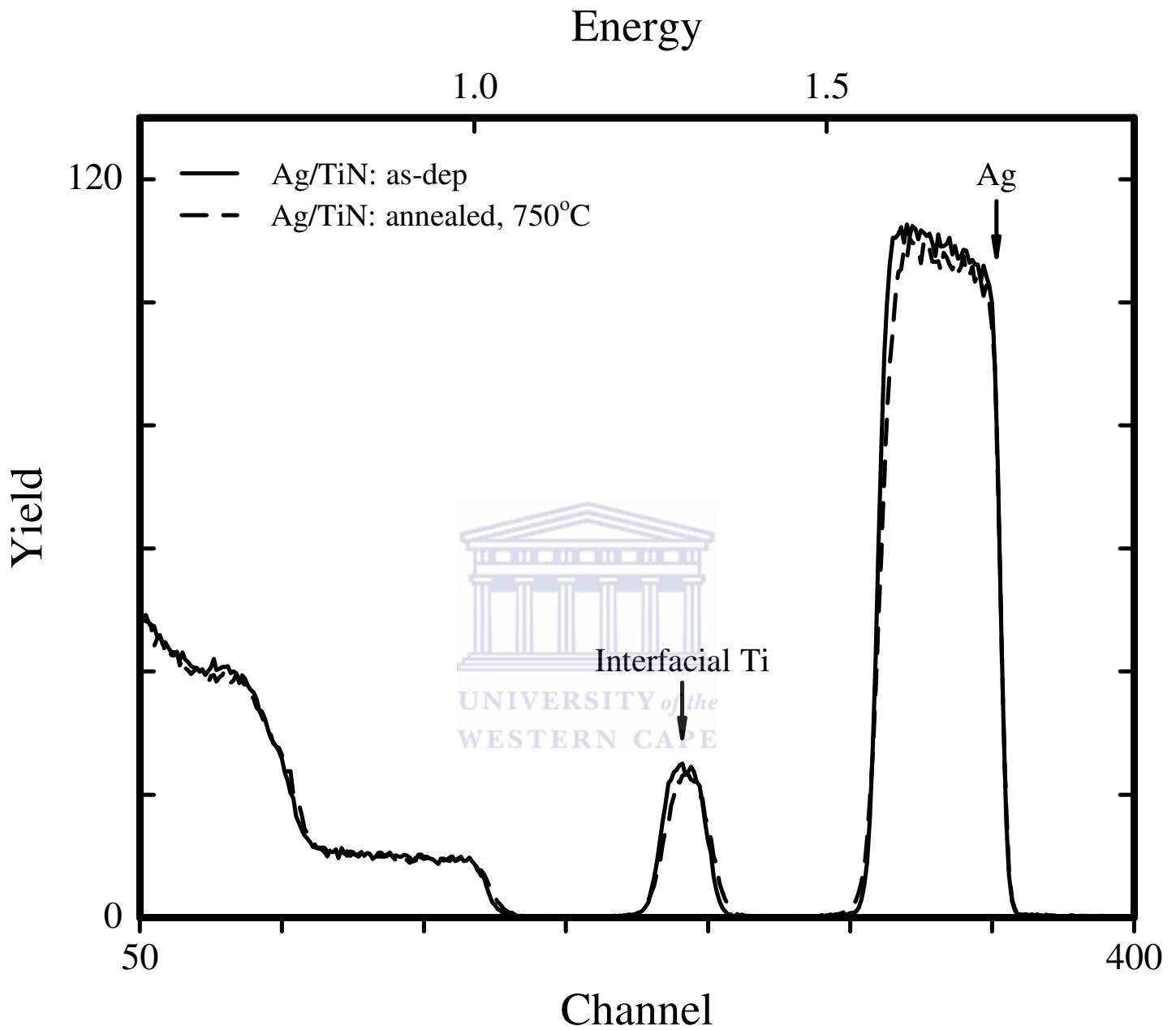


Figure 2.8: The RBS spectrum of an as-deposited Ag (200 nm)/TiN (200 nm) sample compared with sample annealed in vacuum until 750 °C. A 2.0 MeV ${}^4\text{He}^{2+}$ beam energy was used.

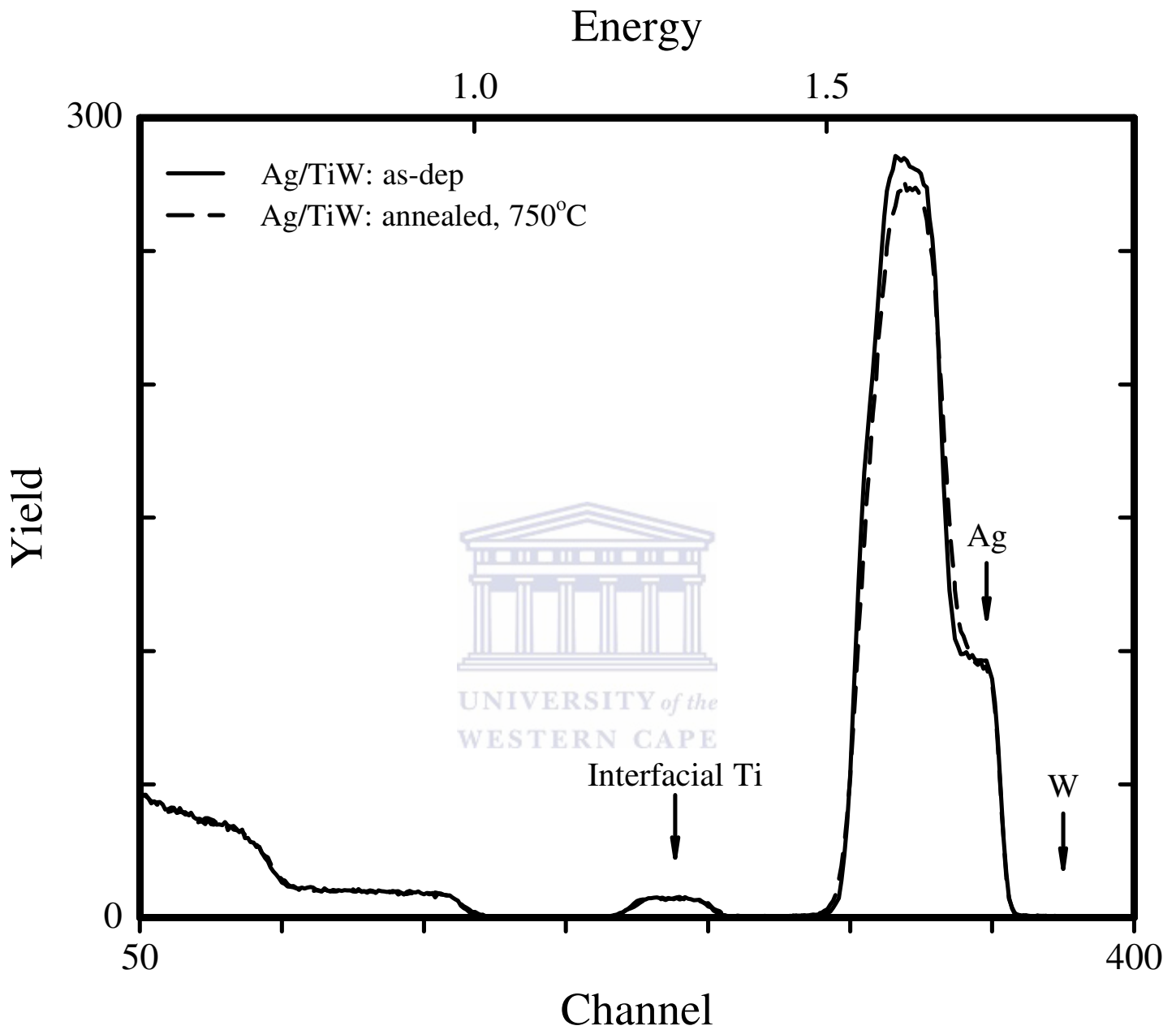


Figure 2.9: The RBS spectrum of an as-deposited Ag (200 nm)/TiW (200 nm) sample compared with sample annealed in vacuum until 750 °C.

A 2.0 MeV $^4\text{He}^{2+}$ beam energy was used.

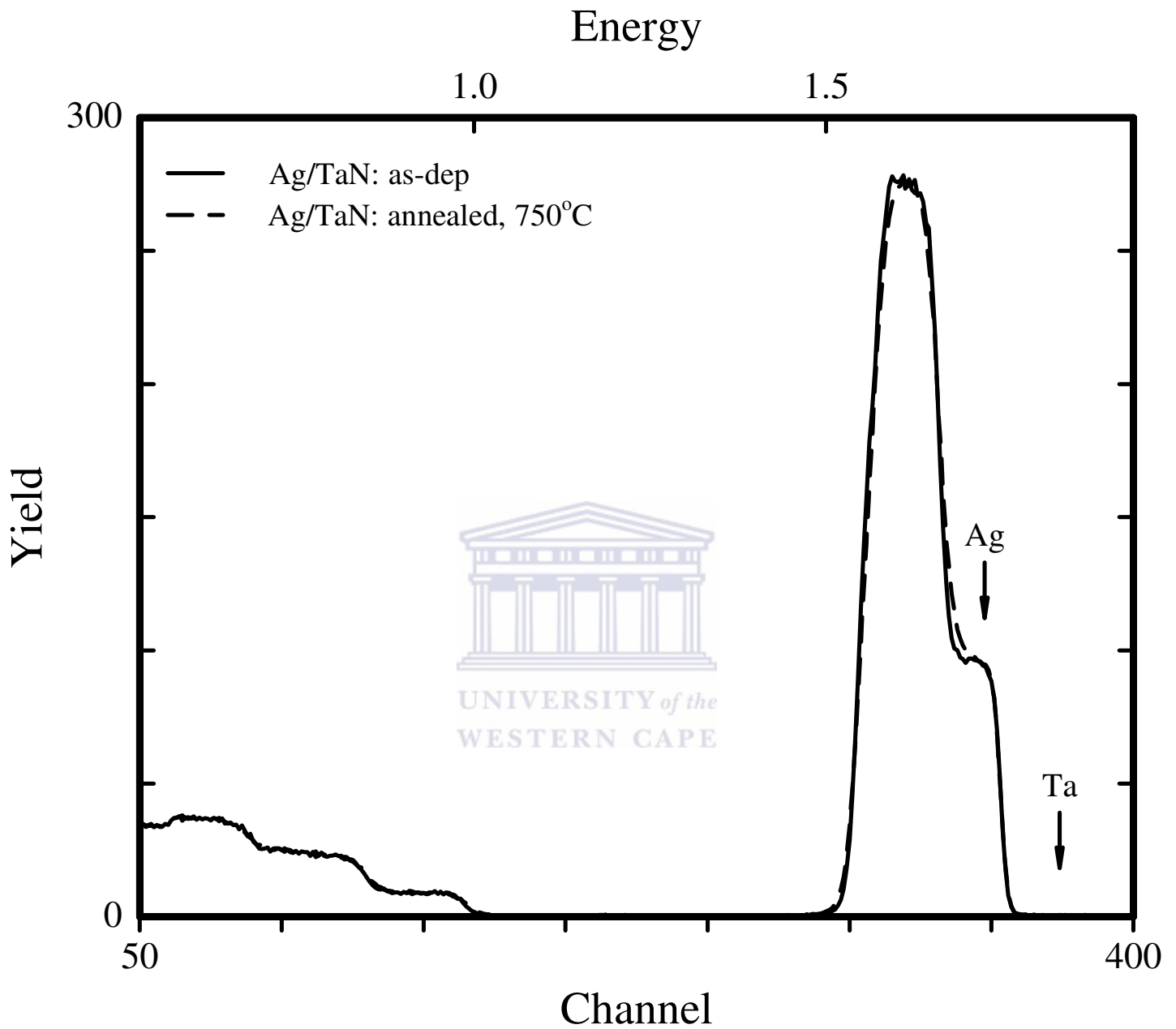


Figure 2.10: The RBS spectrum of an as-deposited Ag (200 nm)/TaN (200 nm) sample compared with a sample annealed in vacuum until 750 °C. A 2.0 MeV $^4\text{He}^{2+}$ beam energy was used.

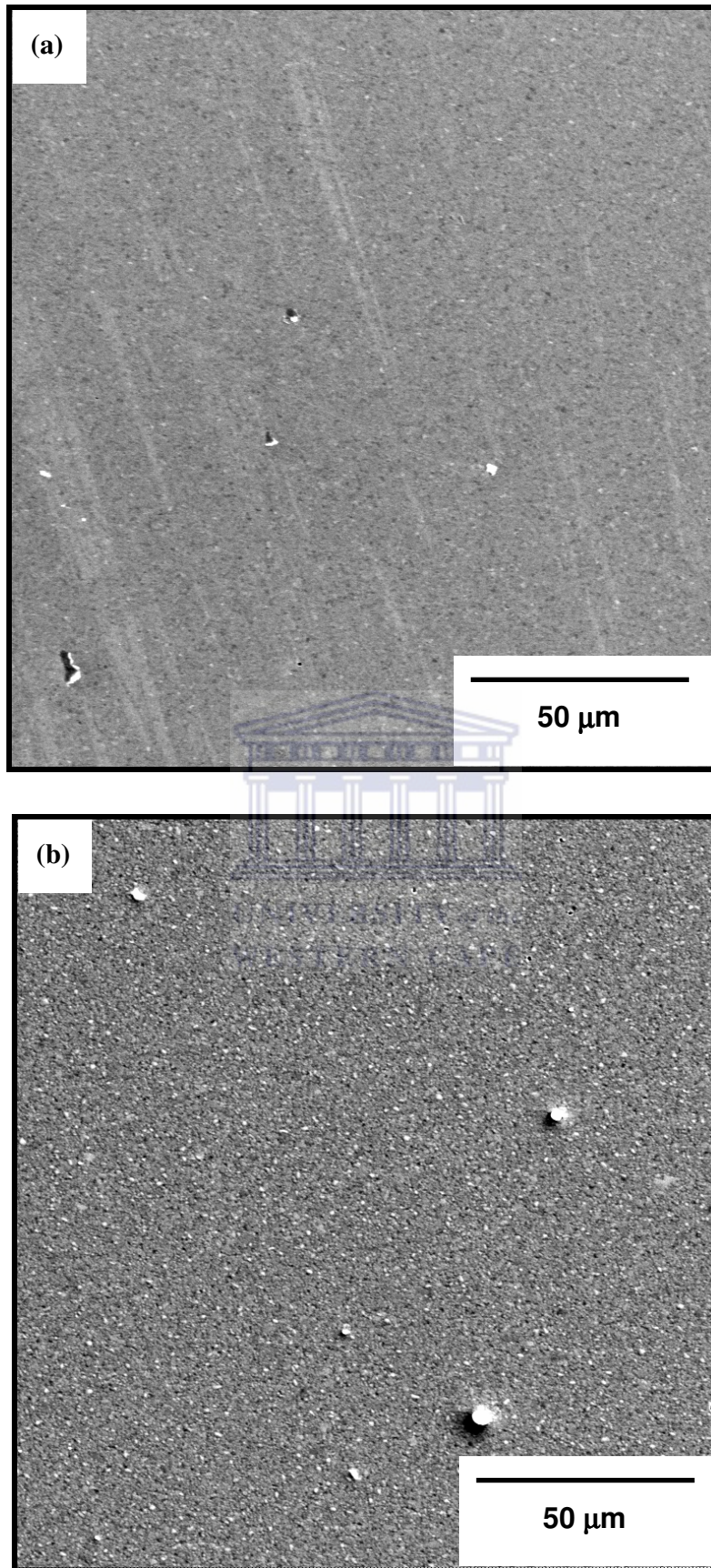


Figure 2.11 SEM Micrograph of (a) an as-deposited Ag (100nm) / TiN (200nm) sample, and (b) a sample annealed in vacuum till 750 °C.

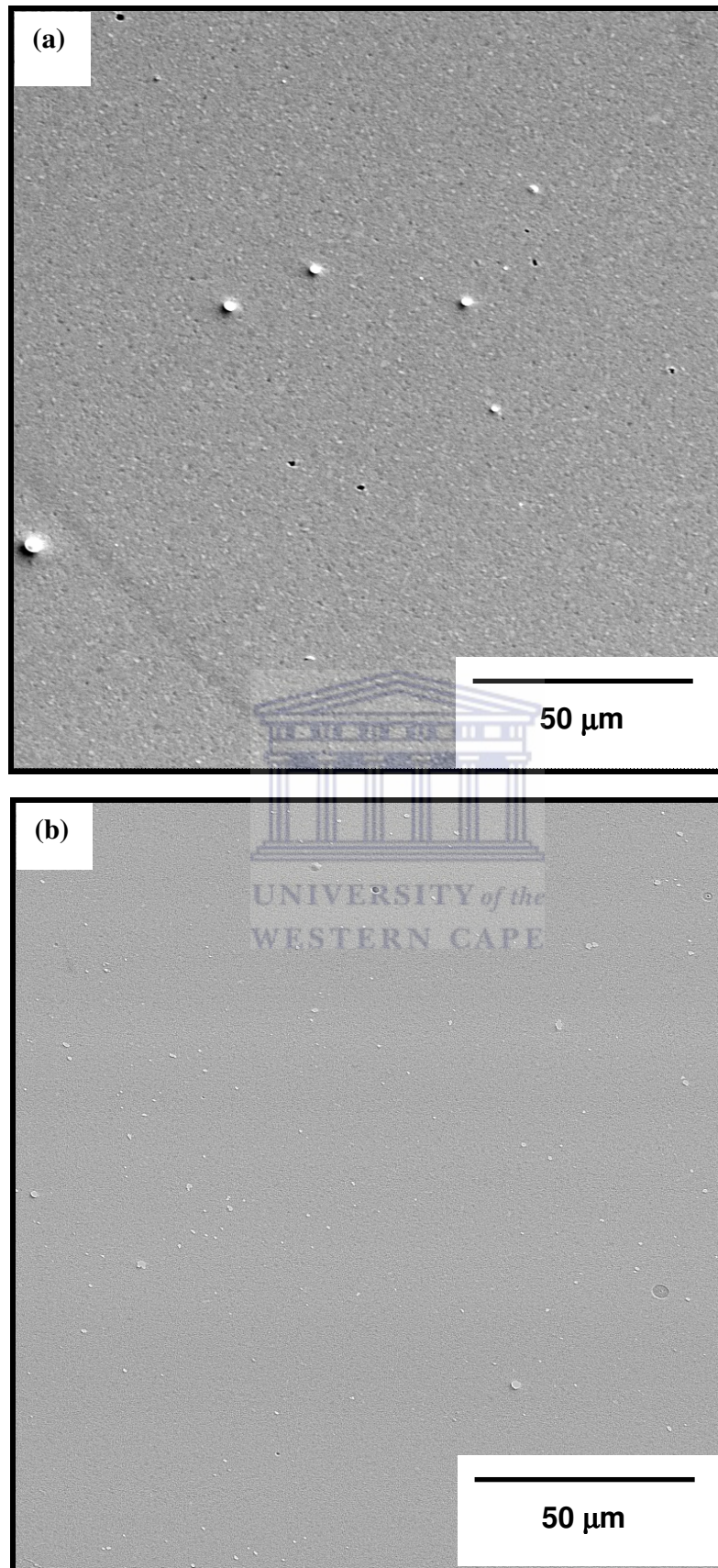


Figure 2.12 SEM Micrograph of (a) an as-deposited Ag (100nm) / TiW (200nm) sample, and (b) a sample annealed in vacuum till 750 °C.

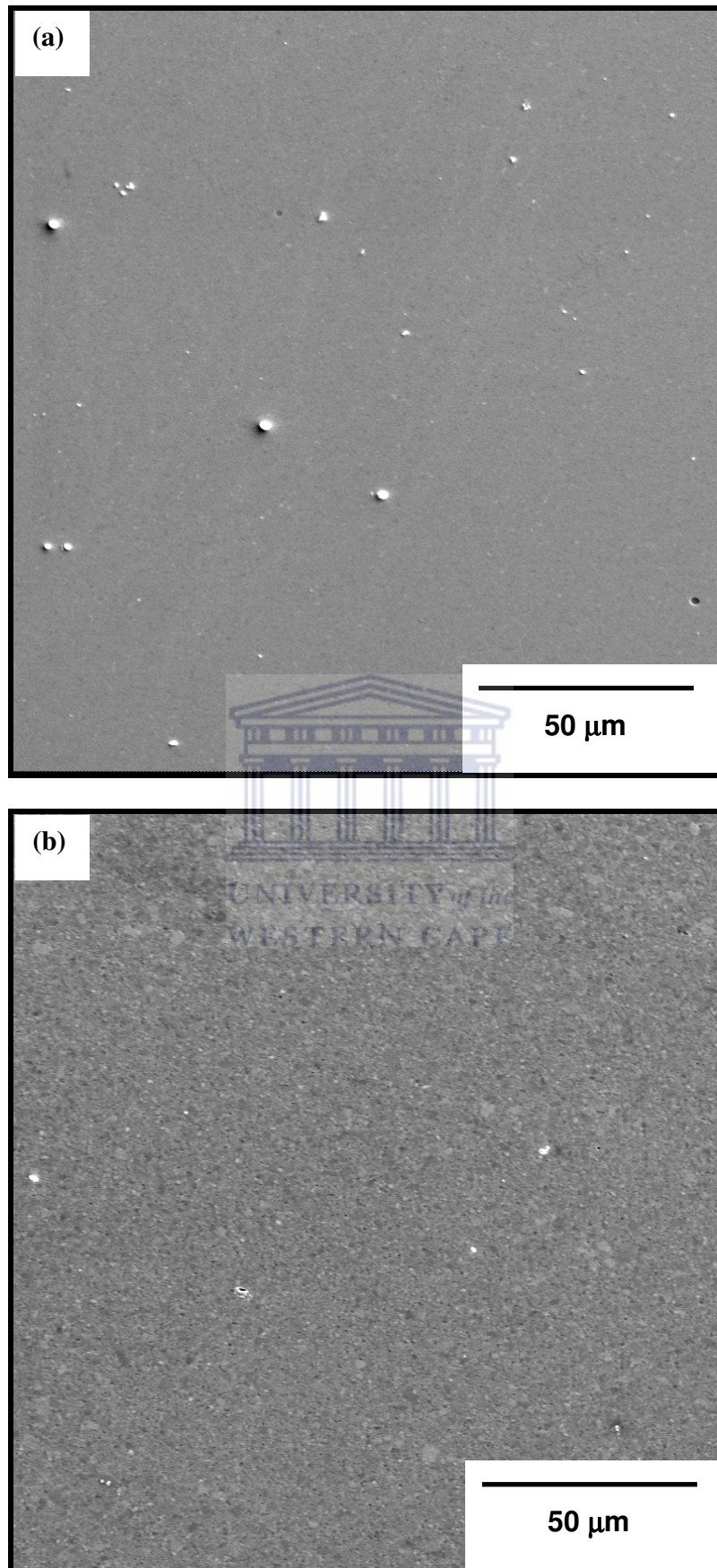


Figure 2.13 SEM Micrograph of (a) an as-deposited Ag (100nm) / TaN (200nm) sample, and (b) a sample annealed in vacuum till 750 °C.

2.4.2 iThemba Laboratories

Three types of analysis were done on the set of samples of Ag/TaN, Ag/TiN and Ag/TiW that were annealed ex situ in vacuum for 30 minutes at 650 °C, namely X-Ray Diffraction (XRD), Rutherford Backscattering Spectrometry and resistivity measurements. The RBS spectra of the ex situ annealed samples were identical to the spectra of in situ annealed samples and are therefore not included. The set of samples were annealed ex situ at iThemba Laboratories, Faure.

Figure 2.14 compares XRD spectra of the Si substrate, the as-deposited Ag on TiN and the spectra of samples annealed in vacuum at 650 °C for 30 minutes. It can clearly be seen that the Si peaks did not overlap with the Ag peaks. It is observed that the intensity of the Ag peaks in the annealed samples increased compared to the as-deposited sample. Apart from the increase in the intensity of the Ag peaks in the annealed samples, no new intermetallic formation occurred, which suggests that the diffusion barrier successfully prevents interdiffusion or compound formation. Similar results were obtained for Ag deposited on TiW (Figure 2.15) and TaN (Figure 2.16). In both situations the barrier did well in preventing interdiffusion and intermetallic formation between the Ag and the underlined diffusion barrier. There was no shift in the Ag peaks and therefore no intermetallic or compound formation occurred.

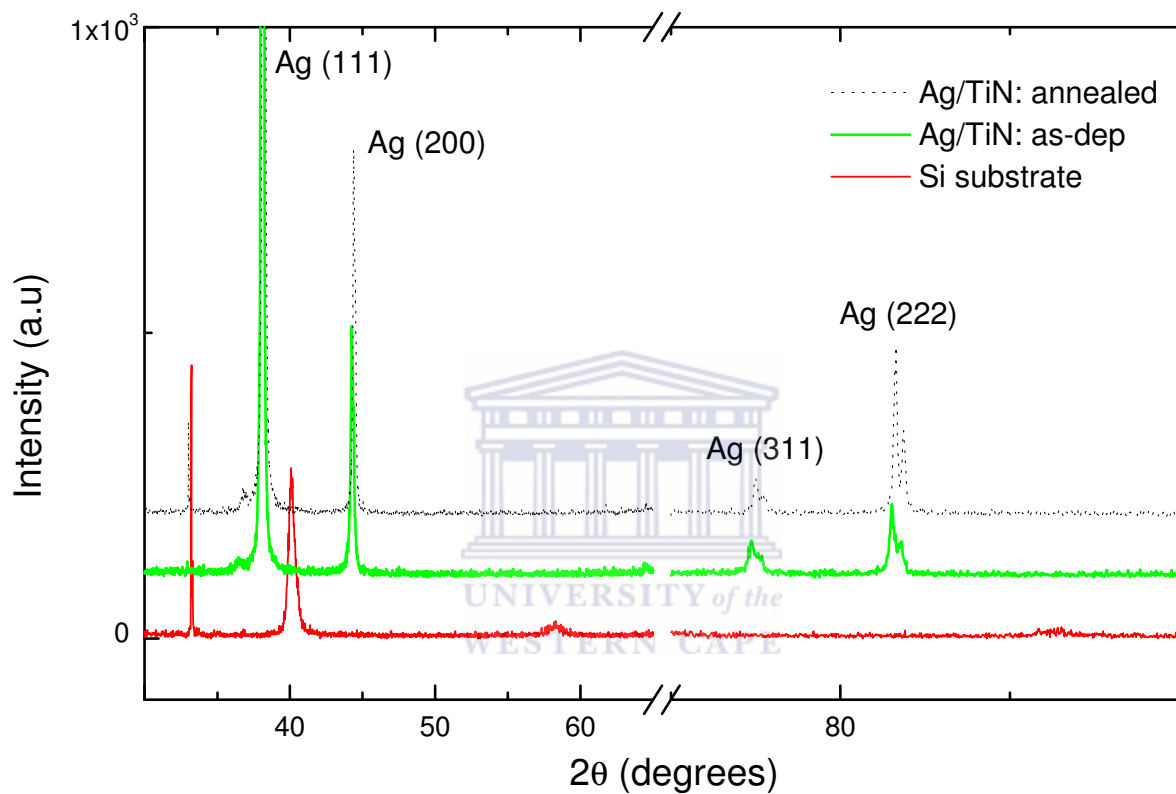


Figure 2.14: XRD spectra of the Si substrate, and the as-deposited and annealed Ag (200 nm)/TiN (200 nm) sample

The Ag (200 nm)/ TiN (200 nm) sample was annealed at 650 °C for 30 minutes

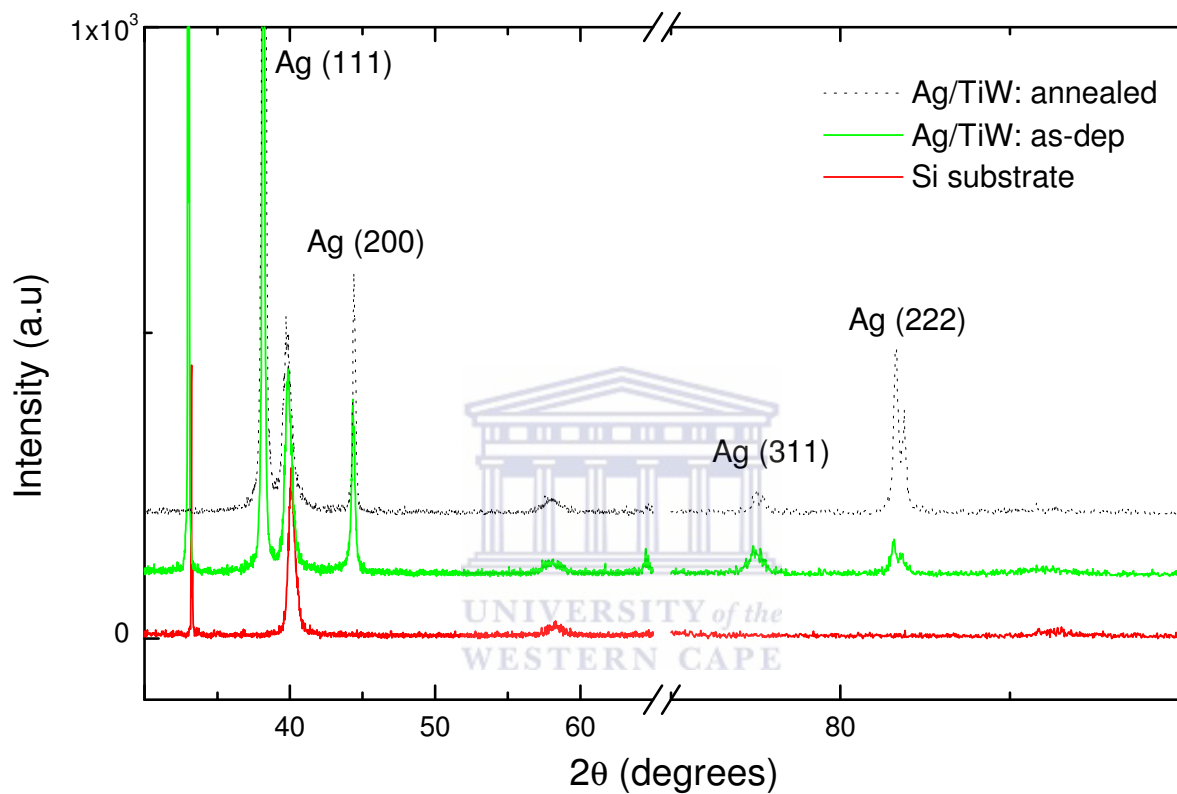


Figure 2.15: XRD spectra of the Si substrate, and the as-deposited and annealed Ag (200 nm)/TiW (200 nm) sample

The Ag (200 nm)/TiW (200 nm) sample was annealed at 650 °C for 30 minutes

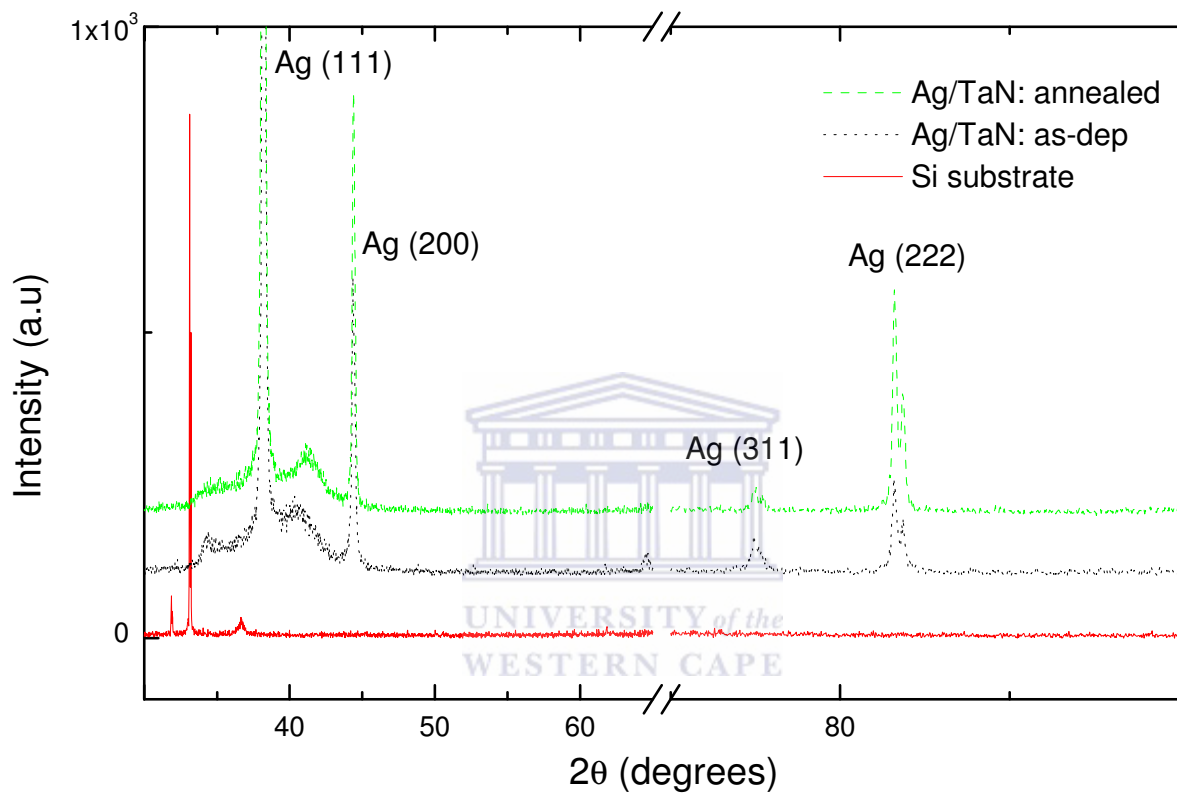


Figure 2.16: XRD spectra of the Si substrate, the as-deposited and annealed Ag (200 nm)/TaN (200 nm) sample

The Ag (200 nm)/TaN (200 nm) sample was annealed at 650 °C for 30 minutes

Tables 2.2 to 2.5 show the resistivity measurements taken at the Physics Department, University of the Western Cape. The resistivity of the as-deposited samples measured in the four-point probe furnace at ASU and at UWC are approximately the same and are comparable. However, the resistivity measurements of the in-situ samples are nearly twice as great as those of the ex-situ annealed samples. The resistivity measurements for the Ag/TiW samples is well within $11.3 \mu\Omega\cdot\text{cm}$, which means that less than 1% of Ti resides in Ag. The reason for this could be that the samples undergo thermal stress in the case of the four-point probe furnace and have been in the furnace for a long time by the time they reach $650 \text{ }^\circ\text{C}$. However, in the case of the ex-situ annealed samples, the samples have only remained for 30 minutes in $650 \text{ }^\circ\text{C}$ vacuum ambient. The resistivity at ASU was read while the samples were at $650 \text{ }^\circ\text{C}$, while the ex-situ annealed samples were given time to cool down to room temperature before their resistivity measurements were taken.

Table 2.2: List of the resistivity measurements for the as-deposited and annealed TiN sample in vacuum at $650 \text{ }^\circ\text{C}$ for 30 minutes

TiN				
	As-deposited	Annealed	As-deposited	Annealed
Current (mA)	Voltage (mV)	Voltage (mV)	Sheet Resistance (Ω)	Sheet Resistance (Ω)
1	0.024	0.022	0.109	0.100
10	0.220	0.210	0.100	0.100
100	2.250	2.080	0.102	0.094
		Average	0.103	0.096
		Standard Deviation	0.005	0.003

Table 2.3: List of the resistivity measurements for the as-deposited and annealed TaN sample in vacuum at 650 °C for 30 minutes

TaN				
	As-deposited	Annealed	As-deposited	Annealed
Current (mA)	Voltage (mV)	Voltage (mV)	Sheet Resistance (Ω)	Sheet Resistance (Ω)
1	0.037	0.027	0.168	0.122
10	0.380	0.258	0.172	0.117
100	3.800	2.560	0.172	0.116
		Average	0.171	0.118
		Standard Deviation	0.003	0.003

Table 2.4: List of the resistivity measurements for the as-deposited and annealed TiW sample in vacuum at 650 °C for 30 minutes

TiW				
	As-deposited	Annealed	As-deposited	Annealed
Current (mA)	Voltage (mV)	Voltage (mV)	Sheet Resistance (Ω)	Sheet Resistance (Ω)
1	0.026	0.028	0.118	0.127
10	0.240	0.270	0.109	0.122
100	2.410	2.680	0.109	0.121
		Average	0.112	0.124
		Standard Deviation	0.005	0.003

Table 2.5: List of the resistivity measurements for the as-deposited and annealed TiN, TaN and TiW samples in vacuum at 650 °C for 30 minutes

Type of diffusion barrier	The sheet resistance of the as-deposited sample (Ω)	Standard Deviation (Ω)	The sheet resistance of the annealed sample (Ω)	Standard Deviation (Ω)
TiN	0.103	0.005	0.096	0.003
TaN	0.171	0.003	0.118	0.003
TiW	0.112	0.005	0.124	0.003

2.5 Discussion

2.5.1 ASU vacuum furnace

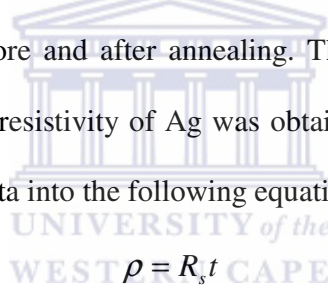
The RBS results suggest that the barrier remains intact for the temperature range 200 °C to 750 °C. However, by plotting the best fit through the data of resistance versus annealing time, the Ag/TiW curve (Figure 2.9) shows a slight change in the slope at about 200 °C. The change in slope and hence a change in resistivity may be due to the incorporation of impurities or microstructural changes in the Ag. The data suggest that the first line is a result of phonon scattering and the second line is a result of both impurity and phonon scattering. It is believed that impurity scattering is predominant in the data that fit the second line [2.19]. The slope in which the impurity scattering dominates is compared with that of the coefficient of resistivity of pure silver. The coefficient of pure silver is $3.8 \times 10^{-3} \Omega/^{\circ}\text{C}$ [2.20]. The presence of the impurities may either be a result of failure of the barrier or the subsequent reaction between the Ag and the barrier elements Ti and W. This reaction may lead to the formation of stable phases or solid solutions. By applying Hume-Rothery's rules the possibility of a solid solution between Ti and Ag exists [2.21, 2.22]. The Hume-Rothery rules are elaborated on later in this section. The coefficient of resistivity of Ag was calculated from experimental data by plotting the resistivity versus temperature, and was found to be $3.57 \times 10^{-4} \Omega/^{\circ}\text{C}$ (Figure 2.6). Matthiessen's Rule states that the resistivity of pure metals and dilute alloys can be separated into two components [2.23]:

$$\rho_{\text{total}} = \rho_{\text{phonon}} + \rho_{\text{residual}}$$

Where ρ_{total} is the total resistivity, ρ_{phonon} is the temperature-dependent electron-phonon contribution, and the ρ_{residual} is the residual resistivity. The residual contribution arises from electron scattering by impurities and structural imperfections such as grain boundaries, dislocations and vacancies [2.24]. The presence of refractory metal solute

atoms in the Ag matrix leads to additional electron scattering centres and hence a higher resistivity than the elemental values. The need to avoid the diffusion of Ti into Ag therefore arises and will be discussed in more detail later on. In the following two paragraphs it will be shown that firstly no Ti diffused in Ag, and secondly W and Ag could not have formed a solid solution.

According to dilute alloy theory, Ag resistivity is very sensitive to Ti diffusing into it, and the resistivity of Ag will increase by $9.7 \mu\Omega\cdot\text{cm}$ for every 1 atomic percent of Ti [2.25]. The resistivity of pure silver is $1.61 \mu\Omega\cdot\text{cm}$ [2.19]. The thickness of the deposited layers before and after annealing as well as the composition of the samples was determined using the simulation software RUMP [2.14]. It was found that the size of the Ag layer remained at 200 nm both before and after annealing. The sheet resistance, R_s , read off Figure 2.6, was taken and the resistivity of Ag was obtained from the experimental data determined by placing these data into the following equation:



The logo of the University of the Western Cape, featuring a classical building facade with columns and a pediment, with the text 'UNIVERSITY of the WESTERN CAPE' below it.

$$\rho = R_s t$$

It was found quite clearly that no Ti diffused into Ag. The resistivity of the end point of the second line in Figure 2.6 was found to be $6.4 \mu\Omega\cdot\text{cm}$. This resistivity of Ag was found to be much lower than the resistivity of 1 atomic percent of Ti in Ag and the resistivity of Ag added together, which meant that less than 1 atomic percent of Ti diffused into Ag. Furthermore, the sheet resistance of Ag at the end point of the second line in Figure 2.6 had to be 0.565Ω in order for the resistivity of Ag to be $11.3 \mu\Omega\cdot\text{cm}$. This is not the case and therefore approximately 0.56% (less than 1%) of Ti diffused into Ag. It is therefore reasonable to believe that the Ti present in the Ag exists in elemental form and not as a solid solution, which otherwise would have resulted in a dramatic increase in the resistivity of Ag.

According to the Hume-Rothery rules [2.21, 2.22] two elements cannot form a solution if their atomic radii difference is greater than 15%, which means that tungsten (W has an empirical radius of 135 picometres [2.26]) could not have formed a solid solution with Ag (Ag has an empirical radius of 160 picometres [2.26]).

The microscopy analysis revealed no changes in morphologies of the surfaces, apart from localised Ag hillocks formed as a result of surface diffusion of the silver. Malgas et al. [2.27] reported that the hillock formation results in an accumulation of Ag at one point and a depletion at another, and that this extensive depletion results in hole formation. Sharma et al. [2.28, 2.29, 2.30] investigated hillock formation, hole growth and agglomeration using SEM and TEM and discovered that hillock formation in silver films annealed in vacuum can be explained by thermal stress relaxation by diffusion creep. It is generally considered that tensile stresses within a thin film can enhance hole formation or agglomeration, while compressive stresses often lead to hillock formation [2.31]. The inference from the SEM micrographs, resistance measurements and the RBS spectra of the three diffusion barriers, namely TiN, TiW and TaN, shows that the diffusion barriers performed well against the diffusion of Ag. It must be noted that the barriers were exposed to air before the silver deposition. In the literature it has been shown that any surface oxide between the barrier and the metal overlayer may hinder interdiffusion, as the oxygen atoms block grain boundaries to enhance barrier layer characteristics [2.32, 2.33, 2.34].

2.5.2 iThemba Laboratories

The RBS showed similar results to those of the in-situ annealed samples and therefore were not included. The resistivity measurements were similar to those of the in-situ annealed samples and showed no interdiffusion of Ti into Ag. The resistivity did not

increase markedly and the explanation using Hume-Rothery rules and Mathiessen's rule to show this also holds true here. The resistivity was different (as can be seen from Tables 2.2, 2.3, 2.4 and 2.5) to that of the in-situ annealed samples, but that could be due the generation of thermal stresses and the fact that the samples were allowed to cool down to room temperature.

The XRD showed no shifting which also means that no intermetallic or compound formation took place.

2.6 Conclusion

The one set of TiN, TiW and TaN samples was annealed in situ in vacuum at ASU, while the other set was annealed ex situ at iThemba Laboratories in Faure. The in-situ samples were annealed up to 750 °C, while the ex-situ samples were annealed to 650 °C. The in-situ annealed samples were analysed by Rutherford Backscattering Spectrometry, SEM and resistance measurements, while the ex-situ annealed samples were analysed with Rutherford Backscattering Spectrometry, XRD measurements and resistance measurements. These analyses revealed that the silver on different diffusion barriers prevented any interdiffusion between the metal overlayer and the barrier or any phase formation from occurring. Therefore the TiN, TaN and TiW diffusion barriers remained intact for the temperature range 200 °C to 750 °C for the in-situ samples. Similarly, the barriers remained intact for the ex-situ annealed samples that were annealed at 650 °C for 30 minutes. Therefore the TiN, TiW and TaN samples proved to be an effective barrier for Ag in both scenarios.

2.7 References – Chapter 2

- 2.1 Mayer, J.W. & Lau, S.S. (1990). *Electronic materials science: for integrated circuits in Si and GaAs*. New York: Macmillan Publishing Company: 329.
- 2.2 Mayer, J.W. & Lau, S.S. (1990). *Electronic materials science: for integrated circuits in Si and GaAs*. New York: Macmillan Publishing Company: 10.
- 2.3 Peercy, P.S. (2000). The drive to miniaturization. *Nature magazine*, 406 (31): 1025.
- 2.4 Mayer, J.W. & Lau, S.S. (1990). *Electronic materials science: for integrated circuits in Si and GaAs*. New York: Macmillan Publishing Company: 330.
- 2.5 Mayer, J.W. & Lau, S.S. (1990). *Electronic materials science: for integrated circuits in Si and GaAs*. New York: Macmillan Publishing Company: 331.
- 2.6 Mayer, J.W. & Lau, S.S. (1990). *Electronic materials science: for integrated circuits in Si and GaAs*. New York: Macmillan Publishing Company: 332-333.
- 2.7 Mayer, J.W. & Lau, S.S. (1990). *Electronic materials science: for integrated circuits in Si and GaAs*. New York: Macmillan Publishing Company: 333.
- 2.8 Widdra, W., Fink, A., Gokhale, S., Trischberger, P., Gutdect, U., Birkenheuer, U., Rosch, N. & Menzel, D. (1998). One-Dimensional Delocalized Adsorbate Bloch States on a Semiconductor Surface: C₂H₄/Si(001)-(2×1). *Phys. rev. lett.* 80: 4269.
- 2.9 Murarka, S.P., Gutmann, R.J., Kaloyeros, A.E. & Lanford, W.A. (1993). Advanced multilayer metallization schemes with copper as interconnect metal. *Thin solid films*, 236: 257.
- 2.10 Chapman, B. (1980). *Glow discharge processes: sputtering and plasma etching*. New York: Wiley Interscience Publishers.

- 2.11 *The Motorola Website*. [Online] Available <http://www.motorola.com/>
- 2.12 Malgas, G.F., (1999). *Silver-magnesium thin film interactions in an oxidising ambient*. MSc Dissertation, University of the Western Cape: 11.
- 2.13 Chu, W.K., Mayer, J.W. & Nicolet M.A. (1978). *Backscattering spectrometry*. New York: Academic Press.
- 2.14 Doolittle, L.R. (1985). Algorithms for the rapid simulation of Rutherford backscattering spectra. *Nucl. inst. meth. res.*, B9: 344.
- 2.15 Smits, F.M. (1958). Measurement of Sheet Resistivities with Four-Point Probe. *The Bell System Technical Journal*, 37: 711-718.
- 2.16 Postek, Jr. M. (1980). *Scanning electron microscopy: a student's handbook*. Ladd Research Industries, Inc.
- 2.17 Nuffield, E.W. (1966). *X-ray diffraction methods*. New York: John Wiley & Sons, Inc.
- 2.18 *The Microcal software website*. [Online] Available <http://www.microcal.com/>
- 2.19 Kittel, C. (1976). *Introduction to solid state physics*. New York: Wiley Publishers: 148-151.
- 2.20 Halliday, D. & Resnick, R. (1978). *Physics. Part 1 & 2. Combined edition*. (3rd Edition). New York: John Wiley & Sons, Inc.: 679.
- 2.21 Avner, S.H. (1974). *Introduction to physical metallurgy*. New York: McGraw-Hill Publishers: 152.
- 2.22 Ali Omar, M. (1996). *Elementary solid state physics*. London: Addison Wesley Publishers: 543.
- 2.23 Matthiessen, A. & Vogt, C. (1864). *Pogg. ann. phys. chem.*, 122: 19.

- 2.24 Adams, D. (1996). *Refractory metal nitride self-encapsulation and thermal stability issues in copper and silver metallization*. PhD dissertation, Arizona State University: 140.
- 2.25 Bass, J. (1982). *Electrical Resistivity of pure metals and dilute alloys*. Landolt-Bornstein Tables, New Series, III/15a, Berlin: Springer-Verlag Publishers: 169.
- 2.26 Slater, J.C. (1964). Atomic Radii in Crystals. *J. chem. phys*, 41: 3199.
- 2.27 Malgas, G.F., Adams, D., Nguyen, P., Wang, Y., Alford, T.L. & Mayer, J.W. (2001). Investigation of the effects of different annealing ambients on Ag/Al bilayers: electrical properties and morphology. *J. appl. phys.*, 90 (11): 5591-5598.
- 2.28 Sharma, S.K. & Spitz, J. (1980). Hillock formation, hole growth and agglomeration in thin silver films. *Thin solid films*, 65: 339.
- 2.29 Sharma, S.K. & Spitz, J. (1979). Hillock Growth and Agglomeration in Thin Silver Films. *Thin solid films*, 61: L13.
- 2.30 Sharma, S.K. & Spitz, J. (1980). Agglomeration in chemically deposited silver films. *Thin solid films*, 66: L51.
- 2.31 Srolovitz, D.J. & Goldiner, M.G. (1995). Thermodynamics and Kinetics of Film Agglomeration. *J. metal*, 47: 31.
- 2.32 Sinke, W., Frijink, G.P.A. & Saris, F.W. (1985). Oxygen in titanium nitride diffusion barriers. *Appl. phys. lett.*, 47: 471.
- 2.33 Ngan, K., Mosely, R., Xu, Z. & Raaijmakers, I.J. (1994). Proceedings of the Eleventh VLSI Multilevel-Interconnection Conference, IEEE, New York: 452.
- 2.34 Wolf, S. (1986). *VLSI Si processing*. Sunset Beach: Lattice Press.

CHAPTER THREE: SUMMARY AND FUTURE WORK

3.1 Summary

With the high price of scientific equipment, universities have found it difficult to purchase critical scientific equipment with which to conduct research. This thesis explores the question of using a remote instrument for a physics experiment to obtain data and evaluate whether the data obtained contradict other data not obtained remotely. It can clearly be seen that from this perspective, the experiment proved successful. The vacuum four-point probe furnace at ASU was used to obtain resistivity measurements remotely. The other forms of analysis used were XRD, RBS and SEM. The samples were annealed in vacuum both in situ and ex situ and their resistivity was measured. The types of diffusion barriers TiN, TiW and TaN all proved successful in preventing interdiffusion.

Some time was also taken to develop a website that attempted to incorporate remote instruments as well as to develop a portal for students through which they could request SEM images from the Electron Microscopy unit at the University of the Western Cape. This website was called “MicroWorld”. It no longer exist due to scarce human resources, but an attempt to include the website on the accompanying CD is made. No detailed information of MicroWorld is included in this thesis, but further information can be obtained by contacting the Physics Department at the University of the Western Cape.

Other activities also included the development of a virtual scanning electron microscope using the Virtual Reality Markup Language to teach the functions of the microscope at the Physics Department at the University of the Western Cape.

Keeping in mind that the key activity was the use of a remote instrument in the physics experiment to determine the thermal stability of diffusion barriers, the other activities mentioned, although not essential, are included for the sake of completeness.

Since the development of the virtual scanning electron microscope and details of the Virtual Reality Markup Language can be seen as a non-essential activity they are included in Appendix A. Further details of X-Ray Diffraction, Rutherford Backscattering Spectrometry and the scanning electron microscope are also included in the appendix.

3.2 Future Work

A number of activities within this thesis can be used for further study. Firstly, the fact that the key activity, namely the use of a remote instrument to prove the thermal stability of diffusion barriers, was successful, collaboration is possible between universities in the Cape to share research funds and develop a number of remote instruments to strengthen the science and technology base.

Secondly, the SEM website could be used to serve students, learners and teachers and provide SEM images to facilitate understanding. Thirdly, the present virtual scanning electron microscope can be tested in a tutorial environment and improved with feedback from students.

APPENDIX A: THE DEVELOPMENT OF A VIRTUAL SCANNING ELECTRON MICROSCOPE (VSEM) FOR TEACHING AND TRAINING

A.1 The Scanning Electron Microscope: An Overview

A schematic representation of the scanning electron microscope column is given in Figure A.1. The SEM utilises a focussed beam of high-energy electrons that systematically scans across the surface of a specimen. The electron beam is generated within an electron gun, accelerated by a high voltage and formed into a fine probe by electromagnetic lenses. The electron-optical column through which the beam passes is held under high vacuum to allow a free path for the electrons to pass through as well as to prevent high-voltage discharge. Accelerating voltages of 5 to 40 kV are routinely used in the SEM. A ray diagram of a two-lens scanning electron microscope is shown in Figure A.2 [A.1]. The first lens that influences the beam is the condenser lens, which causes the beam to converge and pass through a focal point just above a condenser aperture. The intensity of the electron beam when it strikes the specimen, and hence the brightness of the image signal, is primarily determined by the condenser lens in conjunction with the chosen accelerating voltage [A.2]. The beam diverges again below the condenser aperture and is brought into focus at the specimen through the demagnification of a final lens, the objective lens. This final lens demagnification determines the diameter of the spot size of the electron beam at the specimen, which in turn determines the specimen resolution [A.3].

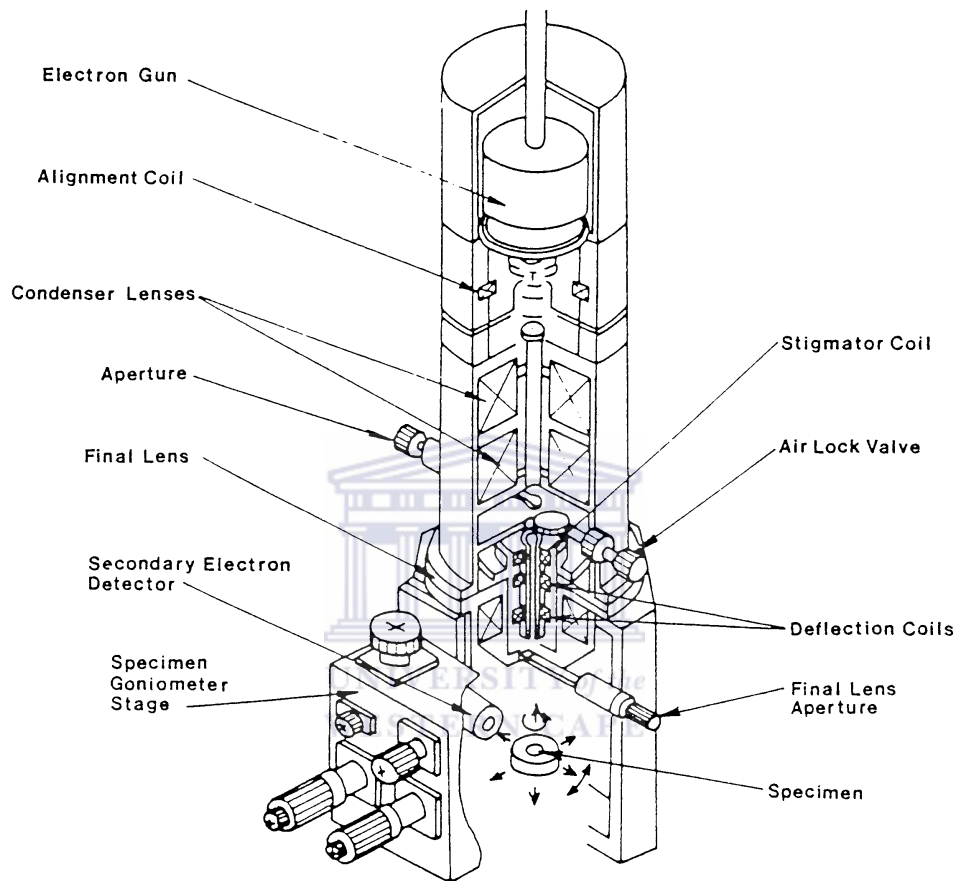


Figure A.1: Schematic representation of a scanning electron microscope column (courtesy of Hitachi Ltd) [A.4]

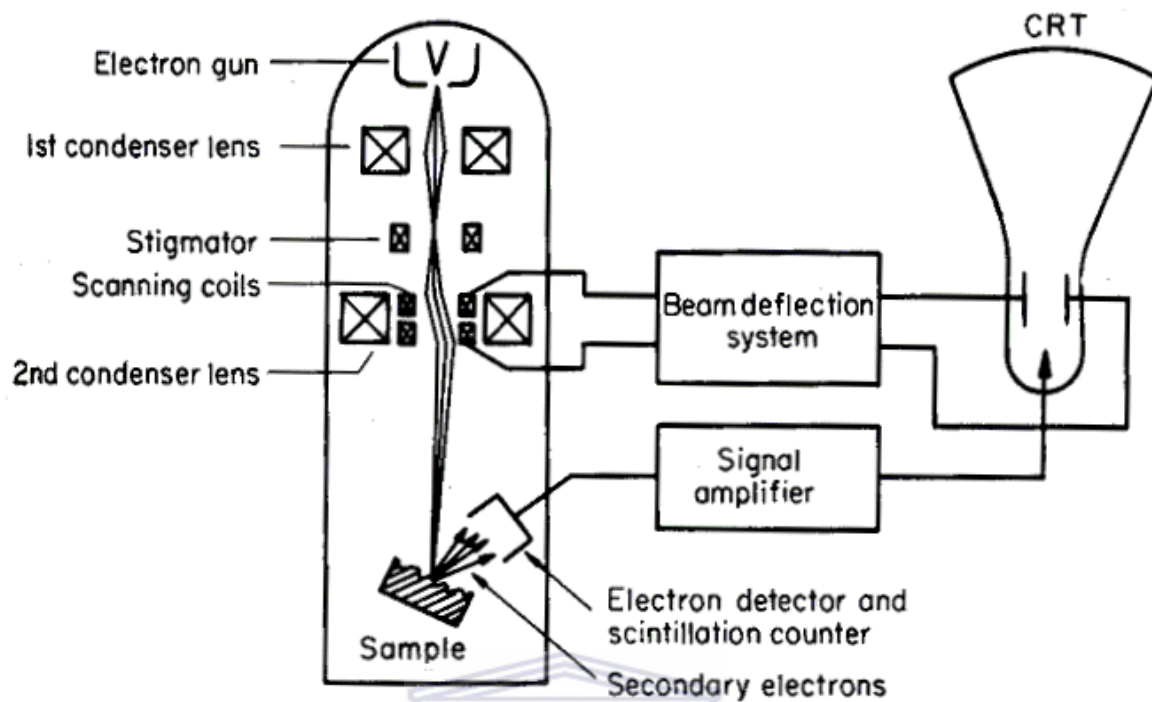


Figure A.2: Ray diagram of a two-lens SEM showing the electron beam path to the specimen [A.5]

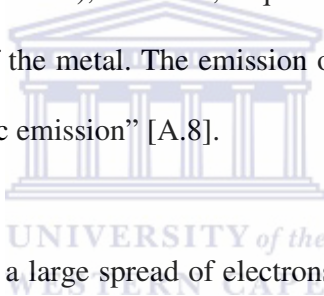
UNIVERSITY of the
WESTERN CAPE

A.1.1 The detector

X-ray energy analysis accomplished by energy dispersion, which is the separation of X-rays according to their energy, uses a semiconductor detector [A.6]. When an X-ray strikes a semiconductor crystal, the electrons in the crystal all absorb a given amount of energy (keV) and are thus excited. The greater the X-ray energy, the greater the number of electrons or the intensity. The absorbed energy is then converted to an electric signal, which is transmitted and amplified. The strength of the current from the crystal is proportional to the X-ray energy. The amplified electrical pulses from the semiconductor are converted to digital form and fed into a multichannel analyser (MCA), which sorts these signals and, in effect, counts the number of X-rays at each energy level which strikes the crystal [A.7].

A.1.2 Electron gun

The production of a high-resolution image requires a focused beam of electrons to strike the specimen. The simplest, and at present most widely used electron gun, which accounts for approximately 95% of all electron microscopy, is composed of a hairpin-shaped tungsten filament, a Wehnelt cylinder and an anode plate. The gun and the Wehnelt cylinder are connected to the negative pole of a high-voltage supply and are characteristically located at the top of the microscope column (Figure A.3). The filament is negatively charged, thus an electrical potential (a voltage difference) is established between the filament and the grounded anode plate. The difference between the cathode and the anode plate voltage is referred to as the “accelerating voltage”. A flow of electrons from the filament (cathode), however, requires the heating of the filament to overcome the work function of the metal. The emission of electrons from a filament due to heating is termed “thermionic emission” [A.8].



Thermionic emission results in a large spread of electrons outward from the filament tip. These electrons are contained and condensed into an electron cloud in space between the filament tip and Wehnelt cylinder (also termed the grid cap) by a slightly greater negative charge on the cylinder than on the filament. This charge differential is referred to as “bias”. The combined effect of the bias and the accelerating voltage toward the anode results in the creation and crude electrostatic focusing (focusing by electrical charge) of the primary electron beam in the gun [A.8]. The positioning of the filament in the grid cap is important for creating a beam of electrons focused at the specimen. The correct configuration optimises a controlled flow of electrons down the column to the specimen. When the best configuration is achieved, less heating of the filament is required and the filament life is extended [A.1].

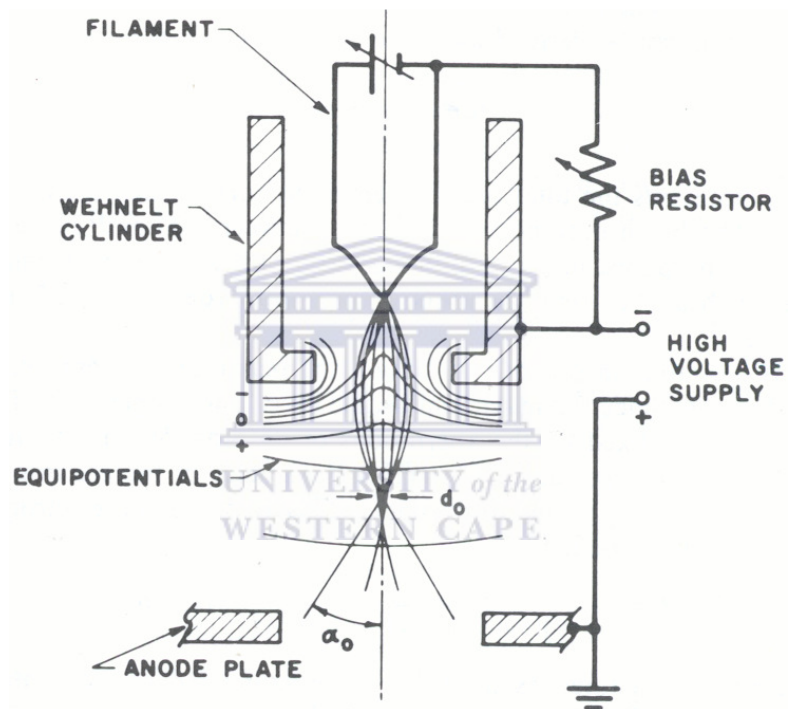


Figure A.3: The electron gun [A.9]

As current flowing through the filament increases, there is a significant increase in the number of electrons emitted up to a specific point referred to as saturation. An increase in current beyond this point only slightly increases further electron emission. At the point of most effective saturation, the highest number of electrons are generated for the least amount of current. The tungsten wire that composes the filament will wear out through evaporation and ion bombardment after a period of time. The life of a filament is dependent on several factors: maintenance of high vacuum, cleanliness of the gun and filament current. One of the major causes of the depreciation of the filament is overheating by using currents higher than saturation [A.1].

The electrons generated by the heating of a tungsten filament, as indicated above, are drawn toward the anode by an accelerating voltage. The accelerating voltage varies in most scanning electron microscopes from approximately 1 000 to 50 000 volts. Each electron accelerating from the filament to the anode acquires the energy of the accelerating voltage. Thus when an accelerating voltage of 25 000 volts is used, the electrons in the beam acquire an energy of 25 000 electron volts (eV). For the majority of the scanning electron microscopes and most specimens, 15 000 to 25 000 eV are optimal, but this may vary greatly with the specimen and the particular application [A.1].

The accelerated electrons pass through a hole in the anode, which acts as a crude aperture. The aperture allows some of the electrons to continue down the column while stopping others [A.1]. The smaller, more cohesive electron beam continuing down the microscope column tends naturally to diverge below this point. This outward spread is now influenced and converged by electromagnetic lenses [A.2].

A.1.3 Electromagnetic lenses

Electrons are charged particles, thus their paths may be influenced as they move through magnetic fields. An electromagnetic lens is essentially a length of wire coiled around a metal cylinder. As the current applied to the wire is increased, the magnetic field over the pole piece also increases in strength. The degree to which the path of an electron travelling through the pole piece is altered depends on the strength of the field, the velocity of the electrons and the relative angle between the electron path and lines of force (Figure A.4). Under the influence of such a magnetic field, electrons assume a helical path, spiralling toward the centre of the pole piece [A.2].

The first lens that influences the electron beam is the condenser lens. This lens causes the electron beam to converge and pass through a focal point. As the condenser lens current is changed, the position of the focal point in the column is altered and moves up or down the column, depending upon the current applied. A condenser lens setting which produces a focal point above a condenser aperture is generally used. Although only a small part of the beam passes through the aperture, it is far more compact, with many of the non-homogeneous and scattered electrons having been excluded. Many modern microscopes use a second condenser lens below the first, which provides more control over the electron beam [A.2].

The condenser lens, in conjunction with the chosen accelerating voltage, is primarily responsible for determining the intensity of the electron beam when it strikes a given specimen. As a result it directly affects the brightness of the image signal from that specimen [A.2]. It is important to keep in mind that a high-intensity beam may be harmful to a delicate specimen. Likewise, a high-intensity signal may damage the scintillation component of the detector system. Therefore caution should be exercised with respect to

the condenser lens setting so that the safe operating limits of the specimen and scintillator are not exceeded [A.10].

The beam will diverge again below the condenser lens aperture. A final lens is used to bring the beam into focus at the specimen by demagnifying (converging) it to a focal point at the specimen surface. The final lens demagnification determines the diameter or spot size of the electron beam at the specimen. Specimen resolution is determined by this beam diameter. Spot size reduction for optimum results is shared equally by all lenses in the column. Reduction is achieved by the appropriate combination of lens demagnification and aperture sizes [A.3].

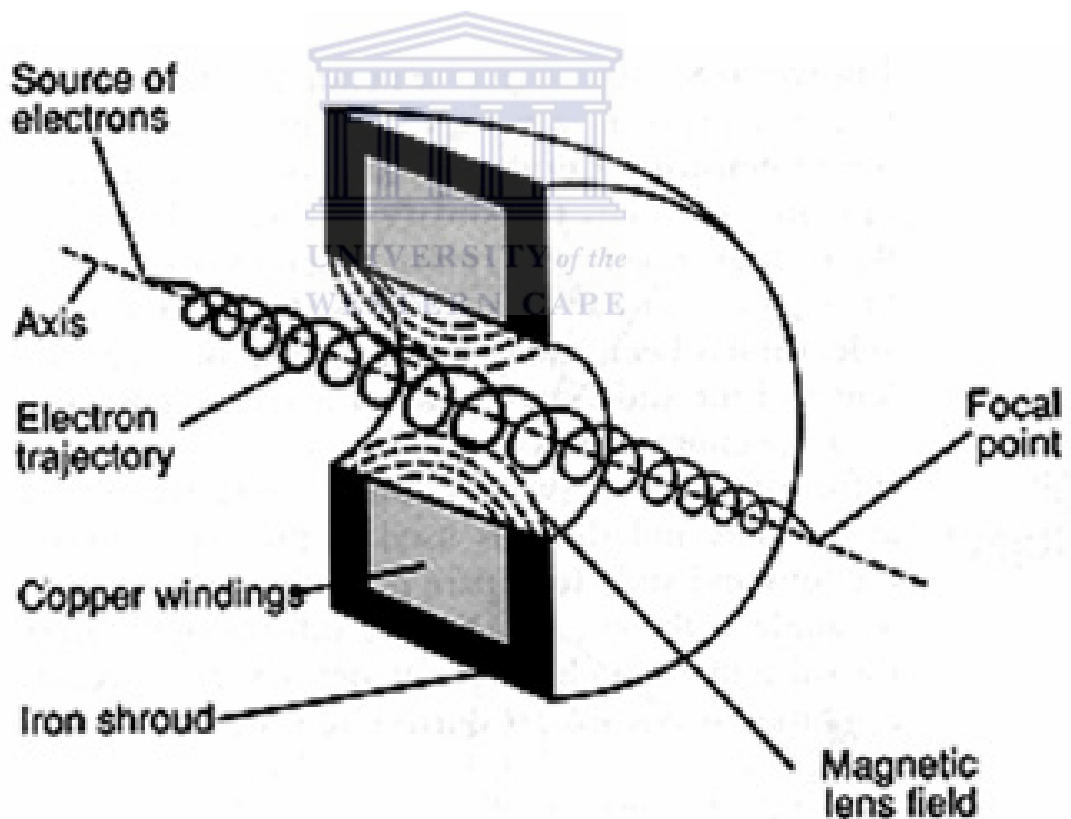


Figure A.4: The electromagnetic lens [A.11]

A.1.4 Apertures

Depending on the design of the SEM, one or more apertures may be present in the microscope column. “Spray-type” apertures may be used to reduce and exclude extraneous electrons in the lenses. In addition, an aperture may be used to reduce spherical aberrations in the final lens. This final lens aperture also affects the depth of field by determining the angle aperture. Final lens apertures vary in diameter from about 100 to 400 μm , depending on the microscope. In many scanning electron microscopes, the operator may select one of several apertures for use. Decreasing the aperture size will result in an increase in depth of field, but with a loss in relative brightness [A.3].



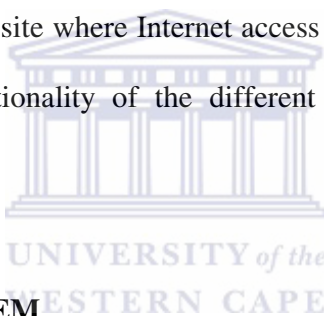
A.1.5 The specimen stage

The specimen stage is the platform upon which the specimen rests in the column of the scanning electron microscope. The stage is located directly underneath the final lens and represents a significant portion of the specimen chamber. The design of the specimen chamber differs significantly from microscope to microscope. The distance between the specimen stage and the final lens (objective lens) is called the working distance of the microscope [A.12].

A.2 The Virtual Scanning Electron Microscope

A.2.1 Rationale

The Virtual Scanning Electron Microscope (VSEM) was designed with remote self-paced training in mind. The advantage of self-paced learning is that the student is able to review the learning material numerous times in order to facilitate understanding. It is anticipated that this tool will decrease the time for training on the actual scanning electron microscope, making it available to other users, lowering the risk of damage to the system and minimising maintenance costs of the microscope. The interactivity of the scanning electron microscope facilitates understanding by giving the student the opportunity to visualise each part of the microscope in a three-dimensional way. The VSEM can also be used at any time and from any site where Internet access is available. The trainee will be able to learn about the functionality of the different components of a SEM in an interactive manner.



A.2.2 The design of the VSEM

Many ways of creating such a tool were investigated and VRML (Virtual Reality Modelling Language) was decided on because of its universality. The fact that a virtual microscope could be viewed anywhere with an Internet connection and browser played a major role in its selection. A virtual microscope consisting only of the major components of an actual system was developed, that is, an electron gun, condenser lens, objective lens, apertures, a sample stage and a detector. The VSEM has the capability of demonstrating the basic operation of a scanning electron microscope, with the emphasis on the functionality of the major components.

It demonstrates 1) the emission of electrons from the electron gun, 2) the deflection of the electrons through the lenses and coils, and 3) action of the detector system. Figure A.5

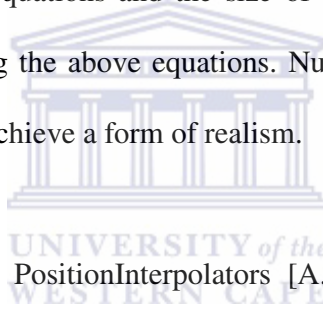
shows the electron gun, which consists of an anode, a Wehnelt cylinder and the biasing wires. The flow of electrons through the microscope was achieved with the use of the PositionInterpolator of VRML. The electrons follow a helical path due to the action of the electromagnetic lenses, so the electron's motion can therefore be described by the following equations, which are the equations for a helix in three dimensional space:

$$x = \cos A$$

$$y = \sin A$$

$$z = A$$

where x , y and z denote the position in three-dimensional space and A denotes both the size of angle in the x and y equations and the size of z in the electron's motion. The positions were calculated using the above equations. Numerous points along the helical path were inserted in order to achieve a form of realism.



ColorInterpolators [A.13] and PositionInterpolators [A.14] were used to demonstrate thermionic emission from the filament in the electron gun. The ColorInterpolators were also used to simulate the heating up of the filament just before the emission of electrons. The PositionInterpolators were used to show the movement of electrons from the filament. Synchronisation of the change of colour of the filament with the movement of the electrons was crucial in achieving realism of this phenomenon.

The condenser and the objective lenses are shown in Figures A.6 and A.7 respectively. The detector system is shown in Figure A.8. It shows the scintillator, photodetector and the wires that send the signal to the microscope's monitor. The VSEM was designed according to the modular design approach, namely that it could be split into its components and hence facilitate easy instruction. The user has the option of viewing the

entire system or its individual components. PositionInterpolators and OrientationInterpolators [A.15] were used to perform the animations where the components of the microscope split into its more elementary parts.

A.3 How to Use the Virtual Scanning Electron Microscope

The virtual scanning electron microscope can be accessed through the accompanying CD. The VSEM was originally on a webserver, but due to scarce human and financial resources, it is only available on the CD. The user needs Netscape or Internet Explorer with a VRML plug-in [A.16]. The plug-ins are available for download over the Internet from Cortona3D [A.17] or Cosmo software [A.18].

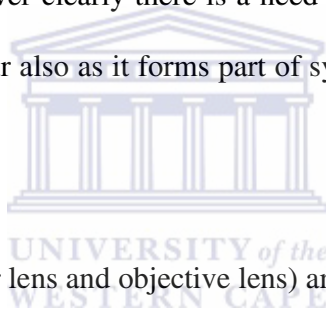
The website is forms part of the larger VIMS website, elaborated on earlier. The virtual scanning electron microscope (Figure A.9), now however consists of a list of 3D representations and animations. They are in no particular order:

- 1) The detector, which collects the electrons
- 2) Different components of the microscope
- 3) The electron gun
- 4) Accelerating voltage (needs improvement)
- 5) Bias (needs improvement)
- 6) Thermionic emission
- 7) Structure of lenses (needs improvement)
- 8) The helical path of the electrons
- 9) The second condenser lens
- 10) The picture on the monitor of the specimen scanning progressively.

The detector (Figure A.8) animation has the following features, when clicking on the detector it opens up, and the inner parts are visible, also when clicking on the grey ball, a ball representing an electron moves towards the detector.

The different parts of the microscope are visible also in the file called “microscopeguts0907.wrl” (Figure A.10).

The electron gun has an animation that shows thermionic emission, that is the electrons coming from the filament, with the filament changing colour in the process. The animation is activated when clicking on the filament. The accelerating voltage and bias is shown in the 3D model, however clearly there is a need for improvement as the one red top wire needs to change colour also as it forms part of system that is positively charged (Figure A.5).



The different lenses (condenser lens and objective lens) are also shown in 3D models, and they disassemble upon clicking on them (Figure A.6, Figure A.7).

An animation showing the sample appearing progressively on is also added

Admittedly, these animations are not perfect and this microscope should be seen as a beta version that can be trialed in class and improved upon.

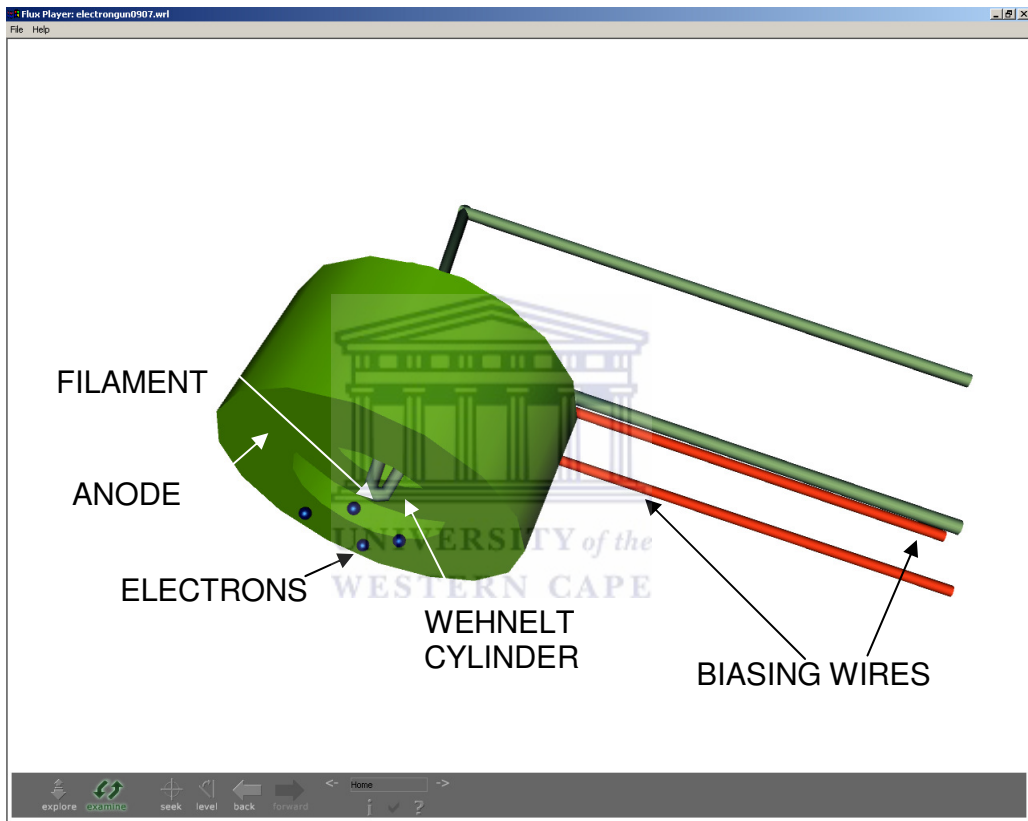


Figure A.5: The electron gun

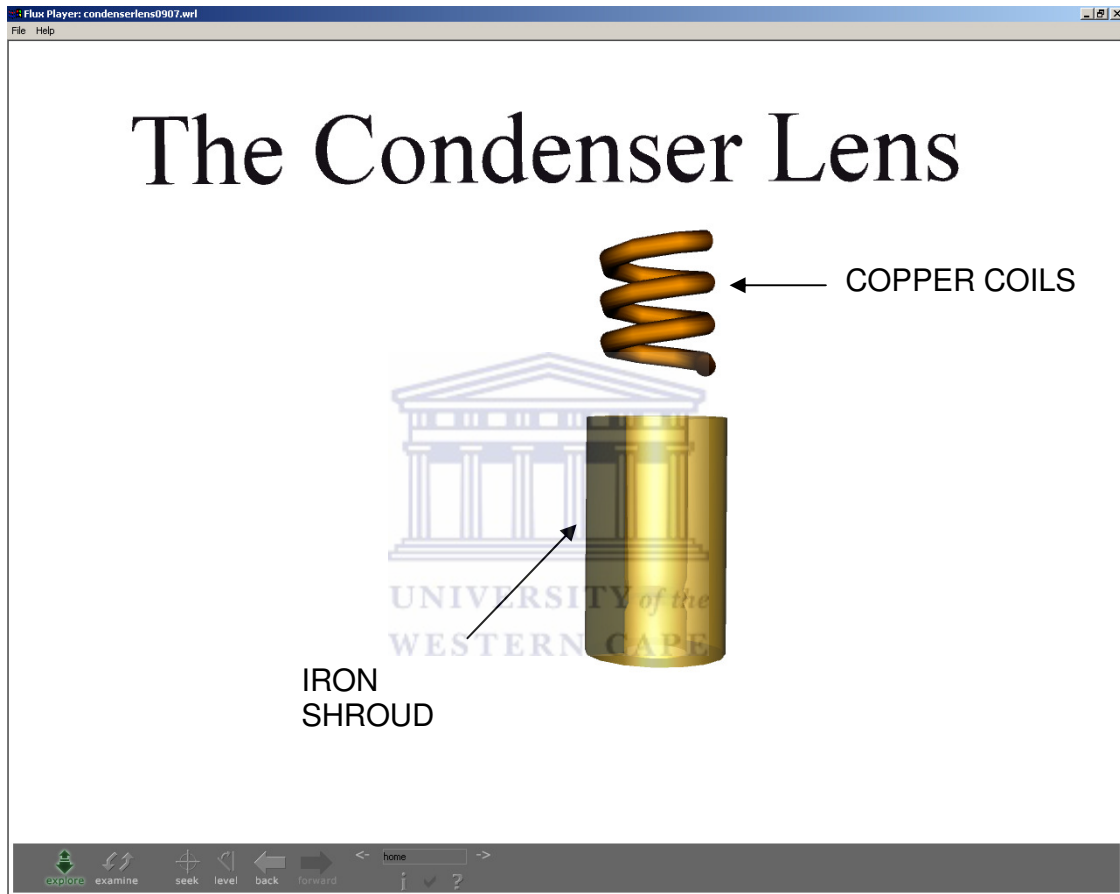


Figure A.6: The condenser lens

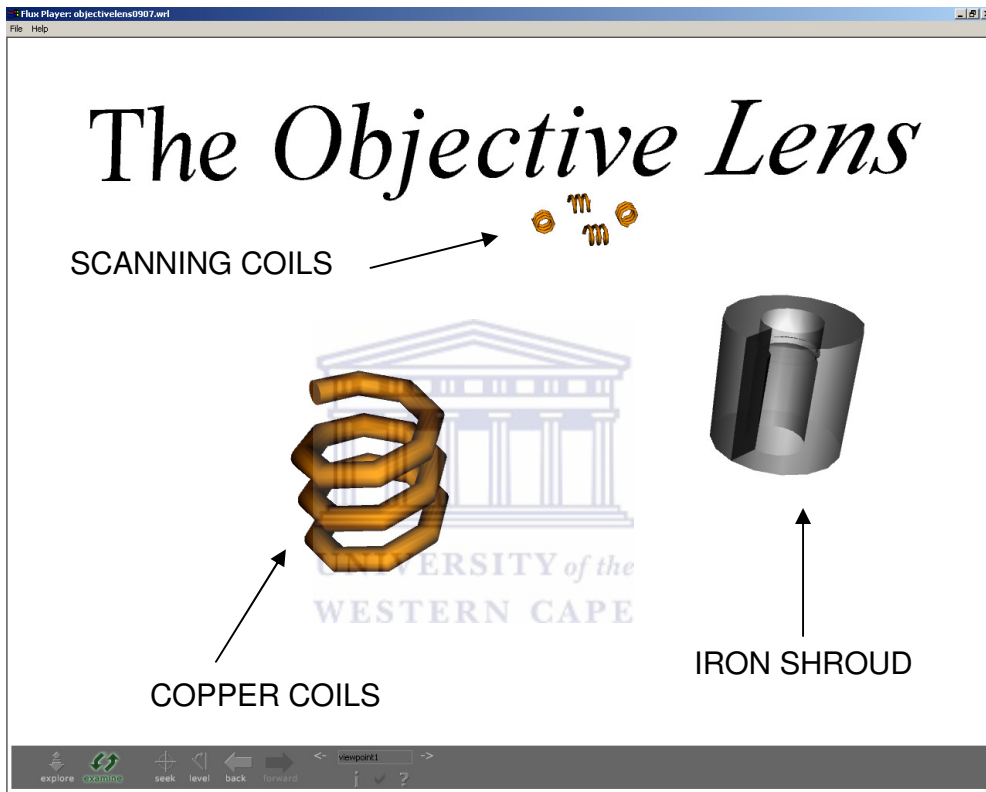


Figure A.7: The objective lens

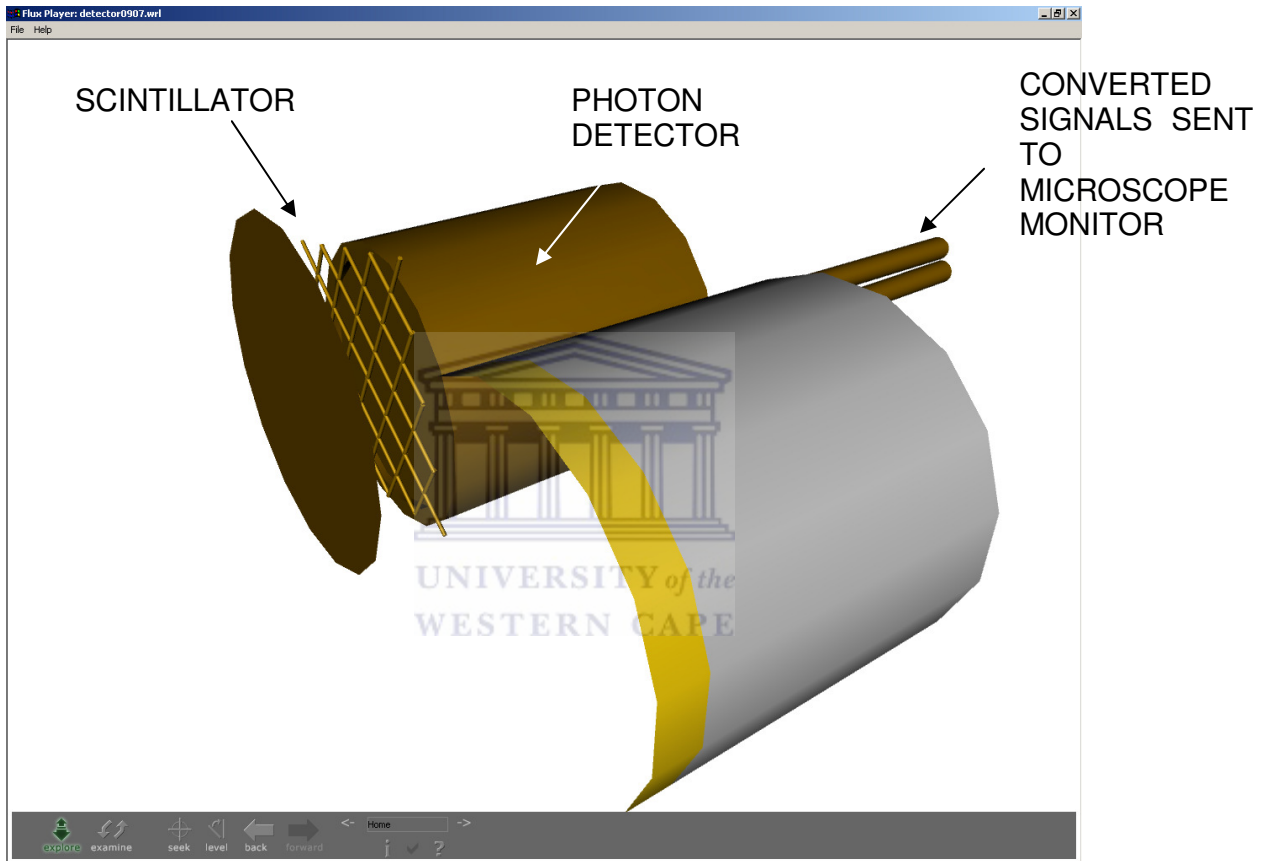


Figure A.8: The detector

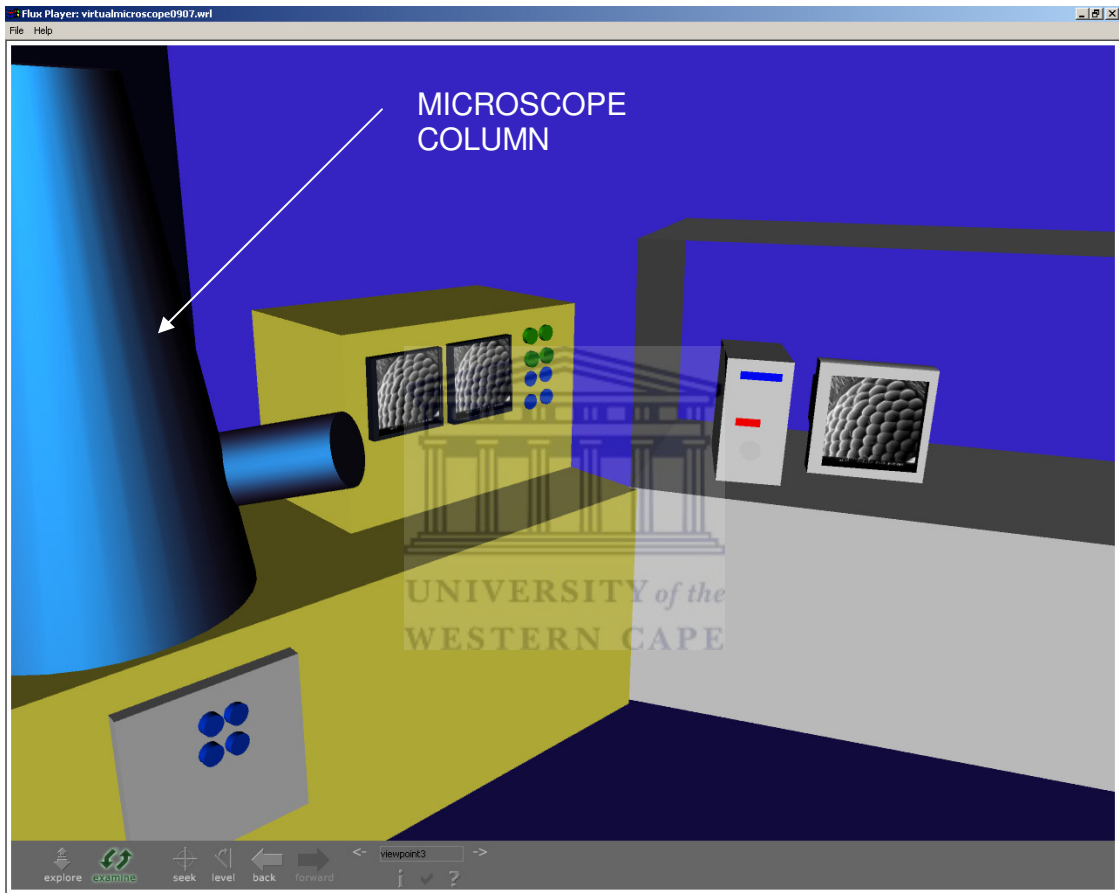


Figure A.9: The microscope created with CosmoWorlds

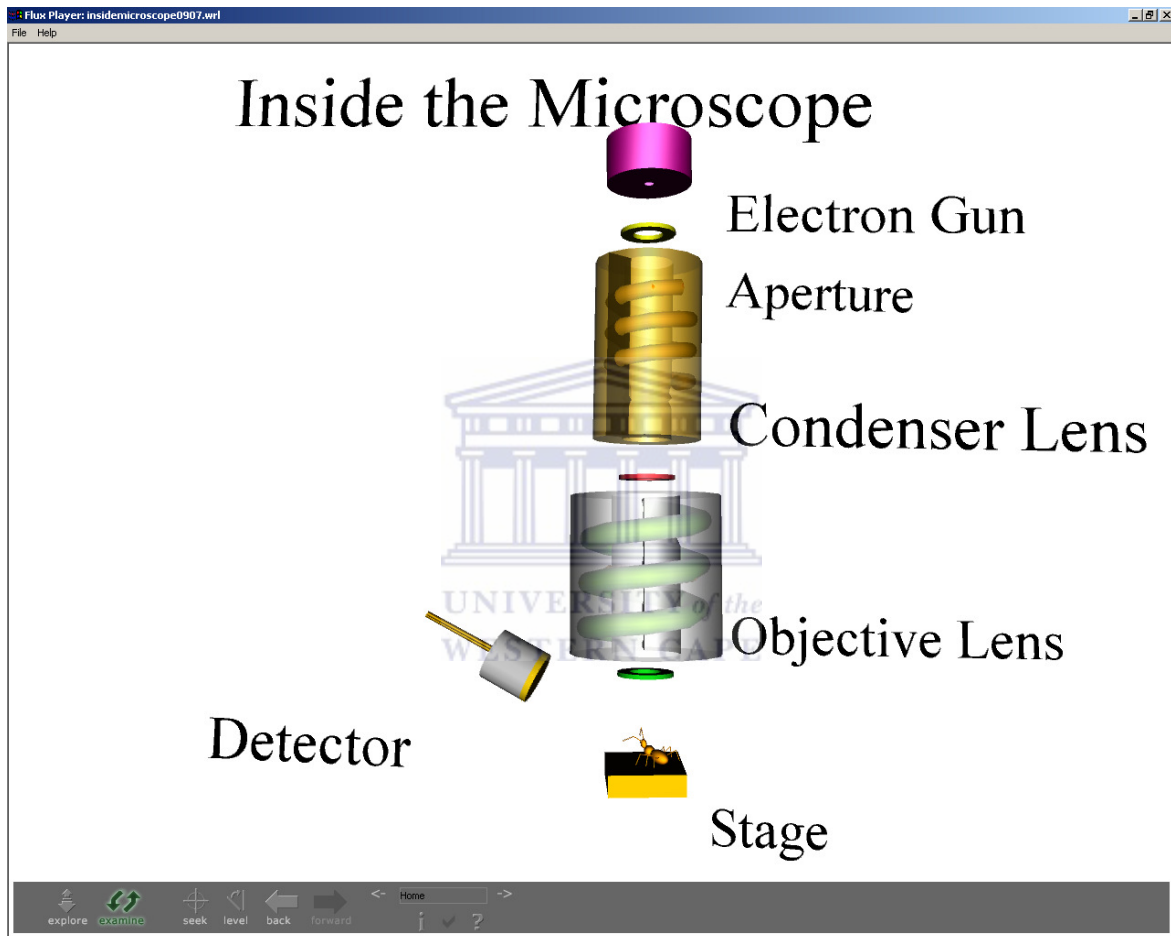


Figure A.10: The major components created with CosmoWorlds

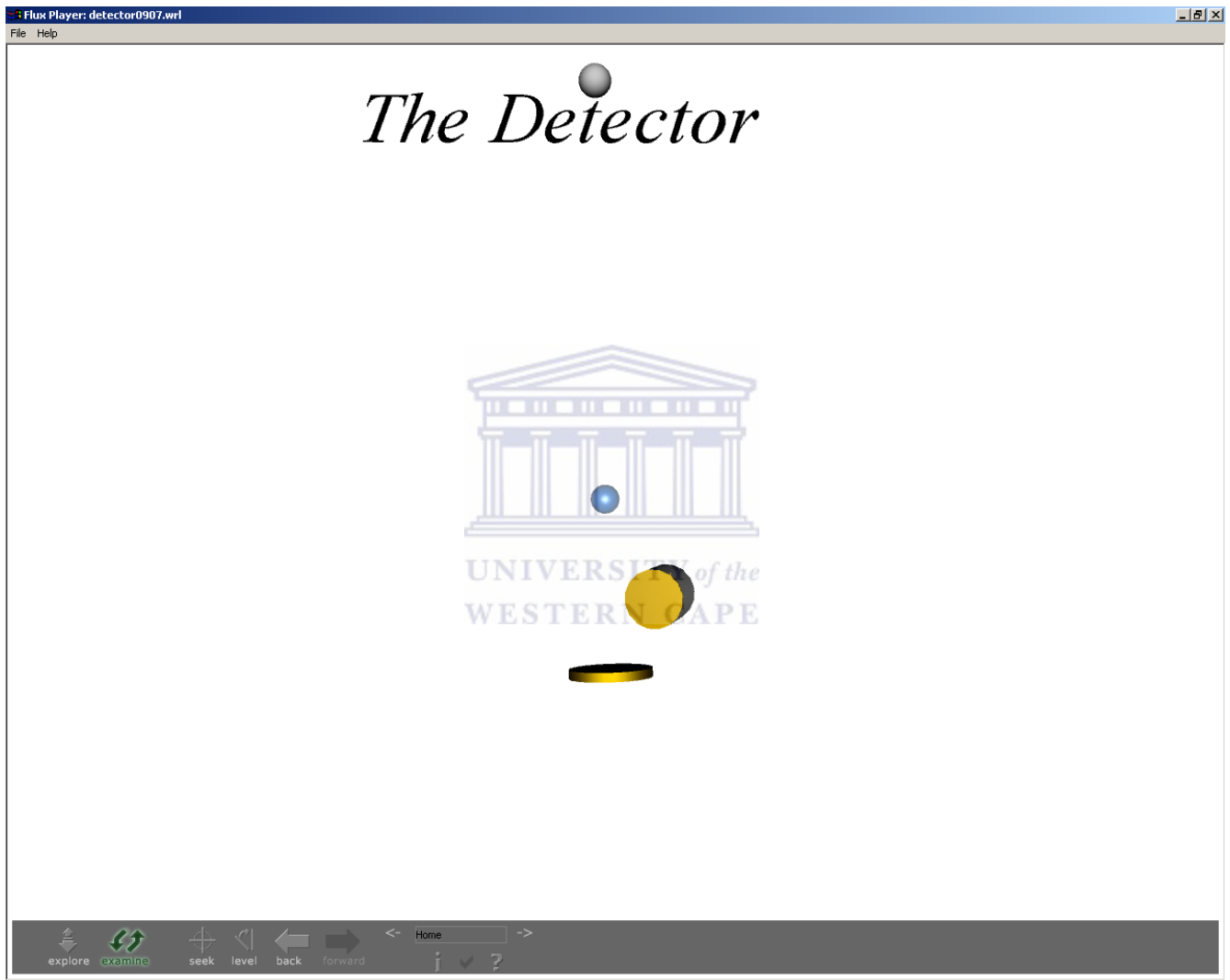
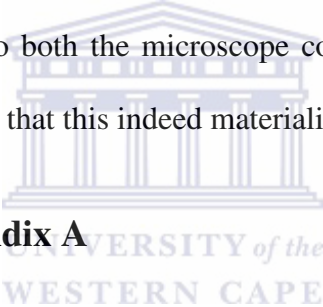


Figure A.11: The detector of the microscope animation created with CosmoWorlds

A.4 Conclusion

This chapter shows how the Virtual Reality Modelling Language (VRML) can be applied to the illustration of physics principles. The design and implementation of VSEM using VRML makes it accessible worldwide since it is on a platform-independent language that makes it viewable in any web browser. Future research could involve development of the VSEM, by introducing more physics principles and testing its effectiveness as an instructional tool. The VSEM is no longer available on the website (<http://sem.uwc.ac.za/>) as the server is no longer in operation, however the microscope is available on the accompanying CD. The VSEM is also by no means complete but rather illustrates the potential of using this medium. A lot of improvements can be made to both the microscope components and its animations, and it is the hope of the author that this indeed materialises.

A.5 References – Appendix A

- 
- A.1 Postek, Jr. M. (1980). *Scanning electron microscopy: a student's handbook*. Burlington, VT.: Ladd Research Industries, Inc.: 15.
- A.2 Postek, Jr. M. (1980). *Scanning electron microscopy: a student's handbook*. Burlington, VT.: Ladd Research Industries, Inc.: 16.
- A.3 Postek, Jr. M. (1980). *Scanning electron microscopy: a student's handbook*. Burlington, VT.: Ladd Research Industries, Inc.: 17.
- A.4 Postek, Jr. M. (1980). *Scanning electron microscopy: a student's handbook*. Burlington, VT.: Ladd Research Industries, Inc.: 14.
- A.5 Von Heimendal, M. (1980). *Electron microscopy of materials: an introduction*. New York: Academic Press: 35.

- A.6 Postek, Jr. M. (1980). *Scanning electron microscopy: a student's handbook*. Burlington, VT.: Ladd Research Industries, Inc.: 79.
- A.7 Postek, Jr. M. (1980). *Scanning electron microscopy: a student's handbook*. Burlington, VT.: Ladd Research Industries, Inc.: 81.
- A.8 Postek, Jr. M. (1980). *Scanning electron microscopy: a student's handbook*. Burlington, VT.: Ladd Research Industries, Inc.: 13.
- A.9 Goldstein, J.I., Newbury, D.E., Echlin, P., Joy, D.C., Fiori, C. & Lifshin, E. (1981). *Scanning electron microscopy and X-ray microanalysis: a text for biologists, material scientists, and geologists*. New York: Plenum Press: 21.
- A.10 Postek, Jr. M. (1980). *Scanning electron microscopy: a student's handbook*. Burlington, VT.: Ladd Research Industries, Inc.: 12.
- A.11 *The Transmission Electron Microscope at the University of Delaware*. [Online]. Available <http://www.udel.edu/Biology/Wags/b617/tem/tem6.gif>
- A.12 Postek, Jr. M. (1980). *Scanning electron microscopy: a student's handbook*. Burlington, VT.: Ladd Research Industries, Inc.: 19.
- A.13 Hartman, J. & Wernecke, J. (1996). *The VRML 2.0 handbook: building moving worlds on the Web*. New Jersey: Addison Wesley Developers Press: 281.
- A.14 Hartman, J. & Wernecke, J. (1996). *The VRML 2.0 handbook: building moving worlds on the Web*. New Jersey: Addison Wesley Developers Press: 331.
- A.15 Hartman, J. & Wernecke, J. (1996). *The VRML 2.0 handbook: building moving worlds on the Web*. New Jersey: Addison Wesley Developers Press: 323.
- A.16 The Netscape Website. [Online]. Available <http://www.netscape.com/>
- A.17 The Parallel Graphics Website. [Online]. Available <http://www.parallelgraphics.com/>

A.18 The Cosmo Player Website. [Online]. Available

<http://www.karmanaut.com/cosmo/player/>



APPENDIX B: EXPERIMENTAL TECHNIQUES

B.1 Rutherford Backscattering Spectrometry (RBS)

Rutherford Backscattering Spectrometry (RBS) is perhaps the easiest analytical technique to understand and apply in the study of thin films. Apart from the accelerator which provides a collimated beam of particles with energy of several MeV (usually $^4\text{He}^{2+}$ ions), the instrumentation is simple. The sample is bombarded by a homogeneous non-interacting mono-energetic particle beam of 2 - 4 MeV. Some of the particles are transmitted or absorbed by the sample while others are backscattered. A solid state detector detects the backscattered particles as shown in Figure B.1.

The analytical capabilities of Rutherford Backscattering Spectrometry depend on three concepts (in no particular order):

Differential cross-section $\frac{d\sigma}{d\Omega}$ (quantitative analysis)

Energy loss $\frac{dE}{dx}$ (depth analysis)

Kinematic factor K (mass analysis) [B.1, B.2]

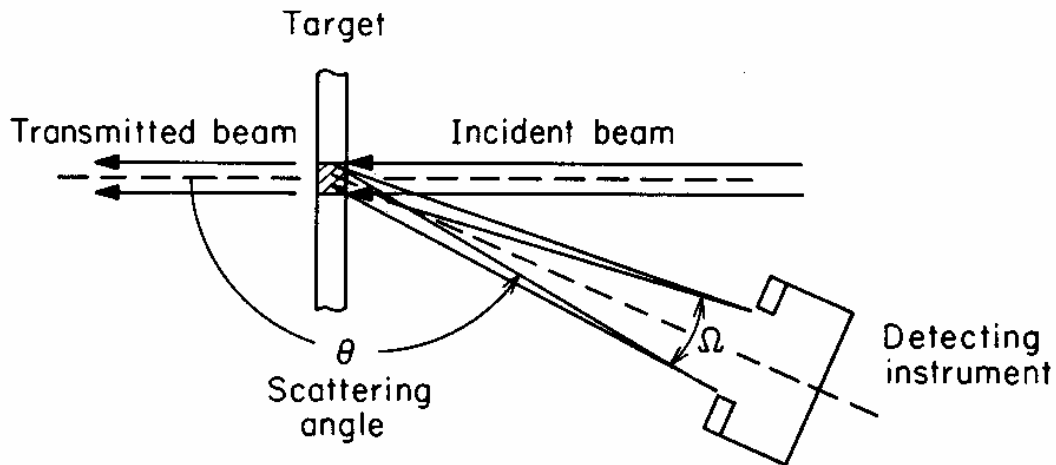


Figure B.1: Diagram of the experimental set-up of Rutherford backscattering. A 2 MeV ${}^4\text{He}^{2+}$ beam was used [B.3].

B.1.1 Kinematic factor

During RBS, monoenergetic particles in the incident beam collide with target atoms and are scattered backwards into the detector. The collision is assumed to be elastic. During the collision, energy is transferred from the moving particle to the stationary target atom [B.2].

Applying the principles of conservation of energy and momentum in a laboratory frame of reference, the energy transfers in elastic collision between two particles can be solved. [B.4].

The notation for the laboratory system of co-ordinates is illustrated in Figure B.2. The conservation of energy and momentum parallel and perpendicular to the direction of incidence are expressed by the following equations:

Momentum before collision = Momentum after collision, and

Energy before collision = Energy after collision

$$\frac{1}{2}M_1V_0^2 = \frac{1}{2}M_1V_1^2 + \frac{1}{2}M_2V_2^2 \dots\dots\dots(a)$$

$$M_1V_0 = M_1V_1 \cos \theta + M_2V_2 \cos \phi \dots\dots\dots(b)$$

$$0 = M_1V_1 \sin \theta - M_2V_2 \sin \phi \dots\dots\dots(c)$$

Eliminating ϕ and V_2 we obtain the ratio [B.4]

$$\frac{V_1}{V_0} = \frac{(M_2^2 - M_1^2 \sin^2 \theta)^{1/2} + M_1 \cos \theta}{M_1 + M_2} \dots\dots\dots(d)$$

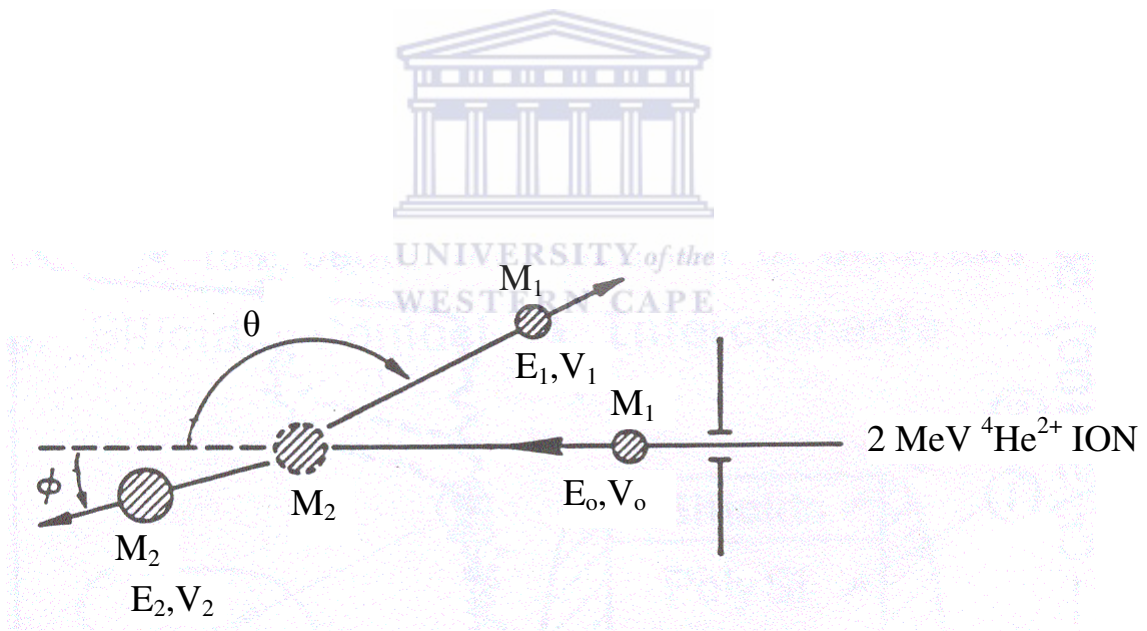


Figure B.2: Diagram showing elastic collision between a projectile of mass M_1 with velocity V_0 and a stationary target of mass M_2 [B.5]

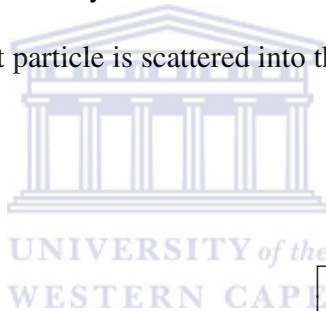
The kinematic factor is defined as the ratio between the projectile energies after and before the elastic collision.

$$K = \frac{E_1}{E_0} = \frac{V_1^2}{V_0^2} \dots\dots\dots (e)$$

From equation (a) we see that the kinematic factor (K) depends on the scattering angle in the laboratory frame and the masses involved in the collision [B.4].

B.1.2 Differential cross-section

Differential cross-section, governed by coulombic scattering, is the probability per unit solid angle at which an incident particle is scattered into the solid angle $d\Omega$ subtended by the detector (Figure B.1) [B.6].



$$\frac{d\sigma(\theta)}{d\Omega} = \left(\frac{Z_1 Z_2 e^2}{4E_0} \right)^2 \frac{4}{\sin^4 \theta} \frac{\left[\cos + \left(1 - \frac{M_1^2}{M_2^2} \sin^2 \theta \right)^{\frac{1}{2}} \right]^2}{\left[1 - \left(\frac{M_1}{M_2} \sin \theta \right)^2 \right]^{\frac{1}{2}}} \dots\dots (f)$$

where

$Z_1 e$ = charge of the projectile

$Z_2 e$ = charge of the target

E_0 = energy of the projectile before scattering

Ω = finite solid angle spanned by the detector

B.1.3 Energy loss

When an incident particle penetrates to some depth in a dense medium, projectile energy dissipates due to interactions with electrons and to glancing collisions with the nuclei of target atoms. The amount of energy a projectile loses depends on the thickness, its velocity, the elements in the sample and the density of the sample material. The energy loss is expressed as a stopping power, $\frac{dE}{dx}$. The ratio of energy loss to two-dimensional

atom density (N) for a given material is known as its stopping cross-section given as $\epsilon = \frac{1}{N} \frac{dE}{dx}$ [B.7]. Both stopping power and cross-section depend on the composition of the

target. In general, for small energy losses, $\frac{dE}{dx}$ does not change much and there exists a

relationship between energy loss (ΔE) and depth (t) that can be expressed as $\Delta E = [S] t$, where [S] is the backscattering energy loss factor. For thin films, the surface approximation can be used to evaluate the energy loss $\left(\frac{dE}{dx}\right)_{in}$ at E_0 for its incoming path

and $\left(\frac{dE}{dx}\right)_{out}$ at KE_0 for its outgoing path, where K is the backscattering kinematic factor.

Thus, the energy lost by a projectile of mass m, which was backscattered by an atom of mass M at a depth t, can be approximated as [B.8]:

$$\Delta E = [S] t = \left[\frac{K}{\cos\theta_1} \frac{dE}{dx} \Big|_{E_0} + \frac{1}{\cos\theta_2} \frac{dE}{dx} \Big|_{KE_0} \right] t \dots\dots\dots(g)$$

where θ_1 and θ_2 are the angles of the incoming and outgoing particle with respect to the normal and $\theta = 180 - \theta_1 - \theta_2$ [B.9]. In a compound target, the energy loss of the material

is, however, affected by both the elements in the sample. The energy loss for a particle backscattered from element A at a depth t in a compound A_mB_n is given by [B.1]:

$$\Delta E_A = [S]_A t = \left[\frac{K_A}{\cos \theta_1} \frac{dE}{dx} \Big|_{E_0} + \frac{1}{\cos \theta_2} \frac{dE}{dx} \Big|_{K_A E_0} \right] t \dots\dots\dots (h)$$

where K_A is the backscattering kinematic factor of element A (page 61,62). Bragg's rule states that $\epsilon^{A_mB_n} = m\epsilon^A + n\epsilon^B$ where ϵ^A and ϵ^B are the stopping cross-sections of atoms A and B respectively [B.10]. The total energy loss in the compound A_mB_n is therefore:

$$\Delta E = [S]^{A_mB_n} t = [S]_A^{A_mB_n} N^{AB} t + [S]_B^{A_mB_n} N^{AB} t \dots\dots\dots (i)$$

Where N^{AB} is the number of molecules A_mB_n per unit volume [B.11]. The height of the spectrum H gives the number of backscattered particles with energy in a certain energy interval δE between E and $(E+\delta E)$, and is given by

$$H = n_0 \Omega \left(\frac{d\sigma}{d\Omega} \right) N \frac{E}{[S] \cos \theta_1} \dots\dots\dots (j)$$

where n_0 is the number of incident particles Ω , the solid angle of the detecting system and N the atomic density, while $\left(\frac{d\sigma}{d\Omega} \right)$ and $[S]$ are given by equation (f) and equation (g) respectively [B.12]. The height of the spectrum peak H_A for element A in the compound A_mB_n can be given in the same way as equation (j):

$$H_A = n_0 \Omega \left(\frac{d\sigma}{d\Omega} \right)_A N_A \frac{\delta E}{[S]_A^{A_mB_n} \cos \theta_1} \dots\dots\dots (k)$$

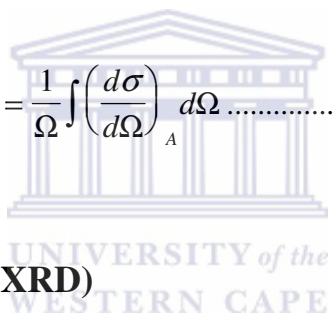
where N_A refers to the density of the atoms A in the compound. A similar equation holds for H_B , the height of the spectrum peak for element B [B.13].

It is obvious that N_A and N_B are proportional to m and n, thus [B.14]:

$$\frac{H_A}{H_B} = \frac{\sigma_A m [S]_B^{A_m B_n}}{\sigma_B n [S]_A^{A_m B_n}} \dots\dots\dots(1)$$

where σ_A is the average differential cross-section given by [B.3].

$$\sigma_A = \frac{1}{\Omega} \int \left(\frac{d\sigma}{d\Omega} \right)_A d\Omega \dots\dots\dots(m)$$



B.2 X-Ray Diffraction (XRD)

X-ray diffraction had its beginnings in 1912 with Von Laue’s discovery that crystals diffract X-rays, the manner of which reveals the structure of the crystal. X-rays are photons with wavelengths comparable to the interatomic distances in crystals. This technique plays an important role in solving molecular structures, identifying compounds, and the fabrication of materials [B.15].

B.2.1 How X-rays are formed

Characteristics spectra are produced when the bombarding electrons have sufficient energy to penetrate to the interior of the atoms of the target and to dislodge electrons from their innermost shells. An atom may be pictured as a nucleus surrounded by shells of

electrons. The inner or K shell can have two electrons, the L shell eight electrons, the M shell eighteen, and so on. The K shell electrons are the most difficult to dislodge. Another electron replaces the expelled one, and the probability is that the vacancy will be filled from the next outer shell rather than from a more remote shell. This creates a new vacancy, which is filled from the next shell, or less probably from a more distant shell, and thus the atom returns to a normal state in a series of steps. An electron moves to a lower energy level when it falls into an inner shell. The transition is accompanied by the emission of energy in the form of x-radiation, the wavelength of which is precisely fixed by the difference in energy between the shells. Falling from the various levels to replace K electrons generates the K series of peaks. Falling in of L electrons gives rise to the K peaks. L electrons are distributed over three sublevels L_i with two electrons, and L_{iii} with four electrons. Transition does not occur from the L_i sublevel. The L_i and L_{iii} sublevels represent slightly different energy levels, and as a result the K peak is actually a doublet whose individual peaks are designated respectively as α_2 and α_1 . Similarly, the K peak is a closely spaced doublet, which arises from the transfer of electrons from two of five M sublevels. A third doublet, the α peak, is formed by electrons falling in from two of the five N sublevels. The total of such transfers gives rise to the K characteristic spectrum (see Figure B.3) [B.16, B.17].

The reason for using X-rays as the medium to determine the different types of elements is that the wavelength of X-rays is comparable to the interatomic distances of the crystals [B.15].

B.2.2 Bragg diffraction

An electron in the path of an unpolarised X-ray beam vibrates with the frequency of the incident radiation, periodically absorbing energy and emitting it as x-radiation of the same

frequency. The original X-rays are unmodified in wavelength by the interaction but are radiated in all directions [B.18].

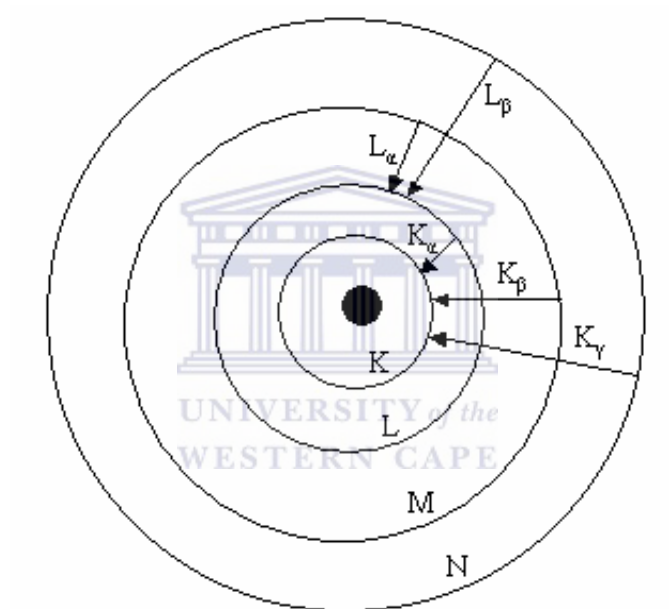


Figure B.3: Schematic drawing to illustrate the production of K and L characteristic peaks that appear in XRD spectra [B.17].

The electron has the effect of scattering the incident radiation and acts as a source of secondary X-rays. The nucleus, because of its high mass, makes a negligible contribution to the radiation scattered by an atom. All atoms in the path of an X-ray beam scatter X-rays simultaneously. In general, the scattered waves interfere with and destroy one another, but in certain specific directions they combine to form new wave fronts. This cooperative scattering is known as diffraction. The directions of possible diffraction depend only on the size and shape of the unit cell [B.18].

Each atom of a row in the path of an X-ray beam can be considered as the centre of radiating, spherical wave shells [B.19]. In general, the scattered waves interfere with each other, but combine to form new wave fronts when they are in phase - that is, when the difference in path length between the rays scattered from adjacent atoms is zero or any whole number of wavelengths. Wave fronts are designated in accordance with the path difference of rays scattered by neighbouring atoms. The path difference for a first-order wave front is one wavelength, and the diffracted beam is described as a first order of diffraction. This can be summarised in the following Von Laue equations, which illustrate the conditions for diffraction [B.20].

$$p(\cos \bar{\nu} - \cos \bar{\mu}) = \pm h\lambda$$

for zero order diffraction (Figure B.4):

$$p(\cos \bar{\nu} - \cos \bar{\mu}) = 0\lambda$$

which reduces to:

$$p \cos \bar{\nu} = p \cos \bar{\mu} \quad [\text{B.20}]$$

For three dimensions (Figure B.5) the Von Laue equations transform into:

$$a(\cos \bar{\nu}_1 - \cos \bar{\mu}_1) = \pm h\lambda$$

$$b(\cos \bar{\nu}_2 - \cos \bar{\mu}_2) = \pm k\lambda$$

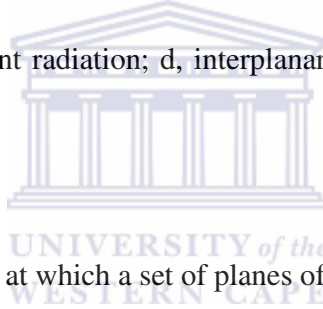
$$c(\cos \bar{\nu}_3 - \cos \bar{\mu}_3) = \pm l\lambda \quad [\text{B.21}]$$

A crystal will only diffract X-rays if the above three equations are met, wherein ν_1 , ν_2 and ν_3 define a common direction and a , b , and c are constant for a particular crystal [B.21, B.22].

There is a much simpler mathematical expression of diffraction, called Bragg's Law (Figure B.6), which is written as:

$$n\lambda = d \sin \theta$$

where λ , wavelength of incident radiation; d , interplanar spacing; n , integer constant; θ , Bragg angle.



The equation gives the angle θ , at which a set of planes of spacing d cooperatively reflects α radiation of wavelength λ in the n^{th} order [B.23].

B.2.3 Intensity of diffraction

The radiation obtained from a diffraction tube is generally considered as unpolarised [B.24]. The process of scattering causes the diffracted beam to become partially polarized, and the degree of polarisation is dependent on the angle of scattering. Hence the intensity of scattering by an electron varies with the angle.

Consider an electron scattering the incident beam along a diffraction direction, which makes an angle 2θ with the undeviated beam [B.25]. This results in an intensity of scattering at a distance R from the electron, in that direction of

$$I_e = I_o \left(\frac{e^4}{m^2 c^4 R^2} \right) \left(\frac{1 + \cos^2 2\theta}{2} \right)$$

Where I_o is the intensity of the incident beam, e and m are the charge and mass of the electron respectively, and c is the speed of light. The quantity $\frac{(1 + \cos^2 2\theta)}{2}$ is called the polarisation factor [B.25, B.27].



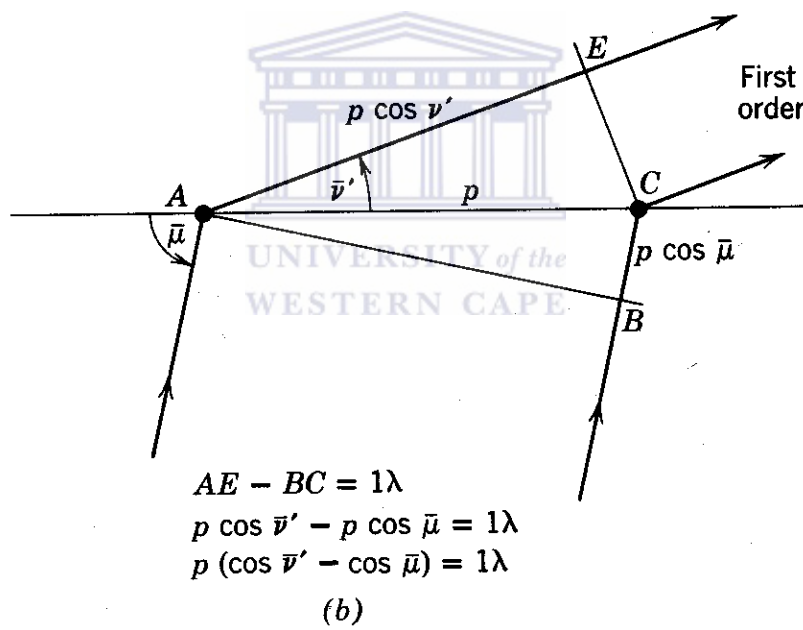
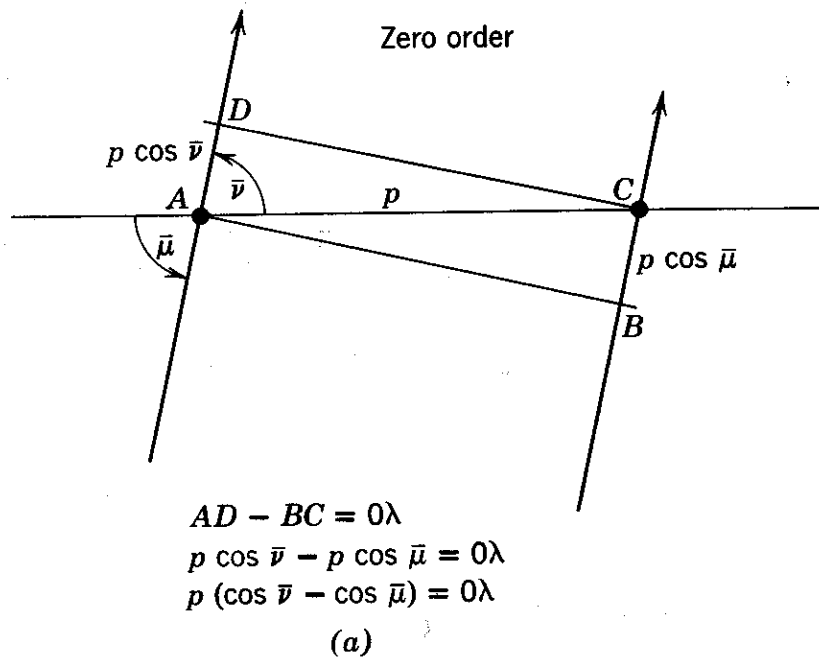


Figure B.4: The condition for the first and zeroth order diffraction from a row of atoms [B.19].

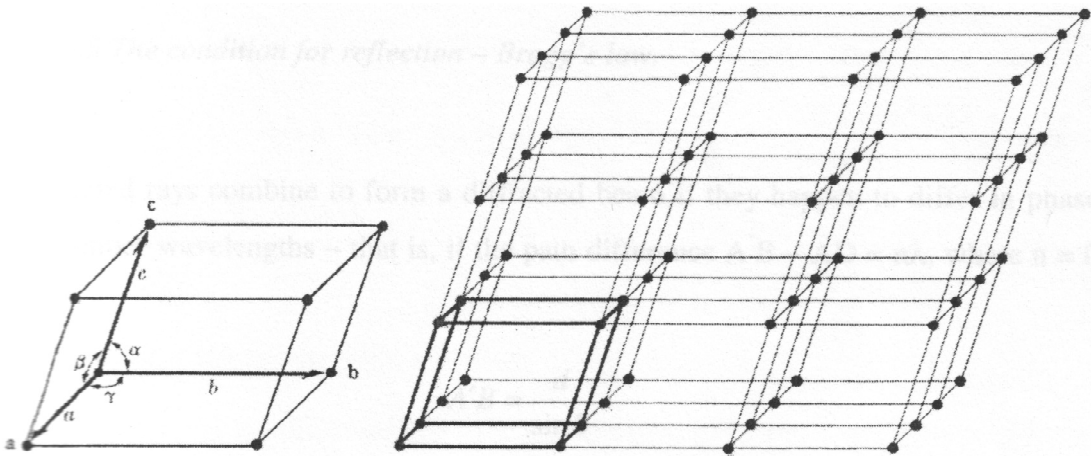


Figure B.5: (a) A unit cell showing the lattice parameters a , b and c . (b) The three-dimensional lattice [B.26].

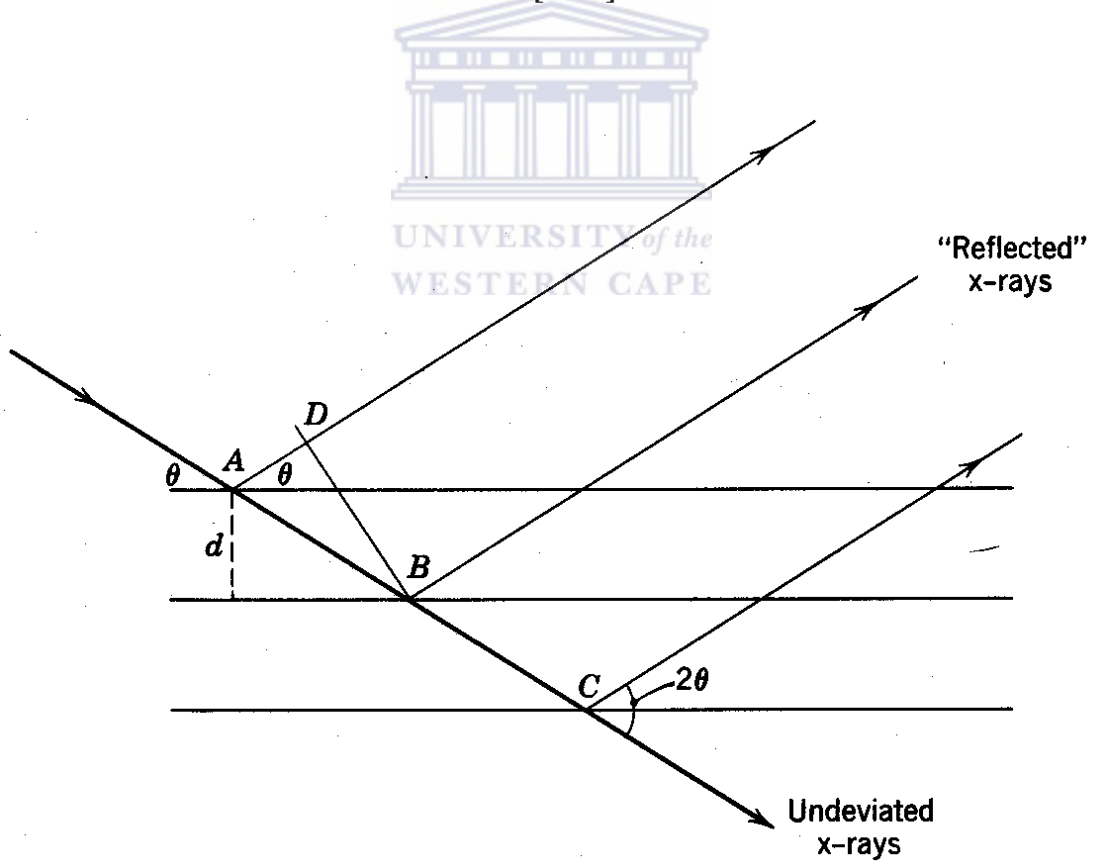


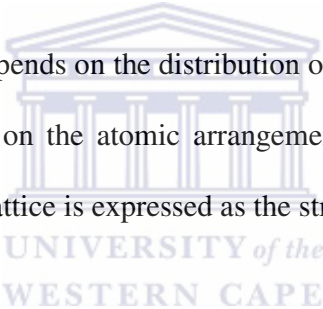
Figure B.6: The condition for Bragg's Law [B.23].

B.2.4 Atomic and structure factors

All waves scattered by the electrons in a single atom have the same path length for the incident beam direction and are therefore in phase. Thus the amplitude of the wave from the whole atom is proportional to the number of electrons in the atom for this direction [B.27]. The scattering power of an atom is therefore dependent on the direction of observation and its atomic number Z .

The efficiency of scattering by an atom in a particular observation is known as its atomic scattering factor f_0 and is defined as the ratio of the amplitude of the wave scattered by an atom, and the amplitude of the wave scattered by an electron [B.28].

The scattering from an atom depends on the distribution of its electrons, but the scattering from a crystal lattice depends on the atomic arrangements. The total amplitude of the wave diffracted by the crystal lattice is expressed as the structure factor F :


$$F_{hkl} = \sum_{j=1}^N f_j \exp^{2\pi i(hx_j + ky_j + lz_j)}$$

The D8 advance system is equipped to perform a number of different scans:

Locked couple: both the tube and detector move towards each other during the measurement.

Tube scan: the detector remains fixed, while the tube scans the theta range.

Detector scan: the tube remains fixed, while the detector scans the 2θ range [B.29].

B.3 Virtual Reality Modelling Language (VRML)

B.3.1 Introduction

In 1994, at the First International Conference on the World Wide Web (WWW), Tim Berners-Lee invited Mark Pesce to present a paper. Pesce and partner Tony Parisi at that time had developed Labyrinth, a prototype three-dimensional interface to the Web. A consensus was reached that there was a need for a common language to specify three-dimensional (3D) scene descriptions over the Internet [B.30]. The VRML specification started here with a set of requirements that was agreed on. The successful protocol had the following requirements: platform independence; extensibility; and the ability to work over low bandwidth (14.4 kilobits per second (kBps) modem) connections. VRML was designed to be platform-independent, and therefore accessible under any operating system provided the user has a web browser [B.31, B.32]. The web browser should have the Cosmo Player, Cortona or any other VRML plug-in installed on the computer. This extensibility feature makes it possible to add extra features to the VRML hierarchy, which is very similar to how Hypertext Markup Language (HTML) was designed [B.32].

An advantage of VRML is that it provides a highly efficient format for describing simple as well as complex objects and VRML worlds. In VRML, a world is a representation of a three-dimensional environment. It is necessary for VRML files to be efficient, since they are transferred over the Internet, and the medium that the VRML data are sent through can be as slow as normal telephone lines or as fast as satellite connections. An end user's computer could range from low-end computers right through to the most powerful computer hardware. VRML has excellent features when used for visualisation of two-dimensional data, for example taking a tour of a campus facility. Students can save time by better orientating themselves, e.g. they can find lecture halls, laboratories, libraries, etc. by getting an overview of the campus grounds through the VRML tour beforehand.

The proto-VRML community selected the Open Inventor ASCII File Format from Silicon Graphics, Inc. as the basis of VRML. This Inventor File Format supports complete descriptions of 3D scenes with geometry, lighting, materials, 3D user interface widgets, and viewers. It had all of the features that developers needed to create highly interactive 3D applications, as well as an existing tool base with a wide installed presence. A subset of the Inventor File Format, with extensions to support networking, was the underpinning of VRML 1.0 [B.33]. Rikk Carey and Gavin Bell adapted the Inventor File Format for VRML, with extensive input from the developers and Silicon Graphics, Inc. The Joint Technical Committee 1 (JTC1) of the International Standards Organization (ISO) and the International Electrotechnical Commission (IEC), in partnership with the VRML Consortium, developed the VRML97 International Standard. The formal process of getting VRML97 to become an international standard began in June 1996 with the Consortium's VRML 2.0 draft specification, with representatives from the VAG and JTC 1 (ISO/IEC JTC 1/SC 24, Computer Graphics and Image Processing) [B.34].

VRML is a rich text language for description of three-dimensional (3D) interactive virtual worlds as well as a modelling language. This makes VRML more complex than Hypertext Markup Language (HTML) but less complicated than a programming language like C and Pascal [B.33]. VRML enables the building of complex, realistic 3D environments, complete with shiny materials, textured surfaces and multiple light sources. VRML can sense viewers' touch and position, and trigger sounds and animations based on the viewer's proximity. It can fly the viewer on a guided tour of the world and even communicate with other applications and users on the Internet. A VRML world can be edited with any text editor. Files that are authored can be viewed using a VRML browser,

available as plug-ins to Netscape, add-ins to Internet Explorer, or as stand-alone browsers. The VRML files have the extension “.wrl” pronounced “dot world” [B.35].

Irrespective of the type of virtual world, all VRML worlds have certain common characteristics. A VRML world is immersive. The user enters the world on the computer screen and explores it as though it were part of the real world. Each person can move in a unique path through the VRML world. The user, not the computer, controls the experience. The VRML developer can recommend a path through the VRML world. The local browser allows the user to explore the VRML world in any way the user decides [B.31].

A VRML world is interactive. Objects in the world can respond to each other and to external events caused by the user. The user can change elements in it.

A VRML world combines 2D and 3D objects, animation and multimedia effects into a single medium [B.32].

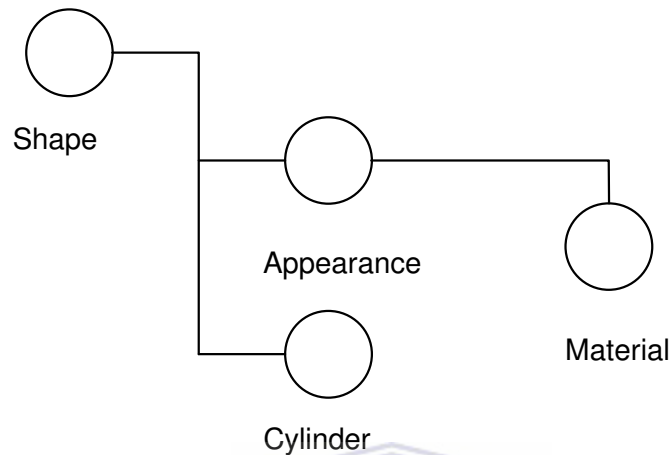
B.2.2 Working with VRML 2.0

VRML is a modelling language that is based on the use of nodes, all which perform different functions in a file. These nodes may be a transform node, a group node or a shape node. The following sub-section explains the syntax of VRML 2.0. The syntax is explained by examples of code.

The scene diagram’s purpose is to show the relationship between the nodes, assist in the design and troubleshoot if necessary. The usefulness of scene diagrams becomes evident

when developing VRML worlds, where there are many nodes [B.38]. A basic VRML file contains the type of shape that is required, and the colour of the object [B.39, B.40].

Scene Diagram for Example 1



The following example shows how to create a cylinder using VRML . The scene diagram shows that there is only one object in the VRML world, a cylinder. Any changes in the Material node will transform the colour of the object and so change the appearance of the object. It is important to recognise the relationship between the nodes and that any changes in the Appearance, Material and Cylinder nodes will affect the Shape node in the VRML world [B.40].

Code for Example 1

```
#VRML V2.0 utf8  
# Build a cylinder shape  
Shape {  
    Appearance appearance {  
        Material material {  
            diffuseColor 0.8 0.8 0.8
```

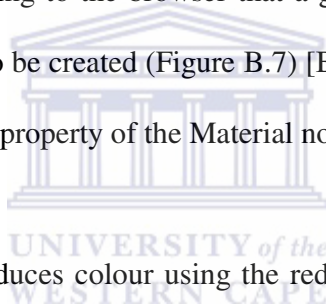
```

    }
}

geometry Cylinder {
    height 2.0
    radius 1.0
}
} # End of shape [B.39, B.41]

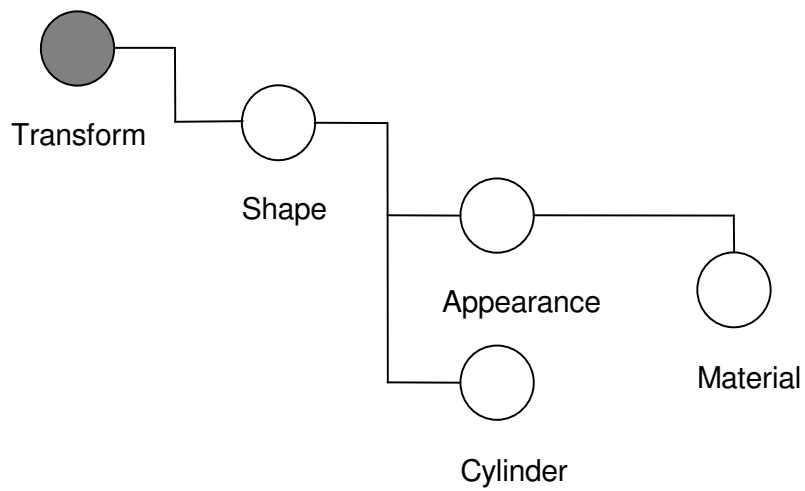
```

By understanding the scene diagram, it is easy to recognise the function of all the nodes present in the code. This VRML file (example 1 code) can be seen as a set of instructions to the VRML browser, indicating to the browser that a grey cylinder with a height of 2 units and a radius of 1 unit is to be created (Figure B.7) [B.42]. The colour of the cylinder is specified in the `diffuseColor` property of the `Material` node [B.41].



The `diffuseColor` property produces colour using the red, green and blue (RGB) format [B.41]. The RGB format is a red, green and blue colour model that uses a Cartesian coordinate system (Figure B.8). The RGB primaries are additive, i.e. the individual contributions of each primary are added together to form a result. The main diagonal of the cube, with equal amounts of each primary, represents the grey levels. Each value ranges from 0.0 to 1.0, dependent on the intensity of the colour that is required [B.43].

Scene Diagram for Example 2



This example with the above scene diagram [B.44] shows how to create a shiny purple cylinder using VRML but with the addition of the Transform node, which gives the developer the option to move, rotate or scale the object created in the VRML world. Empty circles in a scene diagram show non-grouping nodes [B.39]. Shaded circles show grouping nodes [B.40].

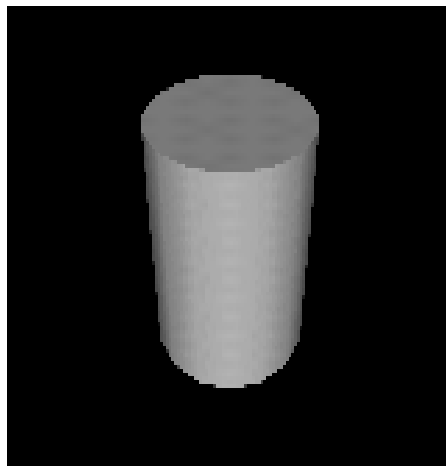


Figure B.7: A print screen showing the result of example 1

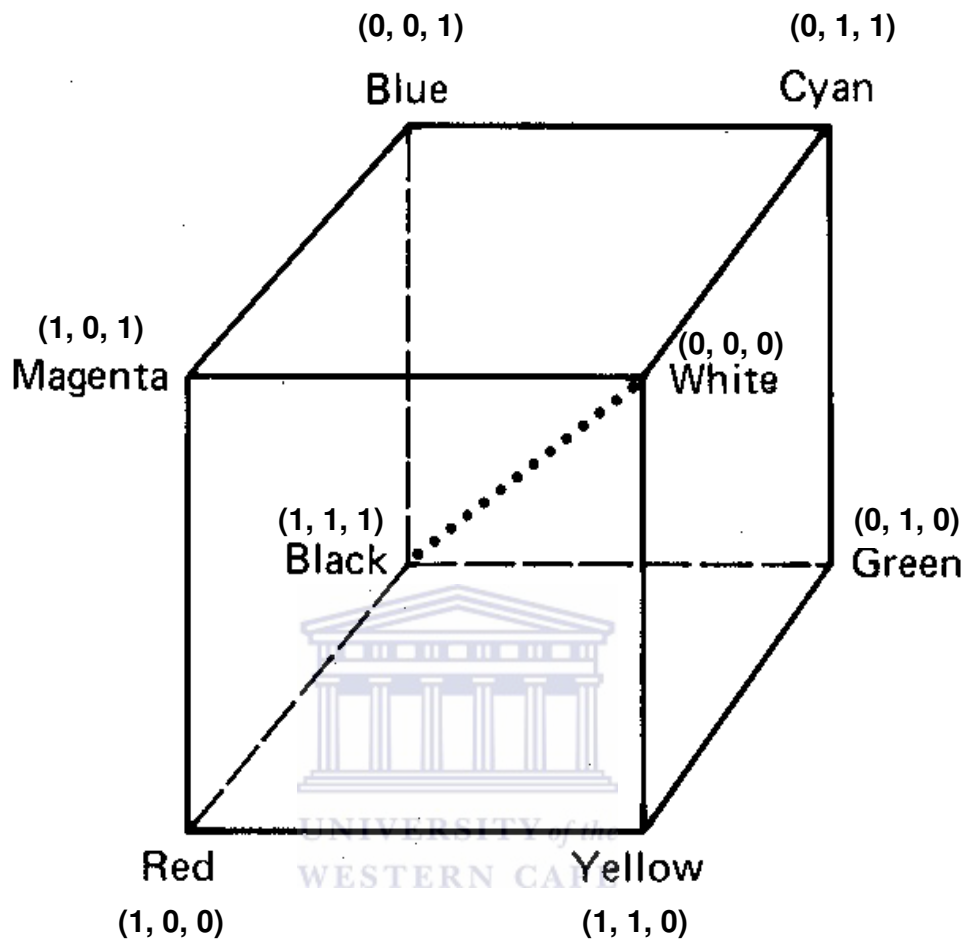


Figure B.8: The RGB colour cube where the greys are on the dotted diagonal
[B.43]

Code for Example 2

Transform {

translation 1 0 0

children [

Shape {

appearance Appearance {

material Material (

```

        diffuseColor 0.5 0 0.5
        shininess 0.5
    }
}

geometry Cylinder (
    radius 3
    height 6
    side TRUE
    top FALSE
    bottom TRUE
)
]
] # End of transform

```



The inclusion of “top FALSE” and “bottom TRUE” makes the purple cylinder have a top surface but not a bottom surface similar to a drinking glass [B.44].

B.2.3 Animation

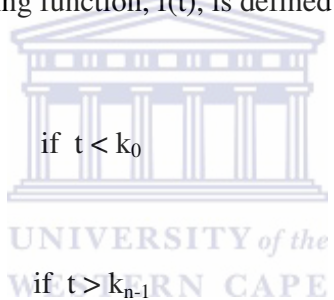
Animation creates motion of an object in VRML. This can be achieved by the use of nodes or the use of scripts. The types of nodes that are used for animation are called Interpolators, of which there are different types, namely: CoordinateInterpolators, ColorInterpolators, PositionInterpolators and OrientationInterpolators. When using scripts for animation a number of scripting languages can be used, for example JavaScript, ECMAScript and VRMLScript. The initiators of animation are known as triggers, which are generally sensors but can also take the form of other animation sequences [B.45].

B.2.4 Interpolators

Interpolator nodes are designed for linear keyframe animation where it defines a piecewise linear function, $f(t)$, on the interval $(-\infty, \infty)$. The piecewise function is defined by n values of t , called key, and the n corresponding values of $f(t)$, called keyValue. The keys must be monotonic non-decreasing and are not restricted to any interval. An interpolator node evaluates $f(t)$ given any value of t (via the `set_fraction eventIn`) [B.46].

Let the n keys $k_0, k_1, k_2, \dots, k_{n-1}$ partition the domain $(-\infty, \infty)$ into the $n+1$ sub-intervals given by $(-\infty, k_0)$, $[k_0, k_1)$, $[k_1, k_2)$, \dots , $[k_{n-1}, \infty)$. Also let the n values $v_0, v_1, v_2, \dots, v_{n-1}$ be the values of an unknown function, $F(t)$, at the associated key values. That is, $v_j = F(k_j)$. The piecewise linear interpolating function, $f(t)$, is defined to be:

$$\begin{aligned}
 f(t) &= v_0, && \text{if } t < k_0 \\
 &= v_{n-1}, && \text{if } t > k_{n-1} \\
 &= v_i, && \text{if } t = k_i \text{ for some value of } i, \text{ where } -1 < i < n \\
 &= \text{linterp}(t, v_j, v_{j+1}), && \text{if } k_j < t < k_{j+1}
 \end{aligned}$$



where $\text{linterp}(t,x,y)$ is the linear interpolant and $-1 < j < n-1$.

The third conditional value of $f(t)$ allows the definition of multiple values for a single key, in other words, limits from both the left and right at a discontinuity in $f(t)$ [B.47]. The first specified value will be used as the limit of $f(t)$ from the left and last specified value will be used as the limit of $f(t)$ from the right. The value of $f(t)$ at a multi-defined key is indeterminate, but should be one of the associated limit values [B.48].

When stipulating a list of keyframe values and times, the VRML browser automatically interpolates the “in-betweens”. As VRML implementations were designed to be small, fast and simple, only linear interpolation is supported, even though most commercial animation systems support spline curve interpolations. It should be noted that it is possible, however, for sophisticated spline curves to be generated and written to a VRML file using exclusively linear interpolators. There would, however, be many more keyframes specified to produce smooth or complex animations [B.47].

The keyValue depends on the type of interpolator used. For PositionInterpolator, ColorInterpolator, OrientationInterpolator and CoordinateInterpolator the keyValues will all be different because they all describe different characteristics [B.48].

1) *PositionInterpolator*

This interpolator is used for moving an object through a series of stipulated positions indicated in x, y as z coordinates over a period of time. The following code example is extracted from the electron gun in the virtual scanning electron microscope.

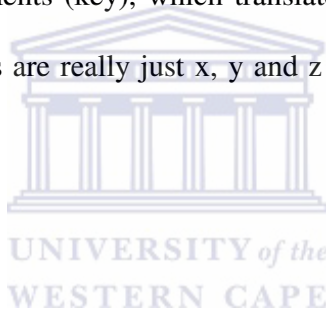
```
DEF UnnamedShapeTranslationInterp_15 PositionInterpolator {  
    Key [ 0, 0.1, 0.2, 0.3,  
        0.4, 0.5, 0.6, 0.7,  
        0.8, 0.9, 1 ]  
    keyValue [ 2.80947 15.5294 -135.51,  
        1.65041 14.878 -135.359,  
        0.443432 14.2377 -135.211,  
        -0.739588 13.5918 -135.062,
```

```

-1.82679 12.9238 -134.907,
-2.7463 12.217 -134.744,
-3.45022 11.4604 -134.569,
-3.98645 10.665 -134.385,
-4.42686 9.84745 -134.197,
-4.84332 9.02437 -134.007,
-5.30769 8.21237 -133.819 ]
}

```

The PositionInterpolator is named “UnnamedShapeTranslationInterp_15” and divides the animation period into 11 segments (key), which translates into 11 positions (keyValue) [B.49]. The keyValue numbers are really just x, y and z coordinates along the animated path.



2) *CoordinateInterpolator*

This interpolator describes the vertices of an object. The keyValue property of this interpolator includes the vertices of an object. One example of this interpolator is in the use of morphing objects. Morphing can be explained as the transition of an object (e.g. a sphere) to another object (e.g. a cylinder) in an animation sequence [B.50].

3) *ColorInterpolator*

This allows for cascading between colours of an object, for example a wood fire in a VRML world where the colour of the fire varies between red, orange and yellow [B.51].

4) *OrientationInterpolator*

This interpolator is used for rotation of an object. The keyValue property contains the angles in radians by which the object would rotate, for example a boomerang flying through a VRML world [B.52].

5) *Triggers*

There are various types of sensors which serves as triggers in animations, namely TouchSensors, ProximitySensors and TimeSensors [B.53].

a) TouchSensors

A TouchSensor is used to initiate an animation of an object and is activated when clicking on an object that has been designated for animation. The property that is activated is called **isActive** (a boolean) and is set to true by clicking on the object [B.54].

b) ProximitySensors

This type of sensor is activated when the viewer has reached a certain distance from the object. The **isActive** field is set to true once the viewer is within the region designated as the proximity sensor [B.55].

c) TimeSensors

It is important to note that VRML is an event-programming language, meaning that there is a transfer of events from one node to the next through the process of routing. Routing is essentially a process by which there is a linking of nodes in order to create animation. There are different types of events, eventins and eventouts. Eventins are events that accept events from other nodes. Eventouts send out events to other nodes. The timesensor is used for timing in animation (Figure B.9). It consists of properties that can only be used as eventins and eventouts or both of them. It should always be remembered when routing

events together that they are both of the same type [B.56, B.57]. Fraction_changed is a eventout that changes the value from 0 to 1 during a cycle. It is a single-field floating point variable, and is therefore defined as a SFFloat variable [B.57].

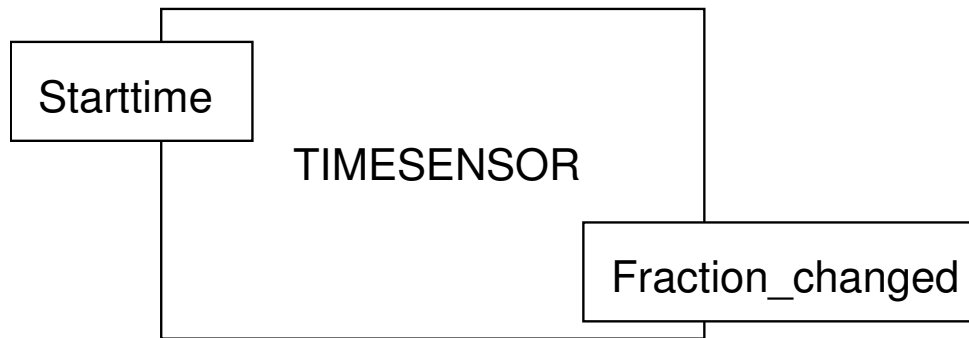


Figure B.9: An EventIn (Starttime) and Eventout (Fraction_changed) of the timesensor node [B.58]

B.4 References – Appendix B

- B.1 Chu, W.K., Mayer, J.W. & Nicolet, M.A. (1978). *Backscattering spectrometry*. New York: Academic Press.: 21.
- B.2 Chu, W.K., Mayer, J.W. & Nicolet, M.A. (1978). *Backscattering spectrometry*. New York: Academic Press.: 22.
- B.3 Chu, W.K., Mayer, J.W. & Nicolet, M.A. (1978). *Backscattering spectrometry*. New York: Academic Press.: 28.
- B.4 Chu, W.K., Mayer, J.W. & Nicolet, M.A. (1978). *Backscattering spectrometry*. New York: Academic Press.: 23.
- B.5 Feldman, L.C. & Mayer J.W. (1986). *Fundamentals of surface and thin film analysis*. Amsterdam: North-Holland Publishers.

- B.6 Chu, W.K., Mayer, J.W. & Nicolet, M.A. (1978). *Backscattering spectrometry*.
New York: Academic Press.: 29.
- B.7 Chu, W.K., Mayer, J.W. & Nicolet, M.A. (1978). *Backscattering spectrometry*.
New York: Academic Press.: 36.
- B.8 Chu, W.K., Mayer, J.W. & Nicolet, M.A. (1978). *Backscattering spectrometry*.
New York: Academic Press.: 61, 62.
- B.9 Chu, W.K., Mayer, J.W. & Nicolet, M.A. (1978). *Backscattering spectrometry*.
New York: Academic Press.: 59.
- B.10 Chu, W.K., Mayer, J.W. & Nicolet, M.A. (1978). *Backscattering spectrometry*.
New York: Academic Press.: 44.
- B.11 Chu, W.K., Mayer, J.W. & Nicolet, M.A. (1978). *Backscattering spectrometry*.
New York: Academic Press.: 77, 78, 79.
- B.12 Chu, W.K., Mayer, J.W. & Nicolet, M.A. (1978). *Backscattering spectrometry*.
New York: Academic Press.: 74.
- B.13 Chu, W.K., Mayer, J.W. & Nicolet, M.A. (1978). *Backscattering spectrometry*.
New York: Academic Press.: 83.
- B.14 Chu, W.K., Mayer, J.W. & Nicolet, M.A. (1978). *Backscattering spectrometry*.
New York: Academic Press.: 82.
- B.15 Cullity, B.D. (1978). *Elements of X-ray diffraction*. (2nd edition). Reading,
MA.: Addison Wesley Publishing Inc.: 3.
- B.16 Nuffield, E.W. (1966). *X-ray diffraction methods*. New York: John Wiley &
Sons, Inc.: 32, 34.
- B.17 Nuffield, E.W. (1966). *X-ray diffraction methods*. New York: John Wiley &
Sons, Inc.: 33.

- B.18 Nuffield, E.W. (1966). *X-ray diffraction methods*. New York: John Wiley & Sons, Inc.: 46.
- B.19 Nuffield, E.W. (1966). *X-ray diffraction methods*. New York: John Wiley & Sons, Inc.: 48.
- B.20 Nuffield, E.W. (1966). *X-ray diffraction methods*. New York: John Wiley & Sons, Inc.: 50.
- B.21 Nuffield, E.W. (1966). *X-ray diffraction methods*. New York: John Wiley & Sons, Inc.: 53.
- B.22 Nuffield, E.W. (1966). *X-ray diffraction methods*. New York: John Wiley & Sons, Inc.: 54.
- B.23 Nuffield, E.W. (1966). *X-ray diffraction methods*. New York: John Wiley & Sons, Inc.: 58.
- B.24 Nuffield, E.W. (1966). *X-ray diffraction methods*. New York: John Wiley & Sons, Inc.: 62.
- B.25 Nuffield, E.W. (1966). *X-ray diffraction methods*. New York: John Wiley & Sons, Inc.: 63.
- B.26 Cullity, B.D. (1978). *Elements of X-ray diffraction. (2nd edition)*. Reading, MA.: Addison Wesley Publishing Inc.: 33.
- B.27 Nuffield, E.W. (1966). *X-ray diffraction methods*. New York: John Wiley & Sons, Inc.: 64.
- B.28 Cullity, B.D. (1978). *Elements of X-ray diffraction. (2nd edition)*. Reading, MA.: Addison Wesley Publishing Inc.: 112.
- B.29 Woolfson, M.M. (1978). *An introduction to X-ray crystallography*. Cambridge: Cambridge University Press: 81.

- B.30 Carey, R. & Bell, G. (1997). *The annotated VRML 2.0 reference manual*. New Jersey: Addison Wesley Developers Press: 5.
- B.31 Carey, R. & Bell, G. (1997). *The annotated VRML 2.0 reference manual*. New Jersey: Addison Wesley Developers Press: 3.
- B.32 Carey, R. & Bell, G. (1997). *The annotated VRML 2.0 reference manual*. New Jersey: Addison Wesley Developers Press: 4.
- B.33 Carey, R. & Bell, G. (1997). *The annotated VRML 2.0 reference manual*. New Jersey: Addison Wesley Developers Press: 2.
- B.34 Carey, R. & Bell, G. (1997). *The annotated VRML 2.0 reference manual*. New Jersey: Addison Wesley Developers Press: 6.
- B.35 Carey, R. & Bell, G. (1997). *The annotated VRML 2.0 reference manual*. New Jersey: Addison Wesley Developers Press: 18.
- B.36 Hartman, J. & Wernecke, J. (1996). *The VRML 2.0 handbook: building moving worlds on the Web*. New Jersey: Addison Wesley Developers Press: 3.
- B.37 Hartman, J. & Wernecke, J. (1996). *The VRML 2.0 handbook: building moving worlds on the Web*. New Jersey: Addison Wesley Developers Press: 4.
- B.38 Hartman, J. & Wernecke, J. (1996). *The VRML 2.0 handbook: building moving worlds on the Web*. New Jersey: Addison Wesley Developers Press: 34.
- B.39 Hartman, J. & Wernecke, J. (1996). *The VRML 2.0 handbook: building moving worlds on the Web*. New Jersey: Addison Wesley Developers Press: 39.
- B.40 Hartman, J. & Wernecke, J. (1996). *The VRML 2.0 handbook: building moving worlds on the Web*. New Jersey: Addison Wesley Developers Press: 40.
- B.41 Hartman, J. & Wernecke, J. (1996). *The VRML 2.0 handbook: building moving worlds on the Web*. New Jersey: Addison Wesley Developers Press: 38.

- B.42 Hartman, J. & Wernecke, J. (1996). *The VRML 2.0 handbook: building moving worlds on the Web*. New Jersey: Addison Wesley Developers Press: 36.
- B.43 Foley, J.D. & Van Dam, A. (1982). *Fundamentals of interactive computer graphics*. Reading, MA.: Addison Wesley Publishing Co.: 611.
- B.44 Hartman, J. & Wernecke, J. (1996). *The VRML 2.0 handbook: building moving worlds on the Web*. New Jersey: Addison Wesley Developers Press: 41.
- B.45 Hartman, J. & Wernecke, J. (1996). *The VRML 2.0 handbook: building moving worlds on the Web*. New Jersey: Addison Wesley Developers Press: 115.
- B.46 Carey, R. & Bell, G. (1997). *The annotated VRML 2.0 reference manual*. New Jersey: Addison Wesley Developers Press: 84.
- B.47 Carey, R. & Bell, G. (1997). *The annotated VRML 2.0 reference manual*. New Jersey: Addison Wesley Developers Press: 85.
- B.48 Carey, R. & Bell, G. (1997). *The annotated VRML 2.0 reference manual*. New Jersey: Addison Wesley Developers Press: 86.
- B.49 Hartman, J. & Wernecke, J. (1996). *The VRML 2.0 handbook: building moving worlds on the Web*. New Jersey: Addison Wesley Developers Press: 331.
- B.50 Hartman, J. & Wernecke, J. (1996). *The VRML 2.0 handbook: building moving worlds on the Web*. New Jersey: Addison Wesley Developers Press: 286.
- B.51 Hartman, J. & Wernecke, J. (1996). *The VRML 2.0 handbook: building moving worlds on the Web*. New Jersey: Addison Wesley Developers Press: 281.
- B.52 Hartman, J. & Wernecke, J. (1996). *The VRML 2.0 handbook: building moving worlds on the Web*. New Jersey: Addison Wesley Developers Press: 323.
- B.53 Hartman, J. & Wernecke, J. (1996). *The VRML 2.0 handbook: building moving worlds on the Web*. New Jersey: Addison Wesley Developers Press: 120.

- B.54 Hartman, J. & Wernecke, J. (1996). *The VRML 2.0 handbook: building moving worlds on the Web*. New Jersey: Addison Wesley Developers Press: 359.
- B.55 Hartman, J. & Wernecke, J. (1996). *The VRML 2.0 handbook: building moving worlds on the Web*. New Jersey: Addison Wesley Developers Press: 333.
- B.56 Hartman, J. & Wernecke, J. (1996). *The VRML 2.0 handbook: building moving worlds on the Web*. New Jersey: Addison Wesley Developers Press: 356.
- B.57 Hartman, J. & Wernecke, J. (1996). *The VRML 2.0 handbook: building moving worlds on the Web*. New Jersey: Addison Wesley Developers Press: 357.
- B.58 Hartman, J. & Wernecke, J. (1996). *The VRML 2.0 handbook: building moving worlds on the Web*. New Jersey: Addison Wesley Developers Press: 133.



APPENDIX C: INTERNET USES

C.1 Summary

This appendix will summarise the Internet developments with respect to virtual laboratories, remote instrumentation and collaboratories, all this information is conveniently placed in a table. The articles below describe a wide range of developments from infrastructure development to facilitate remote instrumentation to the improvements being currently done in collaboratory tools.

Table C.1: A list of developments and its use briefly described.

The uses of the Internet in research
The development of CORBA (a mechanism that facilitates communication between different programming languages) to control remote operated instruments, and is mainly used in Physics experiments [C.1].
The development of a software architecture to facilitate remote participation at the Textor 94 experiment in Germany [C.2].
The usage of remote instrumentation for martian missions to measure pressure, humidity and temperature [C.3].
The usage of the Internet to deliver healthcare and exchange information across distances in especially rural areas in Nigeria [C.4].
A remote data acquisition and control system for Mossbauer spectroscopy [C.5].
The remote teaching of instruments and the providing of remote access to instruments [C.6].
The real time access to images from echocardiography to evaluate and diagnose

patients [C.7].
The remote processing of real time images at a remote site to facilitate medical purposes [C.8].
The remote access of spatial information from databases to develop virtual environments to navigate geographical features [C.9].
The development of a configurable remote access measurement system, that can easily facilitate making instruments remotely accessible [C.10].
The remote measurement of a volcano in Mexico (Volcan de Colima) to predict the time of eruptions [C.11].
The remote raman and fluorescence studies of mineral samples by the Mars Rover [C.12].
The use of remote instruments to detect algae on the land rover on Mars using reflectance spectroscopy [C.13].
The remote detection of water formations on Mars using satellites [C.14].
The usage of remote instruments on the International Space Station to perform remote sensing experiments [C.15].
The use of the Internet in detecting when remote instruments need maintenance [C.16].
An artificial neural network is trained to control and monitor its learning via the Internet [C.17].
Minimal invasive therapy demonstrated remotely using the Internet [C.18].
Power plants, both nuclear and fossil are diagnosed over the Internet [C.19].
The use of the Internet in physiotherapy to evaluate the knee's range of motion [C.20].
The use of the Internet to control a robotic system, and accommodate for Internet lag

[C.21].
Remote control of an MRI instrument through the Internet and teach students about embryology [C.22].
Remote ultrasonic scanning over the Internet to check internal material defects [C.23].
A interdisciplinary virtual laboratory on nanoscience called the Swiss Virtual Campus [C.24].
A web based virtual laboratory that assists in unit operations and process systems engineering [C.25].
A virtual laboratory in materials science that uses RBS and PIXE facilities [C.26].
A virtual laboratory for molecular science using the GRID, to facilitate scientific research [C.27].
The use of the Internet to facilitate real time water quality monitoring [C.28].
The improvement of communication and collaboration through the Internet at the Tokamak DIII-D control room at the National Fusion Collaboratory [C.29].
The use of collaboration tools to assist in the discovery of new drugs [C.30].
The use of collaboration tools to check the quality of programs written in C and Cobol [C.31].
The solving of numerical relativity and astrophysics applications using GRID and collaborative tools [C.32].
Robotically automated telescopes that are located near Sutherland, South Africa. Input parameters are entered via the Internet and output viewed over the Internet [C.33, C34].

C.2 References – Appendix C

- C.1 Fernandes H., Pereira J.P.A. & Varandas C.A.F. (2002). A CORBA sharing and messaging server–client information system. *Fusion Engineering and Design*. 60: 279.
- C.2 Nidero B.U., Gerritsen A.A., van Haren P.C., Lourens W., Taal A., Fuchs C., Kemmerling G., Korten M., Kooijman W., Wijnoltz F. & Oomens A.A.M. (2001). A software architecture for remote participation at the Textor-94 experiment. *Fusion Engineering and Design*. 56: 1045.
- C.3 Harri A-M., Siili T., Pirjola R. & Pellinen R. (1995). Aspects of Atmospheric Science and instrumentation for Martian missions. *Adv. Space Res.* 16: 615.
- C.4 Adewale O.S. (2004). An Internet-based telemedicine system in Nigeria. *International Journal of Information Management*. 24: 221.
- C.5 Zhou Q., Wang L., Wang Y., Zhao H. & Zhou R. (2004). A remote data acquisition and control system for Mossbauer spectroscopy. *Nuclear Instruments and Methods in Physics Research B*. 215: 577.
- C.6 Arpaia P., Baccigalupi A., Cennamo F. & Daponte P. (1997). A remote measurement laboratory for educational experiments. *Measurement*. 21: 157.
- C.7 Naravan G.A., Liang D. & Hu B. (2002) Real-Time Expert-Guided Remote Echocardiography is an Accurate Clinical Tool. *Computer Applications: Cardiac Imaging and Physiological Modeling*. 459A: 1216-165.
- C.8 Inoa F., Ooyamab K., Kawasakia Y., Takeuchib A., Mizutania Y., Masumotob J., Satoc Y., Suganoc N., Nishiic T., Mikic H., Yoshikawac H., Yonenobud K., Tamurac S., Ochic T. & Hagiharaa K. (2003). A high-performance computing

- service over the Internet for nonrigid image registration. *International Congress Series*. 1256: 193.
- C.9 Dykes J. (2000). An approach to virtual environments for visualization using linked geo-referenced panoramic imagery. *Computers, Environment and Urban Systems*. 24: 127.
- C.10 Abdelrahman M. & Rasheed A. (2000). A methodology for development of configurable remote access measurement system. *ISA Transactions* 39: 441.
- C.11 Murray J.B. & Ruiz J.J.R. (2002). Long-term predictions of the time of eruptions using remote distance measurement at Volcan de Colima, Mexico. *Journal of Volcanology and Geothermal Research*. 117: 79.
- C.12 Bozlee B.J., Misra A.K. (2005). Remote Raman and fluorescence studies of mineral samples. *Spectrochimica Acta Part A* 61: 2342.
- C.13 Davis W.L., McKay C.P. & Hynes S.F. (1999). Remote Sensing for organics on Mars. *Adv. Space Res.* 24: 489.
- C.14 Silvermana S., Christensen P. (2006). Successful Mars remote sensors, MOTHEMIS and MER Mini-TES. *Acta Astronautica*. 59: 1039.
- C.15 Broadfoot A.L. (2001). Remote Sensing from the International Space Station. *Adv. Space Res.* 27: 1047.
- C.16 Laugier A., Allahwerdib S N., Baudin J., Gaffney P., Grimsmd W., Groth T. & Schilders L. (1996). Remote instrument telemaintenance. *Computer Methods and Programs in Biomedicine*. 50: 187.
- C.17 Coates T.D. Jr. (2000). Control and monitoring of a parallel processed neural network via the World Wide Web. *Neurocomputing*. 32: 1021.

- C.18 Bennett R. & Kirstein P.T. (1997). Demonstrating minimal invasive therapy over the Internet. *International Journal of Medical Informatics*. 47: 101.
- C.19 Kunze U. (2003). Condition telemonitoring and diagnosis of power plants using web technology. *Progress in Nuclear Energy*. 43:129.
- C.20 Russell T.G., Jull G.A. & Wootton R. (2003). Can the Internet be used as a medium to evaluate knee angle? *Manual Therapy: Technical & measurement report*. 8(4): 242.
- C.21 You S., Wang T., Eagleson R., Meng C. & Zhang Q. (2001). A low cost Internet-based telerobotic system for access to remote laboratories. *Artificial Intelligence in Engineering*. 15: 265.
- C.22 Bruce B.C., Carragher B.O., Damon B.M., Dawson M.J., Eurell J.A., Gregory C.D., Lauterbur P.C., Marjanovic M.M., Mason-Fossum B., Morris H.D., Potter C.S. & Thakkar U. (1997). Chickscope: an interactive MRI classroom curriculum innovation for k-12. *Computers Educ.* 29: 73.
- C.23 Abd El-Ghany K.M. & Farag M.M. (2002). AUTONDT: new software for remote ultrasonic scanning over the Internet. *NDT&E International*. 35: 1.
- C.24 Guggisberg M., Fornaro P., Gyalog T. & Burkhart H. (2003). An interdisciplinary virtual laboratory on nanoscience. *Future Generation Computer Systems*. 19: 133.
- C.25 Shin D., Yoon E.S., Park S.J. & Lee E.S. (2000). Web-based interactive virtual laboratory system for unit operations and process systems engineering education. *Computers and Chemical Engineering*. 24: 1381.

- C.26 Orlic I., Zhou S., Sanchez J.L., Watt F. & Tang S.M. (1999). Virtual PIXE and RBS laboratory. *Nuclear Instruments and Methods in Physics Research B* 150: 83.
- C.27 Gervasi O., Riganelli A., Pacifici L., Laganà A. (2004). VMSLab-G: a virtual laboratory prototype for molecular science on the Grid. *Future Generation Computer Systems*. 20: 717.
- C.28 Toran F., Ramirez D., Navarro A.E., Casans S., Pelegri J. & Espi J.M. (2001). Design of a virtual instrument for water quality monitoring across the Internet. *Sensors and Actuators B*. 76: 281.
- C.29 McHarg Jr B.B., Casper T.A., Davis S. & Greenwood D. (1999). Tools for remote collaboration on the DIII-D National Fusion Facility. *Fusion engineering and design*, 43: 343-355.
- C.30 Rauwerda H., Roos M., Hertzberger B.O. & Breit T.M. (2006). The promise of a virtual lab in drug discovery. *Informatics Reviews: DDT*. 11:5
- C.31 Maresca P. (2000). Reverse engineering collaboratory: a logic-based tool for monitoring the quality of programs. *Engineering Applications of Artificial Intelligence*. 13: 99.
- C.32 Bondarescu R., Allen G., Daues G., Kelley I., Russell M., Seidel E., Shalf J., Tobias M. (2004) The Astrophysics Simulation Collaboratory Portal: a framework for effective distributed research. *Future Generation Computer Systems*. Article in Press.
- C.33 *The Wide Angle Search for Planets (SuperWASP) website*. [Online] Available <http://www.superwasp.org/waspsouth.htm>

C.34 *The Yonsei Survey Telescopes for Astronomical Research (YSTAR) website.*

[Online] Available <http://ystar.yonsei.ac.kr>



APPENDIX D: GRAPHS

D.1 Notes

This appendix shows the graphs of Figure 2.6 (Figure D.1) and Figure 2.7 (Figure D.2) with all its data points.

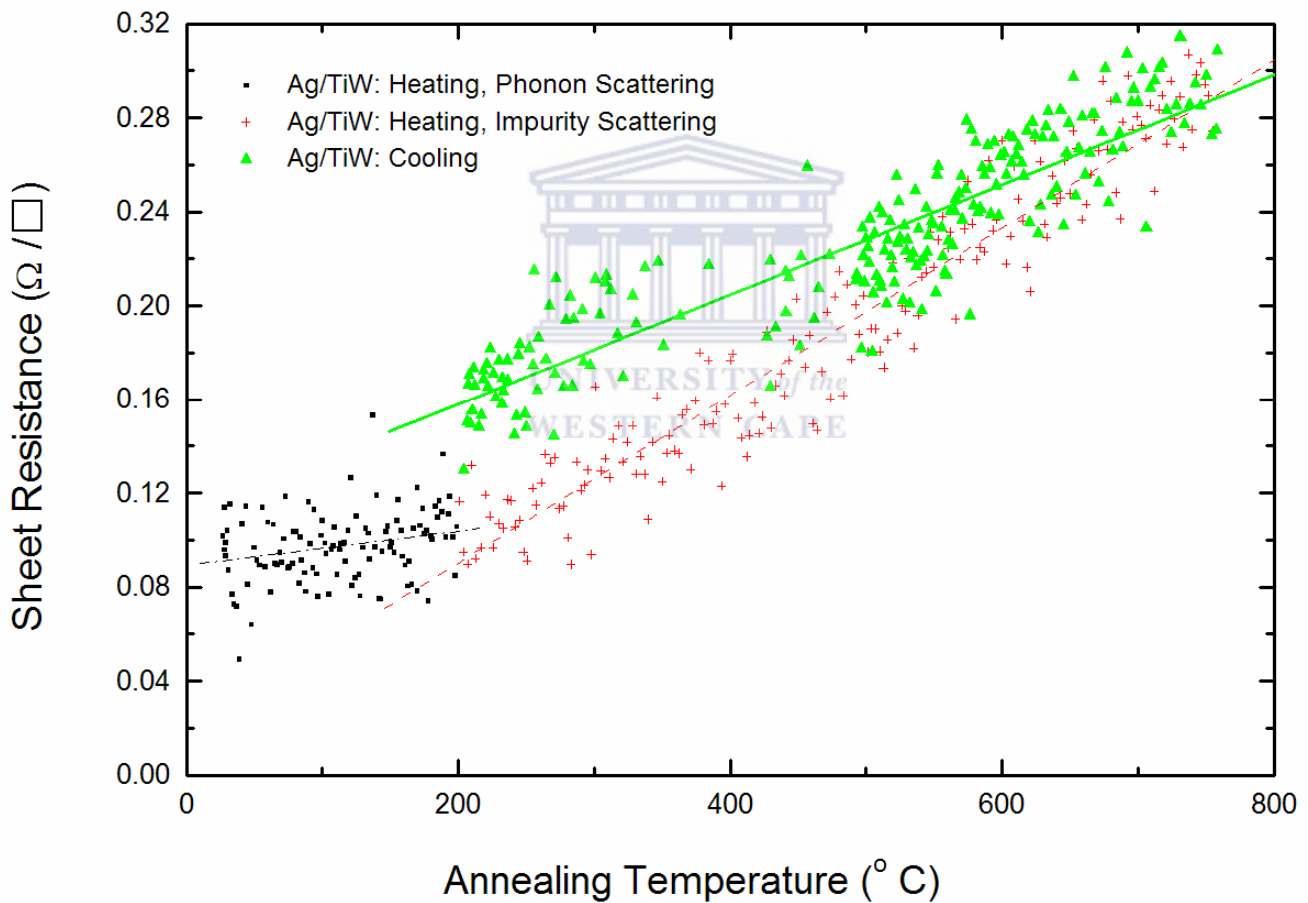


Figure D.1: Plot of sheet resistance vs. annealing temperature of an Ag (200 nm)/TiW (200 nm) sample

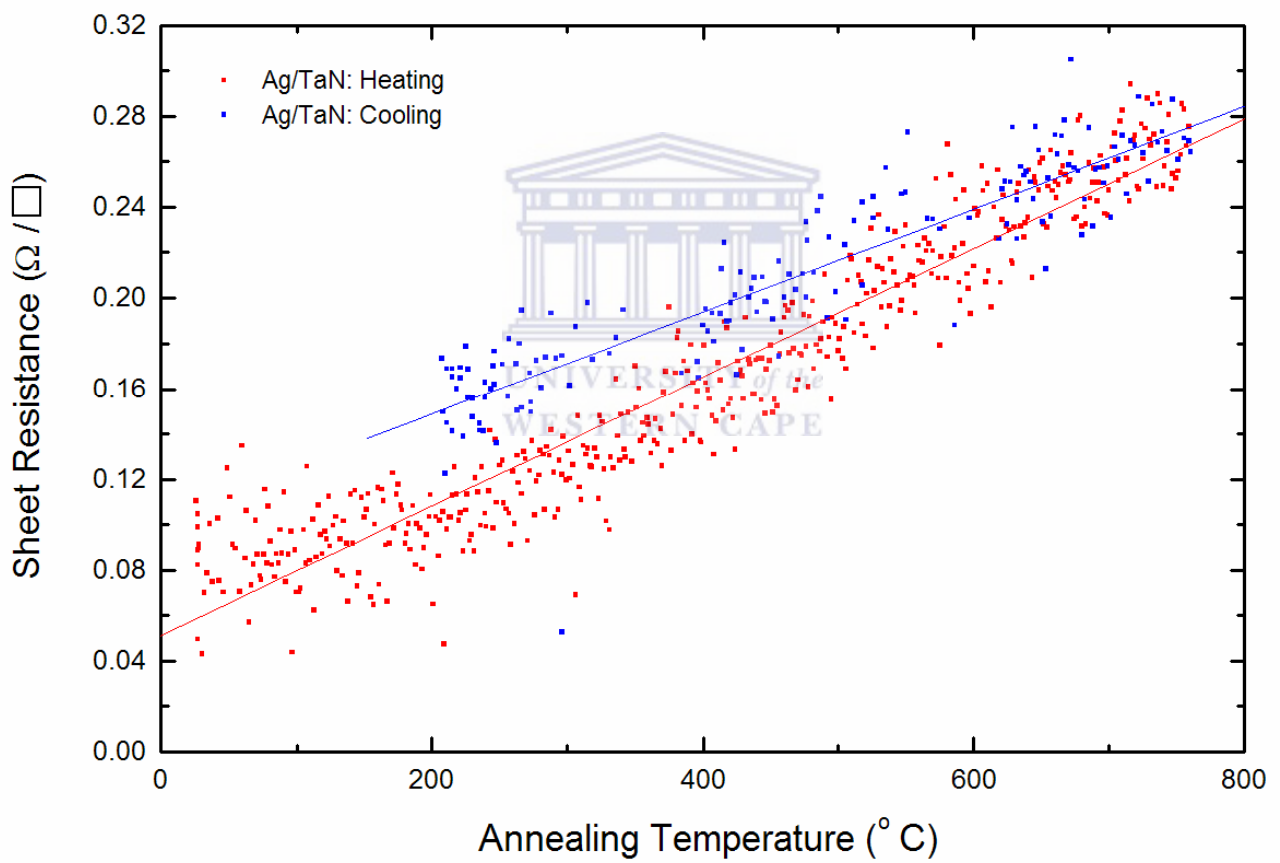


Figure D.2: Plot of sheet resistance vs. annealing temperature of an Ag (200 nm)/TaN (200 nm) sample